UC San Diego

UC San Diego Electronic Theses and Dissertations

Title

Millimeter-Wave Single- and Dual-Polarized 2x2 MIMO Phased Arrays and In-Situ Over-the-Air System-Level Self-Calibration Techniques for 5G Applications

Permalink

https://escholarship.org/uc/item/5k52357c

Author

Nafe, Ahmed

Publication Date

2020

Peer reviewed|Thesis/dissertation

eScholarship.org Powered by the California Digital Library
University of California

UNIVERSITY OF CALIFORNIA SAN DIEGO

Millimeter-Wave Single- and Dual-Polarized 2×2 MIMO Phased Arrays and In-Situ Over-the-Air System-Level Self-Calibration Techniques for 5G Applications

A dissertation submitted in partial satisfaction of the
requirements for the degree
Doctor of Philosophy

in

Electrical Engineering (Electronic Circuits and Systems)

by

Ahmed Nafe

Committee in charge:

Professor Gabriel Rebeiz, Chair
Professor Kam Arnold
Professor Gert Cauwenberghs
Professor William Hodgkiss
Professor Vitaliy Lomakin
Professor Daniel Sievenpiper

2020

Copyright
Ahmed Nafe, 2020
All rights reserved.

The dissertation of Ahmed Nafe is approved, and it is acceptable in quality and form for publication on microfilm and electronically:

_____

_____

_____

_____

_____

Chair

University of California San Diego

2020

DEDICATION

To my family

EPIGRAPH

I am among those who think that science has great beauty.

Marie Curie

TABLE OF CONTENTS

LIST OF FIGURES

LIST OF TABLES

ACKNOWLEDGEMENTS

Arriving to the conclusion of my Ph.D. journey, I can only feel gratitude to people that have helped me through it. For without them, I would not have been able to reach this moment and write this dissertation. In the next pages, I will try my best to express my deepest appreciation, in the hopes of doing them some justice.

First, I would like to take this opportunity to thank my committee members, Professor Kam Arnold, Professor Gert Cauwenberghs, Professor William Hodgkiss, Professor Vitaliy Lomakin and Professor Daniel Sievenpiper for the time and effort they spend into administering my qualification and final defense examinations as well as for their constructive comments on my work.

I would like to express my sincere gratitude to my advisor Professor Gabriel Rebeiz. It has been a privilege spending the past four years working under his supervision. Looking back, I realize that my relationship with Professor Rebeiz effectively started well before I arrived to UCSD and met him. I first came to know about Professor Rebeiz in late 2013, about 1.5 years before I arrived at UCSD for my Ph.D. studies. This happened when I came across his ECE166 Microwave Circuits and Systems course website. I instantly fell in love with the course, every aspect of it: the handwriting, the funny side notes, the well-designed problem sets. To me it was a masterpiece reflective of a master of the craft. I printed all the notes and made into a compact binder that I kept. I then looked for other courses he taught and found ECE 222A which I loved even more. I also printed the entire course and made into a compact booklet. It felt like I found a treasure. It was then that I decided that I want to come to UCSD for my Ph.D. I still remember my first day of ECE 222A, in Fall 2015, I had taken the notes that I printed 2 years ago, sat at the back of the class-room and professor Rebeiz entered and a symphony started. It just felt right, the professor's excitement in teaching was contagious and it peaked when the course reached antenna arrays. It was very clear that arrays had a special place in the professors' heart, a thing I too had since my first introduction of the topic in my undergraduate courses at the German University

in Cairo. This was love at first sight, which led to me work on arrays in both my bachelor and masters projects. It was clear to me that I should strive to join his group, and I was fortunate to join in the Spring of 2016 and my PhD journey officially started.

I could not have foreseen the amount I learned in his lab over the past 4 years. Not only technically but also in life-lessons and managerial skills. Professor Rebeiz's laser focus, humor, and extreme efficiency and dedication helped me stay motivated, on-track and very well-funded. Professor Rebeiz dedicates a lot of time to his students, our weekly meetings on the "table" are where the magic happens. He goes over every students' ($\sim$ 20) weekly reports slide-by-slide and line-by-line with pen and paper. Everything has to make sense. We discuss, argue, counter argue, think deeply, and repeat every week. It is the way he "makes" his students by constantly pushing them, as it is his goal to make them reach their full potential. It is still a mystery to all his students how he keeps his intense work style every day, and how he stays "hungry" and excited despite all of his achievements. The valuable experience and skill set I developed in my years at his lab made it rather easy to land multiple top job offers in my field despite the difficult economic times in Spring of 2020. I would like to take this opportunity to thank him for all his investment in me and patience for my-at times- excessive paranoia and costly obsession with grounding vias.

I feel lucky to be a member and alumni of the Rebeiz Academy of extraordinary gentlemen and ladies (a.k.a Tixers). I would like to thank all the people I have met in his group in the past five years: Kerim Kibaroglu, Hyunchul Chung, Abdurrahman Aljuhani, Omar El-Aassar, Qian Ma, Tom Phelps, Changtian Wang, Sultan Alqarni, Kevin Low, Gokhan Gultepe, Oguz Kazan, Siwei Li, Zhe Zhang, Dimitrios Baltimas, Shufan Wang, Bhaskara Rupakula, Eric Wagner, Yaochen Wang, Umut Kodak, Li Gao, Yusheng Yin, Abdulrahman Alhamed, Timothy Lee, Hasan Al-Rubaye, Samet Zihir, Tumay Kanar, Berktug Ustungtag, Mustafa Sayginer, Tsu-Wei Lin, Evan Traffenstedt, Arman Galioglu, Shugan Wang and Mustafa Lokhadwala.

A special thank you goes to the following Tixers:

Kerim and Mustafa for being my primary co-authors, making all the magnificent chips

used in my thesis work. They always had time for my questions even after they graduated from the group, joined industry, and moved to Los Angles and New Jersey. Thank you Kerim for all the long calls, discussions on everything from game-theory to Turkish deserts, for teaching me about the cup of coffee terminology and your unique aura. Mustafa, thank you for being an older brother, natural mentor, always kind, always helpful and selfless. Thank you again for arranging my talk at Bell-labs in Feb. 2020 and for your kind hospitality.

Omar, for being my first-year Ph.D. roommate, lab-mate, wise-counselor and future company colleague. To me, Omar is the definition of wise and good judgment. He never failed to give me frank advice and perspective whenever I needed it. It feels just like yesterday when we met in Cairo in August 2015 trying to find housing in La Jolla. I do miss our days at Costa-Verde apartments and the evenings of our "inventive" cooking. I want to thank you one more time for teaching me your cappuccino preparation technique for maximum foam. I got hooked and it has been an essential contributor to my Ph.D. work. Also, please deliver my thanks for Tante Magda for her motherly affection and for her the countless delicious molokhia's.

Abdurrahman Aljuhani, for being a brother from another mother. Through the past 4 years, I spent more time in Abdurrahman's company than anyone else's. We shared many experiences, probably had more breakfast, lunch, and dinner together than with anybody else in the past 4 years. We celebrated many achievements, consoled each other when things where difficult, shared many long nights and all nighters at the lab. I think by now I owe him like 100 gallons of gasoline for the many late-night rides home he gave me. I am sad to know that your time in the US is coming to an end but my consolation is that in few years, I will say I have friend who is leading phased array research is Saudi-Arabia.

The third floor EM group: Bhaskar, Kevin, Ghokan, Tom, Yusheng , Jacob, and Zhe for the many illuminating technical discussions, shared deadline nights, tea-time and Sambuusa Tuesdays. Kevin Lo, for showing me the definition of "neat-work" and many deep discussions. Tom for being the soul of sports activity in Tixers Lab and never giving up on soccer Saturdays.

Jacob for bringing the physicist aura to the third-floor office. Gokhan, for being the kind genius he is.

Life can be difficult and lonely away from home for international students. A thank you goes to all the Egyptian and Arabic friends at UCSD for making me feel less home sick: Loai Salem, Ahmed Al thakeb, Amr Eissa, Eslam Helal, Mohammed Badr, Ahmed Hussein, Sara Kandil, Sally Safwat, Nader Sheriff, Abdullah Abdulslam and Dr. Mohammed Salah El Hadri.

I would like to thank Loai again (Now Prof. Loai), for being the first responder when my appendix decided it no-longer wanted to stay with me in September 2017. Despite having an ISSCC deadline with a conference paper to write and precious little time left, Loai took care of me throughout that difficult day being triaged at the emergency, getting CT and comforting my parents over phone until I got out of surgery the next day. Loai, I cannot thank you enough.

I would like to extend my thanks and gratitude for the Al Ayoub family (Amo Hesham, Tante Amany, Zeyad, Noha, and Hana). They were the ones waiting for me when I arrived in LAX in September 2018 and hosted me at their home in the nice Rancho Palos Verdes, showed me around LA set-me up in the USA during my first week. Indeed I was infinitely more comfortable knowing that I am only two hours away from family. I hope you do forgive for being busy all the time and not being able to visit as much as I should. I am particularly regretful about turning down your Thanksgiving invitations year-after-year. It was always just before the IMS deadlines and I was always tight on time. Hopefully in the coming years, I am able to join.

To arrive at this day, I have had the privilege of great teachers and mentors throughout my life:

In KAUST, I would like to thank Professor Hakan Bagci and Professor Ahmed Sultan Salem for teaching me EM /signal processing techniques and encouraging me to persue a Ph.D. in the USA. Also Professor Andrea Fratalocchi and Professor Ying Wu for teaching me Optics and differential equations, respectively. Professor Atif Shamim for supervising my master thesis, sponsoring my masters studies and for letting me go, despite his best interests, when the

opportunity came in the USA.

In Germany, I would like to thank Professor Wolfgang Menzel for offering me the opportunity to do my bachelor project in 2011 at the Institute of Microwave Techniques at Ulm University, and Dr. Ing Micheal Frei for supervising my work, teaching me CST and antenna measurements. I would like to also thank Professor Renato Negra and Dr. Ahmed Farouk Aref for letting me work with them in the summer of 2011 at RWTH-Aachen and teaching me all about PA linearization and out-phasing transmitters.

In Egypt, I would like to thank all my professors at the German University in Cairo. Particular thanks go to Professor Frank Kuhnemann for sparking my interest in electromagnetism and optics, Professor Hany Hammad for teaching me RF concepts, waveguides and antennas. It was his wave-distribution class in Fall 2010, that set me on my current career trajectory. Eng. (Now Dr.'s) Shoukry Shams, Mohamed Kheir and Yasmine Abdalla for being excellent TAs and parental figures and for encouraging me to pursue microwave-engineering in post graduate studies. Dr. Wafik Lotfallah and Professor Mustafa Amer (may his soul rest in peace) for equipping my with many mathematical tools that helped along my path. Finally, my high school teachers: Mr. Ahmed Shams and Dr. Hakeem Hana (may his soul rest in peace) for enlisting in me a love for science and their role in my near-prefect high school national examination score which opened up many opportunities for me.

It is said that no man is useless while he has a friend. I was fortunate to form many friendships that helped me through the most difficult of times. Among many other, I would like to thank them for their friendships and for staying in touch over the years:

From KAUST/Saudi-Arabia: Dr. Hesham Omran (now Professor at Ain Shams University), Dr. Mohammed Affan Zidan (now Post Doc at the University of Michigan), Dr. Mahmoud Ouda, Dr. Amir Nabil (Now with Keysight), Dr. Mohamed Tarek Ghoneim (Now with Intel) and Dr. Mohamed Ahmed Nasr. From GUC and Germany: Dr. Ramy Atawia, Karim Ishak (Uni. Ulm), Ahmed Moheeb, Dr. Ahmed Saleh Mansour, Dr. Muhammed Samir, Islam el Nakib,

Akram Amin and the one and only Abdurrahman Askar who was always there when I needed him the most. From High School: Amr Nabil, Eslam Shanab, and Ehab El Kady.

Last but no means least, I would like to thank my family:

To my sister May, now a mother of three (the twins Ahmed and Layla and the little Mahmoud) all of which came into this world through the course of my Ph.D.: They say that having an older sister is like having a second mother, I could not agree more, thank you for being my second mom. Thank you again for taking care of me during my visit to you in Boston in the Winter of 2019 and for all the delicious food and helping me buy clothes with you wonderful taste.

To my brother Mahmoud, there are no words to express how grateful I am to have you as a brother. It is difficult to imagine how a constantly fighting 5 and 6-year-olds would become such a supportive pillars in adulthood. Mahmoud is not only my younger brother; he is my confidant and partner in crime. We shared everything from child-hood and into adulthood even now we both are both graduate students so we can easily understand and express our happiness and frustrations at times to one another. Mahmoud has always been there when I needed him most, and I know he will always be.

To my parents, Ali and Ola, thank you for sacrificing your comfort and doing everything you can to give us the best education possible. Baba, no son could have asked to a better father. Your dedication, love and joy upon seeing our achievements are things that kept us going despite all the difficulties. You have asked us do our best and that is it. I do hope that this dissertation brings you joy that your life's work is paying off. Mama, I know you paused and eventually left your graduate studies to raise us saying that to you we are worth 1000 PhD's. I do not know about the other 999 but this is one right here and hopefully another one will come in the next 1-2 years from my brother.

The material in this dissertation is based on the following papers which are either published, has been submitted for publication, or contains material that is currently being prepared

for submission for publication.

Chapter 2, is to be submitted for publication of the material as it may appear in: A. Nafe, K. Kibaroglu, M. Sayginer, and G. M. Rebeiz."A Low-Cost Scalable 64-element Single-Polarized Phased-Array for 5G Base Stations". *Antennas and Wireless Prop. Letters*. The dissertation author was the primary investigator and author of this paper.

Chapter 3, in part, is a reprint of the material as it appears in: A. Nafe, M. Sayginer, K. Kibaroglu and G. M. Rebeiz, "2x64 Dual-Polarized Dual-Beam Single-Aperture 28 GHz Phased Array with High Cross-Polarization Rejection for 5G Polarization MIMO", *IEEE International Microwave Symposium (IMS)*, Boston, MA, USA, 2019. The dissertation author was the primary investigator and author of this paper.

Chapter 3 is also a reprint of the material as it appears in: A. Nafe, M. Sayginer, K. Kibaroglu and G. M. Rebeiz, "2x 64-Element Dual-Polarized Dual-Beam Single-Aperture 28-GHz Phased Array With 2x 30 Gb/s Links for 5G Polarization MIMO", *IEEE Trans. Microw. Theory Techn.*, accepted. The dissertation author was the primary investigator and author of this paper.

Chapter 4, in part, is a reprint of the material as it appears in: A. Nafe, K. Kibaroglu, M. Sayginer, and G. M. Rebeiz. "An In-Situ Self-Test and Self-Calibration Technique Utilizing Antenna Mutual Coupling for 5G Multi-Beam TRX Phased Arrays". *IEEE International Microwave Symposium (IMS)*, June 2019. The dissertation author was the primary investigator and author of this paper.

Chapter 4 is also, in full, has been submitted for publication of the material as it may appear in: A. Nafe, Z. Zhang, Y. Yin, M. Sayginer, K. Kibaroglu, and G. M. Rebeiz. "In-Situ Self-Test and Self-Calibration of 5G Multi-Beam Phased-Arrays Leveraging Quadrant-Level Antenna Mutual Coupling". The dissertation author was the primary investigator and author of this paper.

Chapter 5, in part, is a reprint of the material as it appears in: A. Nafe, A. H. Aljuhany,

K. Kibaroglu, M. Sayginer, and G. M. Rebeiz. “In-Situ Self-Test and Self-Calibration of Dual-Polarized 5G TRX Phased Arrays Leveraging Orthogonal-Polarization Antenna Couplings”. *IEEE International Microwave Symposium (IMS)*, June 2020. The dissertation author was the primary investigator and author of this paper.

Chapter 5 also, is to be submitted for publication of the material as it may appear in: “Leveraging Orthogonal-Polarization Antenna Coupling for In-Situ Self-Test and Self-Calibration of 5G Polarization MIMO Phased Arrays ”. *IEEE Trans. Microwave Theory and Tech.*, . The dissertation author was the primary investigator and author of this paper.

The dissertation author was the primary author of the work in these chapters, and coauthors (Prof. Gabriel M. Rebeiz, Dr. Mustafa Sayginer, Kerim Kibaroglu, Abdurrahman H. Aljuhani, Zhe Zhang, and Yusheng Yin) have approved the use of the material for this dissertation.

Ahmed Ali Nafe

La Jolla, California

August 2020

VITA

2012	B. S. in Electrical and Electronics Engineering, German University in Cairo, Egypt
2015	M. S. in Electrical Engineering, King Abduallah University of Science and Technology, Saudi Arabia
2020	Ph. D. in Electrical Engineering (Electronic Circuits and Systems), University of California San Diego

PUBLICATIONS

A. Nafe, Z. Zhang, Y. Yin, M. Sayginer, K. Kibaroglu, and G. M. Rebeiz. "In-Situ Self-Test and Self-Calibration of 5G Multi-Beam Phased-Arrays Leveraging Quadrant-Level Antenna Mutual Coupling". *IEEE Trans. Microwave Theory and Tech.*, (to be submitted).

A. Nafe, A. H. Aljuhany, K. Kibaroglu, M. Sayginer, and G. M. Rebeiz. "Leveraging Orthogonal-Polarization Antenna Coupling for In-Situ Self-Test and Self-Calibration of 5G Polarization MIMO Phased Arrays ". *IEEE Trans. Microwave Theory and Tech.*, (to be submitted).

A. Nafe, M. Sayginer, K. Kibaroglu, and G. M. Rebeiz. "2x64-Element Dual-Polarized Dual-Beam Single-Aperture 28 GHz Phased Array With 2x30 Gbps Links for 5G Polarization MIMO". *IEEE Trans. Microwave Theory and Tech.*, (Accepted).

B. Rupakula, A. Nafe, S. Zihir, Y. Wang, T. Lin, and G. Rebeiz. "63.5-65.5 GHz Transmit/Receive Phased-Array Communication Link With 0.5-2 Gb/s at 100-800 m and +/-50° Scan Angles". *IEEE Trans. Microwave Theory and Tech.*, vol. 66, no. 9, pp. 4108-4120, Sep. 2018.

A. Nafe, A. H. Aljuhany, K. Kibaroglu, M. Sayginer, and G. M. Rebeiz. "In-Situ Self-Test and Self-Calibration of Dual-Polarized 5G TRX Phased Arrays Leveraging Orthogonal-Polarization Antenna Couplings". In IEEE MTTS Int. Microw. Symp. Dig., June 2020 (Accepted).

A. Nafe, M. Sayginer, K. Kibaroglu, and G. M. Rebeiz. "2x64 Dual-Polarized Dual-Beam Single-Aperture 28 GHz Phased Array with High Cross-Polarization Rejection for 5G Polarization MIMO". In IEEE MTTS Int. Microw. Symp. Dig., pp. 484-487, June 2019.

A. Nafe, K. Kibaroglu, M. Sayginer, and G. M. Rebeiz. "An In-Situ Self-Test and Self-Calibration Technique Utilizing Antenna Mutual Coupling for 5G Multi-Beam TRX Phased Arrays". In IEEE MTTS Int. Microw. Symp. Dig., pp. 1229-1232, June 2019.

A. Nafe and G. M. Rebeiz. "On the phase center analysis of linear phased-array antennas". In Proc. IEEE Int. Symp. Antennas Propag. Dig., pp. 2023-2024, July 2017.

J. Myeong, K. Park, A. Nafe, H.Chung, G. M. Rebeiz and B. Min. "A 28-GHz Full-Duplex Front-End and Canceller Using Two Cross-Polarized 64-Element Phased Arrays". In IEEE MTTS Int. Microw. Symp. Dig., June 2020 (Accepted).

K. K. Wei Low, A. Nafe, S. Zihir, T. Kanar, and G. M. Rebeiz. "A Scalable Circularly-Polarized 256-Element Ka-Band Phased-Array SATCOM Transmitter with $\pm 60^{\circ}$ Beam Scanning and 34.5 dBW EIRP". In IEEE MTTS Int. Microw. Symp. Dig., pp. 1064-1067, June 2019.

K. Kibaroglu, M. Sayginer, A. Nafe, and G. M. Rebeiz. "A Dual-Polarized Dual-Beam 28 GHz Beamformer Chip Demonstrating a 24 Gbps 64-QAM 2x2 MIMO Link". In Proc. IEEE Radio Freq. Integr. Circuits, pp. 64-67, June 2018.

B. Rupakula, A. Nafe, S. Zihir, T. W. Lin, and G. M. Rebeiz. "A 64 GHz 2 Gbps transmit/receive phased-array communication link in SiGe with 300 meter coverage". In IEEE MTTS Int. Microw. Symp. Dig., pp. 1599-1601, June 2017.

ABSTRACT OF THE DISSERTATION

Millimeter-Wave Single- and Dual-Polarized 2×2 MIMO Phased Arrays and In-Situ Over-the-Air System-Level Self-Calibration Techniques for 5G Applications

by

Ahmed Nafe

Doctor of Philosophy in Electrical Engineering (Electronic Circuits and Systems)

University of California San Diego, 2020

Professor Gabriel Rebeiz, Chair

This dissertation presents two millimeter-wave phased-antenna arrays at 28 GHz for fifth generation (5G) mobile communication applications as well as techniques for performing in-situ self-test and self-calibration of single- and dual-polarized 5G phased-arrays. First, a scalable 64-element single-polarized transmit/receive phased array is built with 2×2 beamformer chips on a low-cost printed circuit board (PCB). The design emphasis is placed on minimizing the printed circuit board cost, optimizing the cross-polarization performance, and on-grid scalability. The array is capable of scanning ±50° in azimuth and ±45° in elevation at 29 GHz with cross-polarization rejection better than 20 dB. It achieves an effective isotropic radiated power (EIRP) >

50 dBm over a 4 GHz bandwidth from 27 to 31 GHz. Therefore, it is a suitable candidate for Gbps multi-user multiple input multiple-output (MU-MIMO) base-station applications.

Second, a 2×64-element dual-polarized dual-beam phased array for 5G polarization MIMO is built. The phased-array has two 1:16 dual Wilkinson networks and microstrip antennas with rotated feeds for cross-polarization cancellation. The array demonstrates a measured effective isotropic radiated power (EIRP) at Psat of 52 dBm for each beam and is capable of scanning $\pm 50^{\circ}$ in azimuth and $\pm 25^{\circ}$ in elevation with $\geq$28-dB cross-polarization rejection. Simultaneous dual-beam operation is demonstrated with near-ideal patterns for each beam. The array demonstrates independent simultaneously transmitted 2×16-quadrature amplitude modulation (QAM) and 2×64- QAM data streams delivering an aggregate maximum data rate of 2×20 and 2×30 Gb/s, respectively.

Next, the problem of phased-array calibration is considered. Two calibration techniques are developed and tested for calibrating single and dual-polarized 5G phased arrays at 28 GHz. The first technique addresses the calibration of single-polarized phased-arrays in a MU-MIMO hybrid beamforming base station system. The procedure, labeled Quad-BIST, enables built-in self-test (BIST) and self-calibration of the arrays in-situ without having to remove the array from the field. Quad-BIST relies on mutual coupling between antennas in neighboring arrays arranged in Quad-fashion to extract the calibration coefficients and perform channel characterization. Quad-BIST was successfully applied to 5G 28 GHz arrays with 4×4 and 8×8 elements in each quadrant. The results show that Quad-BIST predicts the channel states (gain and phase control) with rms errors of 0.2 dB/2° and 0.4 dB/2.5° for the 4×4 and 8×8 quadrants, respectively, as compared to far-field techniques. The relative channel ratios are found to be within rms errors of 0.8 dB/7.5°. Near-ideal patterns are attained using the quadrant-level calibration for both arrays with side-lobe level's below -20 dB over scan.

The second technique is for the calibration of dual-polarized dual-beam phased arrays. The procedure, labeled (DP-BIST), exploits the mutual coupling between different antennas of

orthogonally polarized beams sharing the same aperture to enable in-situ self-calibration and self-test of the phased array channels of each beam. DP-BIST was applied to a 16-element dual-polarized dual-beam linear phased-array at 29 GHz, and predicted the relative channel states (gain and phase control) with rms errors better than 0.3 dB /3° and the relative channel offsets with rms errors of 0.8 dB /6° over a wide-bandwidth. These results demonstrate its feasibility for use in 5G polarization MIMO phased arrays.

Chapter 1

Introduction

1.1 Millimeter-Wave Phased-Arrays for Fifth Generation Mobile Communication

Millimeter-wave (mm-Wave) phased-arrays systems have attracted a growing attention as a result of its planned deployment in the fifth generation (5G) cellular network [1]. Newly announced 5G new-radio (5G NR) milimeter-wave bands at 28 GHz and 39 GHz allow for an order of magnitude wider-bandwidth communication channels than in the current cellular systems operating at the congested 0.6-3 GHz frequency bands [2]. With this available bandwidth, mm- Wave 5G based-stations are expected to support communication data rates of several Gbps to multiple users with low latency. To enable high data rate communication links to mobile users at few hundred meter distances, the capabilities of phased antenna arrays, such as the high directivity, over-the-air power combining, and beam scan are needed to compensate for the increased path loss at mm-Wave frequencies as well as to provide efficient user-tracking directive links. Also, it is expected that 5G base-stations will deploy massive multiple-input multiple-output (MIMO) phased-array systems supporting multiple directional beams to several mobile users to maximize the cellular network capacity. Although phased arrays have been developed in the early

1970s, their use has been mostly limited to radar applications in military systems due to their complexity and high development and testing costs. For 5G to become commercially feasible, low-cost phased arrays need to be developed so as to meet the 5G requirements and to fulfill the Gbps promise. In this thesis, a low-cost scalable 64-element single-polarized transmit/receive phased-array for 28 GHz 5G multi-user MIMO applications is presented. The array is capable of delivering an EIRP up to 52 dBm and of scanning to more than $\pm 45^{\circ}$ in azimuth and elevation. Different design trade-offs and performance analysis are also presented in detail.

One way to further increase the communication data rate of 5G systems without using additional resources (frequency or time slot) is through polarization diversity. By sending independent data streams at the same frequency and time-slot but on two orthogonal polarizations (horizontal and vertical), the data rate can be effectively doubled. This, however, poses a challenge for phased-array designers as such polarization-MIMO systems require high polarization purity beams and low data-stream cross-coupling during simultaneous operation. This is especially true for high-spectral efficiency modulations such as 16- and 64-QAM waveforms. In this thesis, a dual-polarized dual-beam 2×64-element phased array at 28 GHz with high -polarization isolation demonstrating up to 2×30 Gbps communication links is presented.

1.2 Phased-Arrays Testing and Calibration

An inherent problem in phased arrays which drives its cost, especially at mm-wave frequencies, is the need to calibrate and test the array channels in every gain and phase state for optimal array performance (beam and null-steering, side lobe level control, etc.). In general, phased-array channels exhibit gain/phase variations from element-to-element, and these variations can be either random (due to fabrication and process variation) or systematic (due to routing un-equal line lengths in the different channel paths).

Typically, phased arrays are calibrated and tested in a far-field range requiring a dedicated

large setup, or using a planar near-field scanner which requires the mechanical movement of a probe to sample the array aperture. Using such systems is costly, time consuming, and not applicable during production due to the limited time needed to test a phased array.

An interesting but uncommon way to calibrate an array is through the use of mutual coupling between the antenna elements [3, 4]. This idea was originally developed by [3] which showed that an L-band phased-array radar of circularly symmetric monopole antennas placed on a hexagonal grid can calibrate itself by using antenna coupling. In this thesis, mutual-coupling calibration techniques suitable for application in 5G base stations are presented. Two techniques are developed, the first (Quad-BIST) applies to single-polarized phased arrays and the second (DP-BIST) applies for dual-polarized dual-beam phased arrays. Both techniques were used for comprehensive characterization of 5G phased arrays at 28 GHz showing good calibration performance.

1.3 Thesis Overview

Chapter 2 presents a low-cost scalable 64-element 28-GHz phased-array transceiver for 5G communications based on 2×2 transmit/ receive (TRX) beamformer chips. Sixteen of the 2×2 TRX chips are assembled on a multi-layer printed circuit board (PCB) together with a Wilkinson combiner/divider network and $27-31$ GHz stacked-patch antennas. The phased array can scan to $\pm50^\circ$ in azimuth (H-plane) and $\pm45^\circ$ in elevation (E-plane) with low cross-polarization levels and achieves a saturated EIRP of 52 dBm with 4-GHz 3-dB bandwidth.

Chapter 3 demonstrates a 5G 28-32 GHz 2×64-element dual-polarized dual-beam transmit/receive (TRX) phased array. The array is based on a SiGe 2×4 TRX dual-beamformer chip with 6-bits of phase and 25 dB of gain control. The chip delivers 11-12 dBm/channel in the transmit-mode and has a noise figure (NF) of 4.8 dB in the receive-mode. Sixteen chips are employed for the construction of a low-cost printed circuit board (PCB) based 2×64-element

dual-beam array using flip-chip technology. The phased-array has two 1:16 dual Wilkinson networks and microstrip antennas with rotated feeds for cross-polarization cancellation. The array demonstrates a measured effective isotropic radiated power (EIRP) at Psat of 52 dBm for each beam and is capable of scanning $\pm 50^{\circ}$ in azimuth and $\pm 25^{\circ}$ in elevation with >28 dB cross-polarization rejection. Simultaneous dual-beam operation is demonstrated with near-ideal patterns for each beam. The array demonstrates independent simultaneously transmitted $2\times$16-QAM and $2\times$64-QAM data streams delivering an aggregate maximum data rate of $2\times$20 Gbps and $2\times$30 Gbps, respectively. Also, measurements done over all scan angles at an EIRP of 41 dBm per polarization and 64-QAM waveforms show a data rate of $2\times$4.8 Gbps with an EVM≤ -25 dB. To our knowledge, this is the first demonstration of a dual-polarized, dual-beam phased array for 5G polarization-based multiple-input multiple-output (MIMO) systems with 60 Gbps maximum data rates.

Chapter 4 presents an in-situ self-test and self-calibration technique and its application to 5G phased arrays. The built-in self-test (BIST) procedure, labeled Quad-BIST, enables the relative channel calibration, channel gain/phase characterization and failure detection of 5G phased-arrays. Quad-BIST relies on mutual coupling between antennas in neighboring arrays arranged in Quad-fashion to extract the calibration coefficients and perform channel characterization. The calibration technique was successfully applied to 5G 28 GHz arrays with 4x4 and 8x8 elements in each quadrant. The results show that Quad-BIST predicts the channel states (gain, phase control) with rms errors of 0.2 dB/2° and 0.4 dB/2.5° for the 4x4 and 8x8 quadrants respectively. The relative channel ratios are found to be within rms errors of 0.8 dB/7.5° from their far-field counter-parts for both cases. Experimental results also show that near-ideal uniform-illumination patterns are attained using the quadrant-level calibration for both arrays, and with low-side lobe operation ($<$-20 dB over scan). The technique is all-electronic, requires neither any moving parts nor a far-field range, can be applied for initial calibration as well as for re-calibration in the field (as a result of aging, environmental changes, etc.), and is well suited for 5G MIMO base-station

systems. To our knowledge, this work presents the first demonstration and detailed analysis of in-situ calibration for mm-Wave 5G phased arrays.

In Chapter 5, an in-situ self-test and self-calibration technique for 5G dual-polarized dual-beam TRX phased-arrays is presented. The procedure, labeled dual-polarized built-in self-test (DP-BIST), exploits the mutual coupling between different antennas of orthogonally polarized beams sharing the same aperture to enable relative channel offset extraction, channel gain/phase characterization and failure detection for the channels of each beam. DP-BIST was applied to a 16-element dual-polarized dual-beam linear phased-array at 29 GHz and predicted the relative channel states (gain, phase) with rms errors $\leq$0.2 dB /2.5° and the relative channel offsets with rms errors of 0.8 dB /7°. DP-BIST is all-electronic, and can be done using a single aperture without any assistance from neighboring arrays. It can be used for initial calibration as well as for re-calibration in the field, and is well suited for 5G polarization-based multiple-input multiple output (MIMO) systems.

Finally, Chapter 6 summarizes and concludes the work presented in this thesis. In addition, several suggestions are provided for future work.

Chapter 2

A Low-Cost Scalable 64-element Single-Polarized Phased-Array for 5G Base Stations

2.1 Introduction

The fifth-generation (5G) communication links targets a large increase in mobile communications with data rates in the order of 1-10 Gbps by using the newly available bandwidth at mm-wave bands at 28, 39, and 60 GHz [1]. To overcome the increased path loss at mm-wave bands, the next generation communication links will rely on directive communications, enabled by phased-array techniques. Although phased-arrays have been used for many years for defense applications and satellite communications, their cost needs to be significantly lowered for massive use in 5G applications. This requires the use of highly integrated chips based on silicon technologies (SiGe or CMOS) rather than InP- or GaAs-based modules [5], low-cost printed circuit board (PCB) designs, and a great reduction in testing costs through minimizing the array calibration. A scalable low-cost phased-array, capable of scanning in both azimuth and elevation at mm-wave

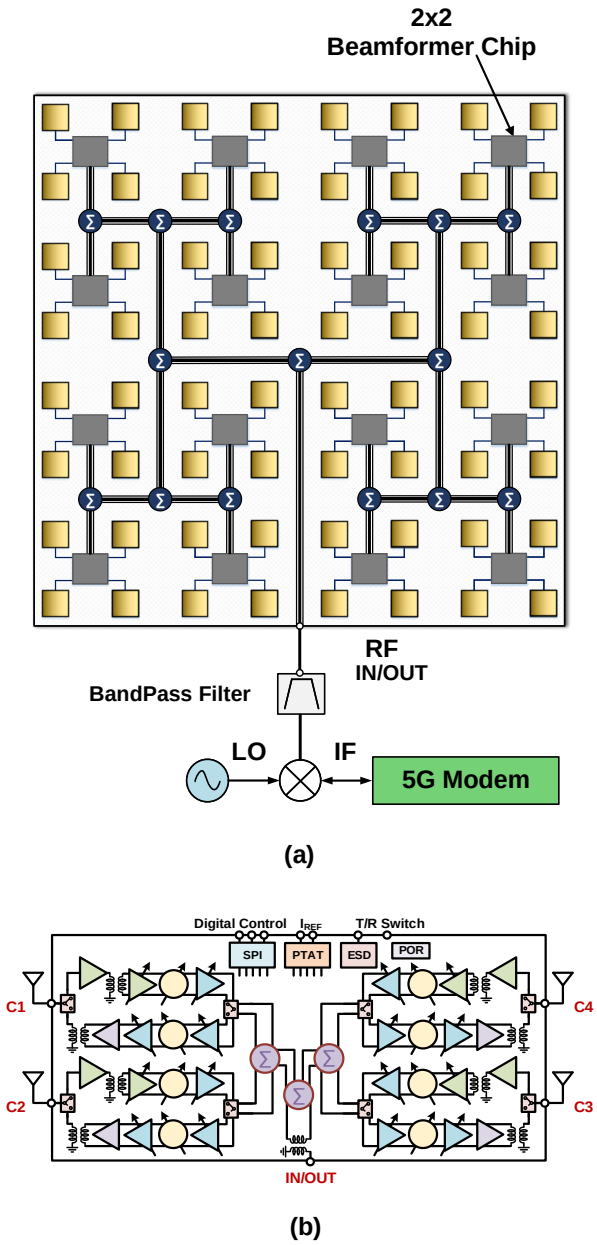

Figure 2.1: Block diagram of (a) 8×8 phased array and (b) 2×2 beamformer chip.

frequencies is needed to deliver Gbps data to several users at a link distance in the order of hundreds of meters. In this chapter, a low-cost and scalable 8×8 28 GHz phased-array suitable for 5G communication links at hundreds of meters for base station applications is presented.

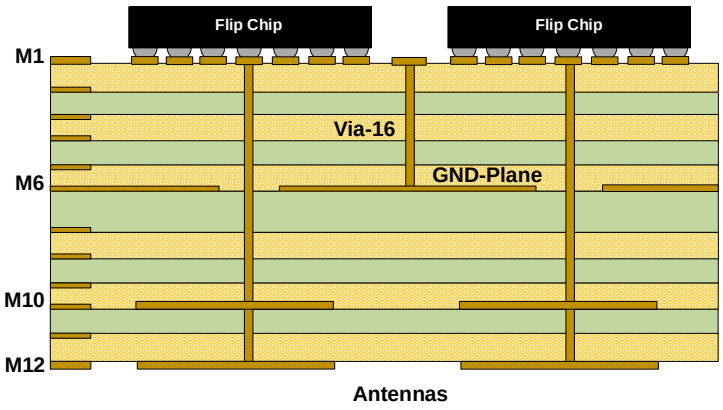

Figure 2.2: Stackup of the low-cost PCB board.

2.2 Phased-Array Architecture

The 28-GHz phased array employs the 2×2 architecture shown in Fig. 2.1(a) with quad-core RF beam-former (Fig. 2.1(b)). The beamformer chips are flipped onto one side of a low-cost PCB and connected to antenna elements on the opposite side of the PCB. There are multiple advantages to this architecture [5, 6]: First, it minimizes the interconnect length between the chips and the antennas which directly affects the transmit EIRP and the receive noise figure. Second, it offers high yield and low assembly costs due to the use of small 2×2 chips with low interconnect count. Third, since the beamforming is done in the RF, no LO and IF routing are needed which reduces the routing complexity on the PCB resulting in less layers and lower PCB cost. Fourth, it helps obtain a uniform heat distribution over the phased array since the chips are distributed evenly over the array aperture area and finally, it allows for using a high-Q filter for blocker rejection before the transciever (Fig. 2.1a).

The phased array is designed on a low cost stack-up based on Megtron-6 ($\varepsilon_r = 3.3$, $\tan\delta = 0.005$ at 30 GHz). The stack-up shown in Fig. 2.2 consists of 12 metal layers (M1-M12). Sixteen beamformer chips are flipped onto the top metal (M1). Layers M1-M2 are dedicated to the RF routing while M3-M4-M5 are used for VDD and digital serial peripheral interface (SPI) routing. Layers M7-M12 are used for antennas and M6 is a full ground plane. The TRX

Table 2.1: Summary of 2×2 beamformer chip performance

Parameter	RX-Mode	TX-Mode
Gain (dB)	17	18
Bandwidth (GHz)	27-31	26-31
NF (dB)	4.8	-
RX-IP1dB/ TX-OP1dB (dBm)	-21	11-12
Phase step (degree)	5.6	5.6
Gain Control (dB)	25	20
Pdc / ch. (mW)	150	220@P1dB

beamformer chip block diagram is illustrated in Fig. 2.1(b). The chip is fabricated in 0.13-μm TowerJazz SBC18H3 SiGe BiCMOS process with flip-chip package and 400-μm pitch balls. The TRX channels contain 6-bit phase shifters and variable gain amplifiers with 20-25 gain control range in the TX and RX modes, respectively. Each channel delivers an output power of 11-12 dBm (OP1dB) at 27-31 GHz in the TX-mode and achieves a noise figure of 4.8 dB in the RX-mode. A summary of the chip performance metrics is given in Table 2.1.

2.3 Antenna Array Design

A stacked-patch antenna is chosen for its ease of integration, and high bandwidth properties. The antenna has a driven patch on M10 and a parasitic patch on M12, the antenna ground plane is M6 (antenna substrate thickness is 30 mil from M6-M12). Different antennas designs were optimized using HFSS in a master/slave environment for operation at 28 GHz. Impedance bandwidth at broadside up to 23% can be achieved with such a design without the need for any matching network. However a negative issue about the maximum bandwidth designs is that the cross-polarization (X-pol) properties degrades quickly with scanning in the H-plane. This is because the cross-polarized currents are imbalanced on the patch due to the probe feed asymmetry. The cross-polarization radiation in the H-plane can be reduced by lowering the patch aspect ratio (W/L), which helps bring the X-pol currents on the non-radiating edges closer to each other, thus leading to cancellation of their radiation component over a larger scan range (Fig. 2.3a). As

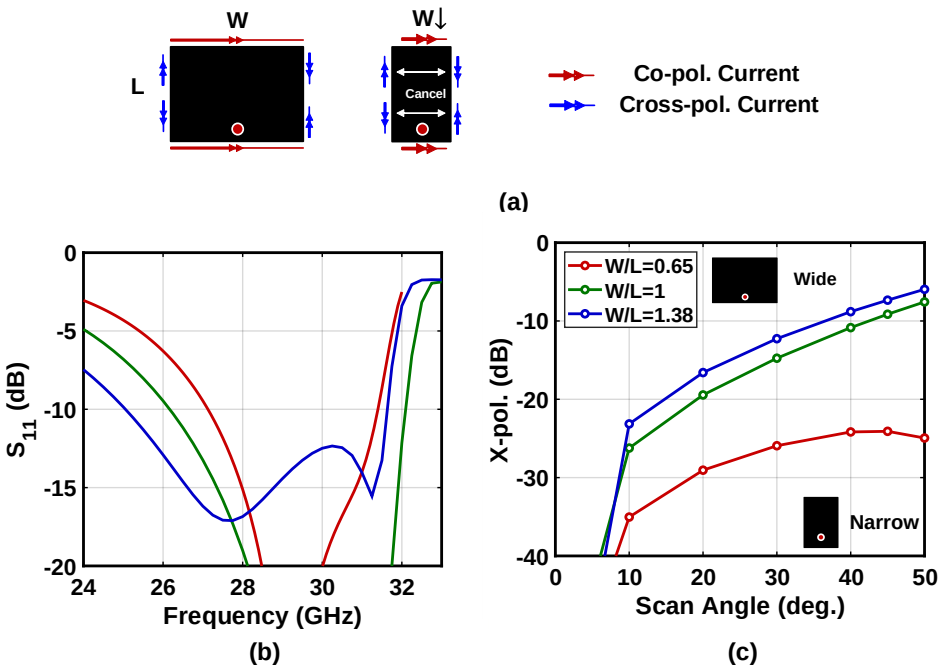

Figure 2.3: Bandwidth and cross-pol. trade-off: (a) Patch antenna equivalent magnetic currents. Simulated (a) S_{11} for patch antennas of different aspect ration and (b) Simulated cross-polarization referenced to the co-polarization level versus scan angle in azimuth (H-plane) at 29 GHz.

can be seen in Fig. 2.3(b,c), for maximum bandwidth is available for an aspect ratio of 1.38 but the X-pol level reaches up to -5 dB when scanned. When the aspect ratio is reduced to 1, the bandwidth shrinks to 20%, whereas the cross-polarization level improves to -8 dB. Finally for an aspect ratio of 0.65, the bandwidth is about 15% but X-pol is less than -25 over scan angle. Since this array has a beamformer chip having a bandwidth from 27-31 GHz (13.8%), using a high bandwidth antenna is not needed and the excess bandwidth can be traded for improved cross-polarization characteristics. Therefore, the design with an aspect ratio of 0.65 and 15% impedance bandwidth is selected.

The antenna is then integrated with a 50 Ω co-axial transition from M1 to M12, and followed by a microstrip line to connect it to the chip on the top metal layer (Fig. 2.4a). An additional quarter wavelength shorted-stub is added to provide elector-static discharge (ESD) protection. Fig. 2.4(b,c) represent the simulated reflection and transmission coefficients when the

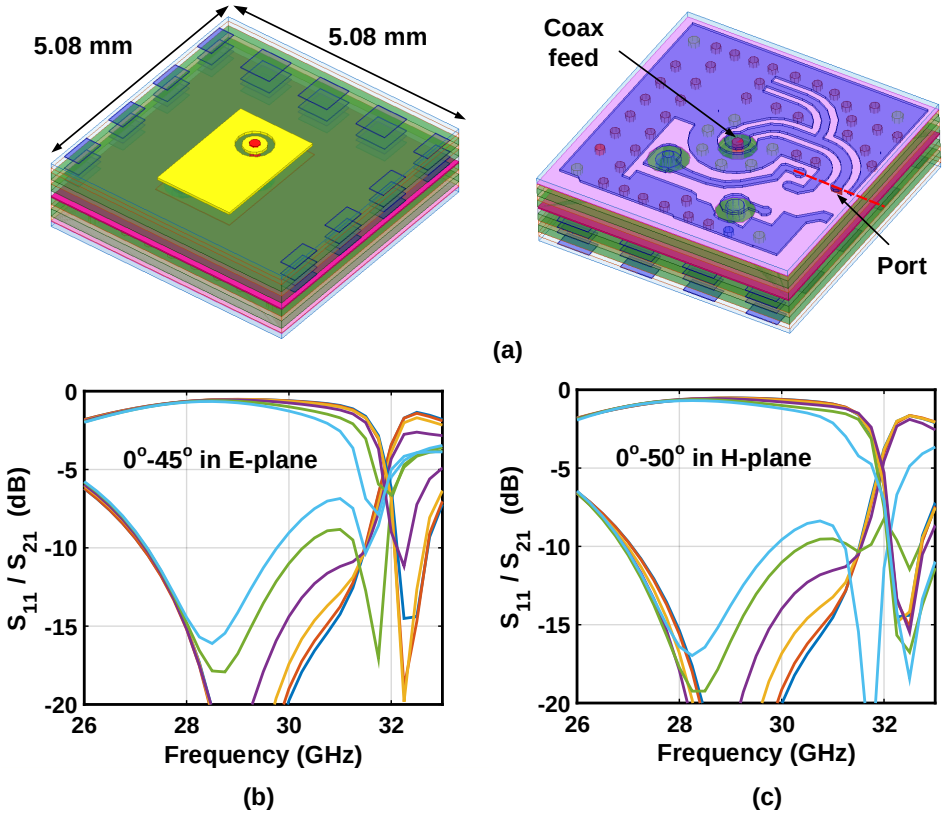

Figure 2.4: (a) Antenna simulation model and coaxial feed. Simulated S_{11} and S_{21} versus scan angle for (b) *E*-plane and (c) *H*-plane

array is scanned to different angles in azimuth and elevation. As can be seen, the array is matched better than -7 dB over scan angles up to $\pm 45^{\circ}$ in the E-plane and up to $\pm 50^{\circ}$ in the H-plane. The scan is limited in the E-plane by the onset of blindness at high frequencies. In the H-plane, the array scanning is grating-limited.

Since it is desired that the phased array module be scalable to larger sizes via tiling, it is important to know how sensitive is the resulting combined pattern to aperture gaps. These gaps are usually present to facilitate routing inside the array PCB. The scenario is shown in Fig. 2.5, with four 8×8 arrays tiled together. In the first case, Fig. 2.5a, the arrays are tiled exactly on-grid and thus effectively forming a contiguous 16×16 array. In the second case, an additional 2λ empty gap is placed in-between the 8×8 arrays (Fig. 2.5b). It can be observed that the side lobe levels in the second case is much worse, and in particular, the first side lobe increases from

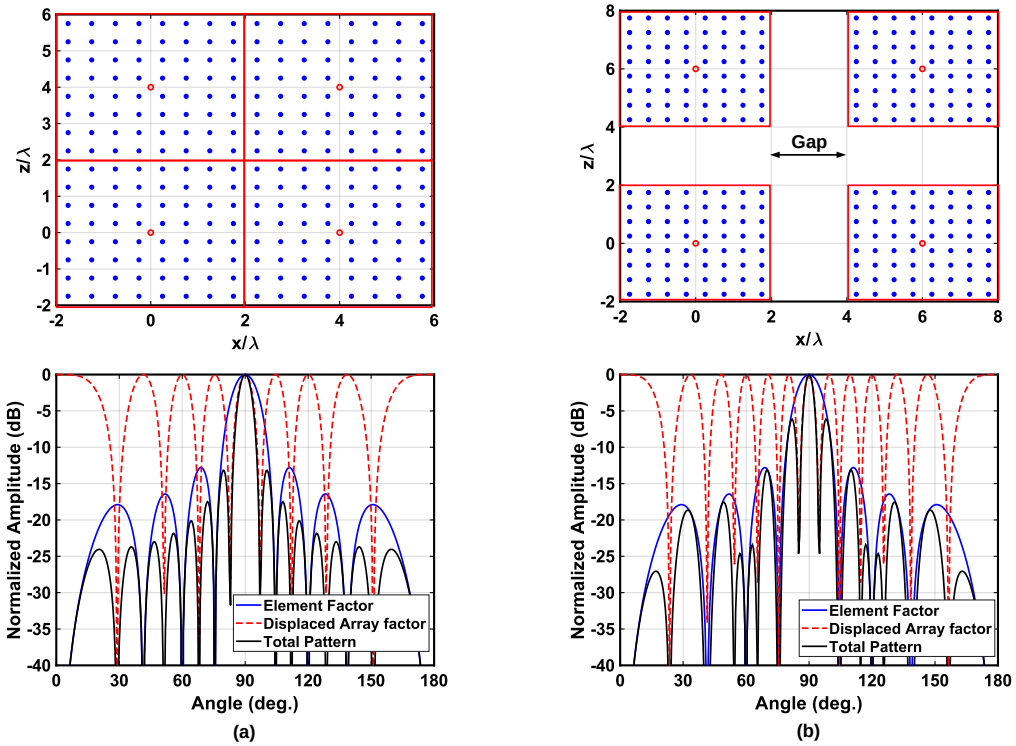

Figure 2.5: Simulated tiled 16×16 array patterns using 8×8 arrays: (a) without gap and (b) with extra 2λ gap between the 8×8 arrays.

the ideal level -13.2 dB to -6 dB. The reason for this can be understood by examining the array-factor (2×2) and the element factor (8×8 EF) for both cases. In the first case, the phase centers of the arrays are 2λ apart and the 2×2 array factor peaks and aligns with the EF (8×8 array at 0.5λ spacing) nulls. However in the second case, the phase centers of the 2×2 array factor become 2.5λ apart. This shifts the array factor peaks from the 8×8 EF nulls leading to a higher side-lobe level. Fig. 2.6 illustrates the side-lobe level for different array-tiling gaps, it can be seen that to maintain side-lobes better than -10 dB, the gap cannot exceed 0.5λ and it is preferred to keep it as low as possible ($\leq 0.2\lambda$) for sub-1 dB side-lobe level degradation.

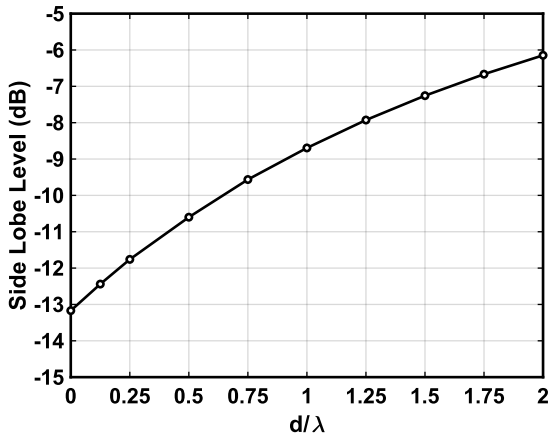

Figure 2.6: Simulated 16×16 side lobe level versus tiling gap.

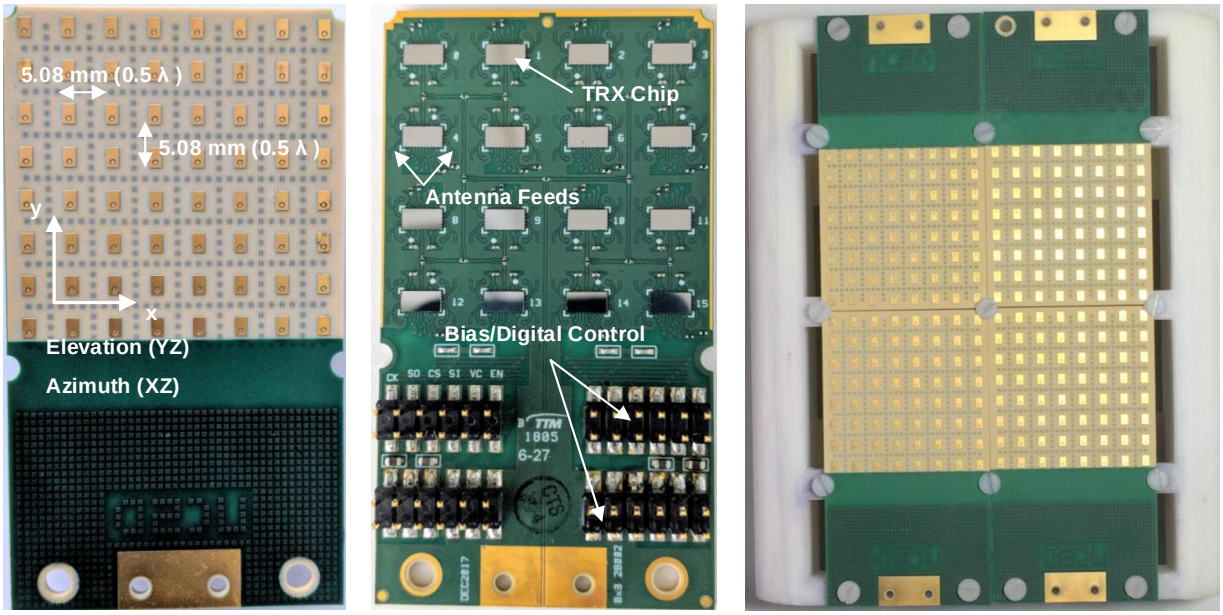

Figure 2.7: Phased array photo: (a) 8×8 antenna side (4.06×4.06 cm^2), (b) 8×8 chip-side and (c) tiled four 8×8 arrays to form a 16×16 array aperture (8.1×8.1 cm^2).

2.4 Measurements

2.4.1 Broadside Frequency Response, EIRP, and Electronic Gain

The fabricated scalable 8×8 phased array is shown in Fig. 2.7(a,b). The array has an aperture of 4.06×4.06 cm^2 and can be scaled to any $16 \times$N size by direct side-by-side tiling as

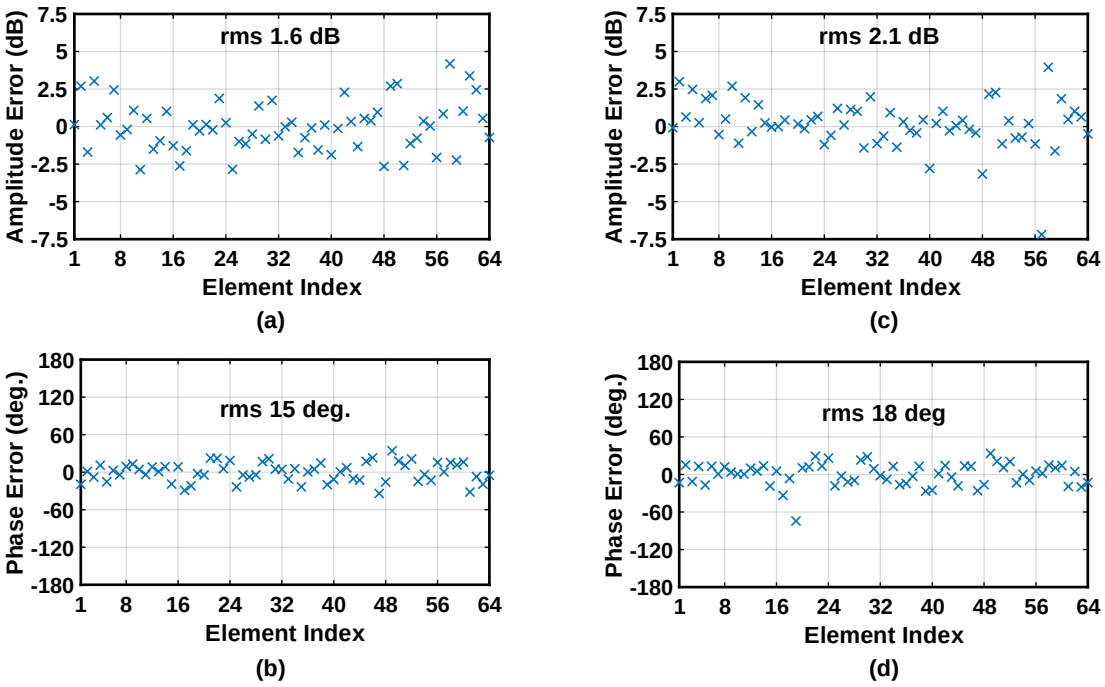

Figure 2.8: Measured channel relative amplitudes and phases in: (a,b) TX-mode and (c,d) RX-mode.

shown in Fig. 2.7(c). The antenna spacing is 0.5λ in azimuth and 0.5λ in elevation at 30 GHz. Ideally, there are no extra offsets in between the tiled arrays, but in practice, there could be up to ($\pm$10 mils) due to the PCB cut-boundary tolerance. However, this is electrically very small at 29 GHz ($\sim \lambda_\circ/40$) and thus does not affect the side-lobe level. Moreover, the ground-planes on each array are exposed at the edges of the top metal layer to allow for ground plane stitching between the neighboring array tiles. This is advisable to do in order to prevent diffraction radiation of ground-plane currents at the ground edges of the individuals arrays.

The 8×8 array is characterized using a far-field measurement set-up with a vector-network analyzer and a standard gain horn at a distance of 1.1 m. The channels were first measured individually, and are found to be mostly within $\pm$2.5 dB and $\pm 30^\circ$ of each other (see Fig. 2.8) indicating an acceptable alignment for uniform illumination purposes. The broadside frequency response in the RX and TX mode (at $\geq$ 10 dB back-off) was measured with all the channels at their maximum gain state (Fig. 2.9a). The 3-dB gain-bandwidth in the RX-mode

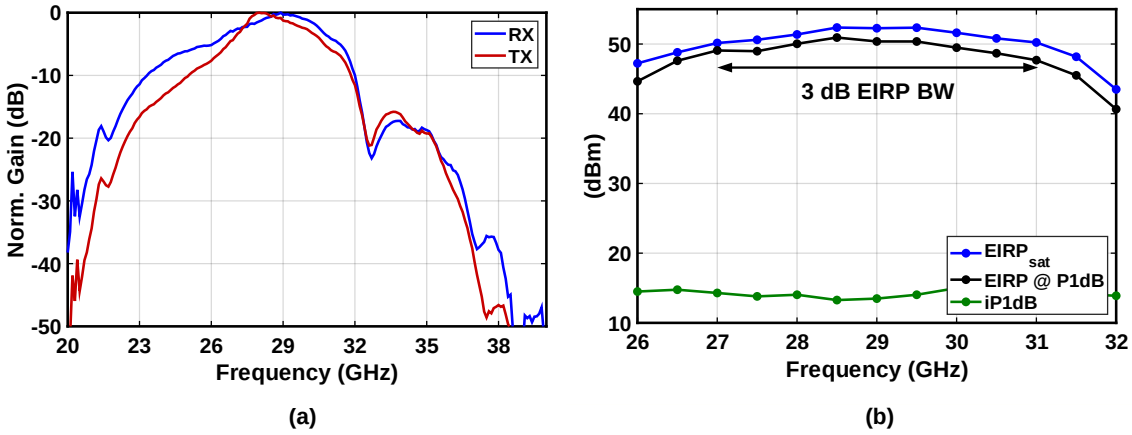

Figure 2.9: Measured broadside: (a) Frequency in TX/RX modes and (b) TX EIRP (at Psat and P1dB) and array input compression point.

extends from 26.7 GHz to 30.7 GHz, and is from 27.2 GHz to 30.2 GHz in the TX mode. The effective isotropic radiated power (EIRP) at broadside is shown in Fig. 2.9b. The 8×8 array demonstrates an EIRP of 52 dBm at Psat with a 3dB-EIRP bandwidth of 4 GHz around 29 GHz. The measured peak EIRP at P1dB is 50.5 dBm which agrees with calculations ($\text{EIRP}_{\text{P1dB}}$=20log$N$ $+\text{P}_{\text{t-P1dB}}+\text{G}_{\text{ant}} = 36 + 11.5 + 4 = 51.5$ dBm). The antenna gain is assumed to be 4 dB, which corresponds to a 5.2 dB directivity and 1.2 dB of antenna and transmission-line loss.

The array simplified block-diagram is shown in Fig. 2.10. The TX gain is defined as EIRP of the array divided by the input power written as:

$$\text{G}_{\text{TX}} = \frac{\text{EIRP}}{P_{\text{in}}} = 50.5 - 13.5 = 37 \text{ dB} \tag{2.1}$$

The RX- electronic gain is defined as the ratio of the output power at the RF-connector (P_{out}) to the total power collected by the array aperture and is expressed as:

$$\text{G}_{\text{RX}} = \frac{\text{P}_{\text{out}}}{\text{S}_{\text{inc}} \times \text{Area}} = -1.2 + 17 - 4 - 3.9 = 7.9 \text{ dB} \tag{2.2}$$

where S_{inc} is the incident plane-wave power, Area is the phased array aperture area. Assuming a

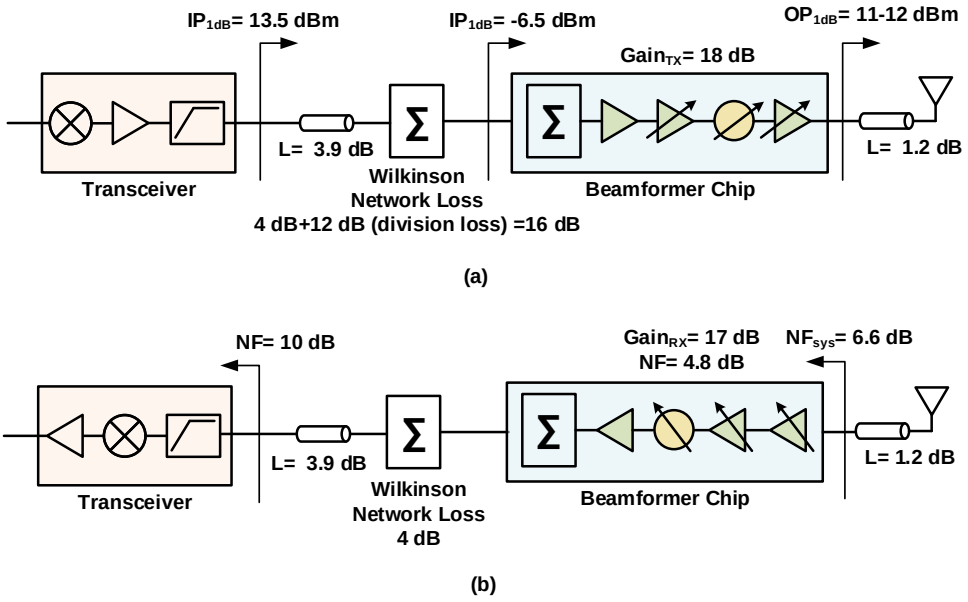

Figure 2.10: Block diagram of system analysis: (a) TX mode and (b) RX mode.

filter and transceiver with a 10 dB noise-figure, the system noise figure referred to the chip input port becomes 6.6 dB.

2.4.2 Radiation Patterns, EIRP versus Scan and Performance Summary

The measured scanned patterns are shown in Fig. 2.11 in the RX mode at 29 GHz. The array is capable of scanning $\pm 50^{\circ}$ in azimuth (H-plane) with a scan drop less than 4 dB. In the elevation plane (E-plane), the array scans up to $\pm 45^{\circ}$ with less than 3.5 dB scan drop. In all cases, the side lobes remain below -10 dB and can be improved by 1-2 dB by calibrating the elements to an rms level better than 1 dB/ 10°. The measured co- and cross-polarization patterns in the principle planes are shown in Fig. 2.12. In the E-plane, the X-pol remains below -30 dB for all scan angles, and in the H-plane it is better than -25 dB over all scan angles.

Fig. 2.13 illustrates the measured EIRP at Psat versus scan angle at different frequencies in the principle planes. At 29 GHz, the peak EIRP drops from 52 dBm at broadside to 48 dBm at the maximum scan angles in the azimuth and drops to 47.5 dBm at the maximum scan angles

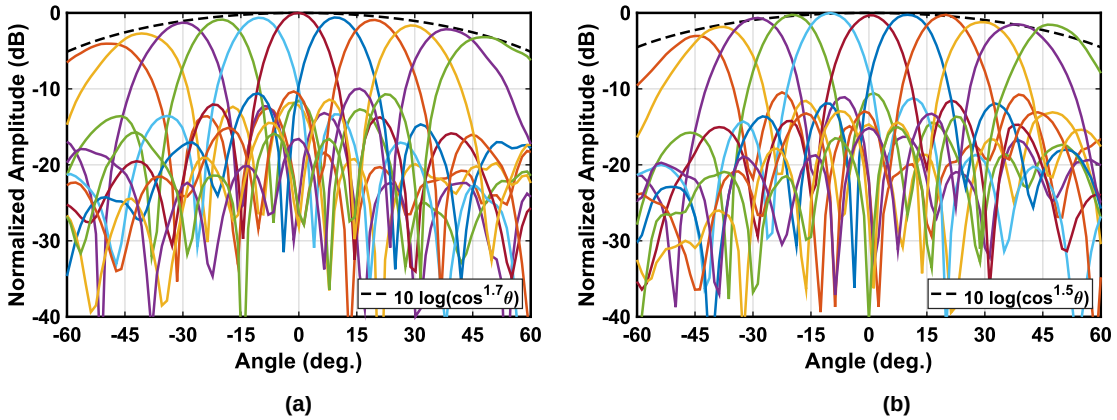

Figure 2.11: Measured radiation patterns in RX-mode at 29 GHz scanned in: (a) Azimuth (H-plane) (b) Elevation (E-plane).

Table 2.2: Array Performance Summary

Parameter		**Value**	
Number of elements, N		64 (8×8)	
Antenna S_{11} bandwidth (GHz)		27-31	
Antenna spacing, d_x / d_y (mm)		5.1 / 5.1	
Feed + antenna ohmic loss (dB)		1.25	
Antenna Gain G_{TRX} (dB)		21.8	
PCB Beamformer ohmic loss (dB)		7.9	
RX Mode		**TX Mode**	
Chip NF (dB)	4.8	Channel NF (dB)	11
System NF (dB)	6.6	EIRP at P1dB (dBm)	50.5
IP_{1dB} / ch. (dBm)	-21	Array IP_{1dB} (dBm)	11-12
P_{dc} (Watts)	9.7	P_{dc} (Watts)	14.3

in elevation. At 27 GHz, the drop is less due to the less directive element factor, and the EIRP drops from a peak value of 50 dBm to 47 dBm in both the azimuth and elevation planes. At 31 GHz, the EIRP drops from 50 dBm at broadside to 46 dBm in the azimuth plane and about 45.5 dBm in the elevation plane. The scan drop is expectedly the highest at 31 GHz due to the more directive element factor ($D \propto 1/\lambda^2$ for a constant area). It can be noticed that in the E-plane, at 31 GHz, there is a sharp drop at $\pm 50^\circ$ which signifies the onset of blindness and is expected from simulations. A summary of the main array performance metrics is shown in Table 2.2.

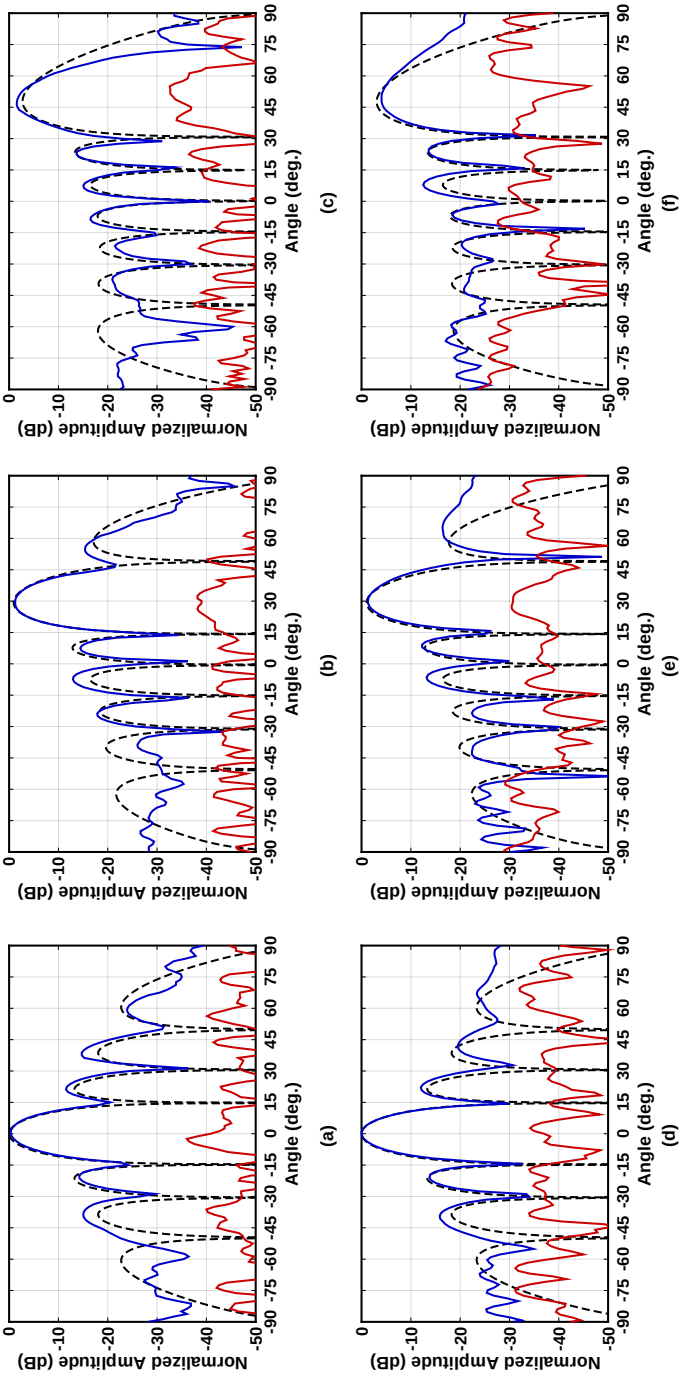

Figure 2.12: Measured co- and cross-polarized scanned patterns in RX-mode at 29 GHz in: (a) Azimuth (H-plane) (b) Elevation (H-plane).

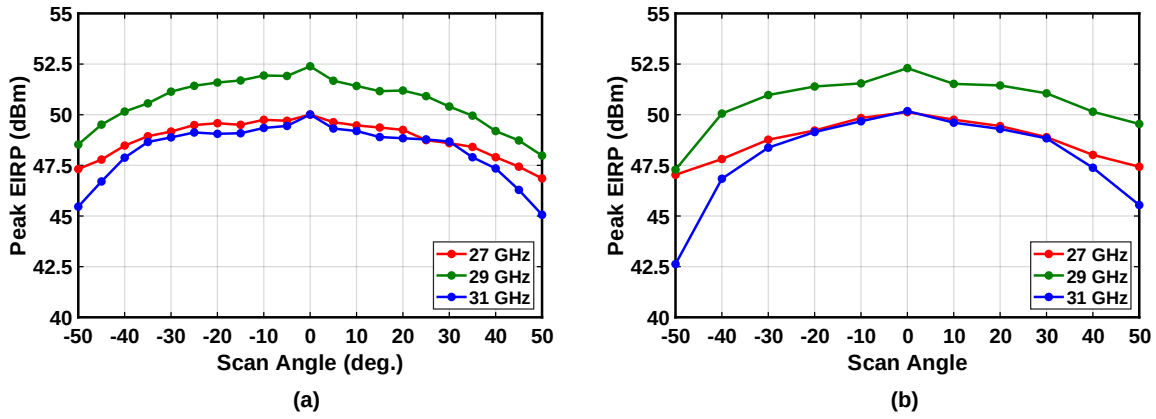

Figure 2.13: Measured EIRP at Psat versus scan angle in: (a) Azimuth (H-plane) and (b) Elevation (E-plane).

2.5 Conclusion

In this chapter, a scalable single polarized 8×8 phased array is developed for 5G base-stations at 28 GHz. The array employs a periodic 2×2 unit cell architecture with quad-core beamfomer chips and is implemented in a low-cost PCB that includes the chips, integrated antennas, and a Wilkinson beam-forming network. Design trade-offs for microstrip patch antennas is presented and the effect of array scaling in the presence of a tiling-gap in the aperture is studied. The presented array achieves an EIRP at P1dB of 50.5 dBm and scans over $\pm 50^{\circ}$ in azimuth and $\pm 45^{\circ}$ in elevation with cross-polarization level less than -25 dB. The array is easily scalable to larger size ($16 \times$N) for increased communication range or for narrower beam formation through tiling, making it a suitable candidate for 5G base-station applications.

2.6 Acknowledgement

This work was supported by Keysight. Technical assistance was provided by Rockwell Collins.

Chapter 2, is to be submitted for publication of the material as it may appear in: A. Nafe, K. Kibaroglu, M. Sayginer, and G. M. Rebeiz."A Low-Cost Scalable 64-element Single-Polarized

Phased-Array for 5G Base Stations". *Antennas and Wireless Prop. Letters*. The dissertation author was the primary investigator and author of this paper.

Chapter 3

2×64-Element Dual-Polarized Dual-Beam Single-Aperture 28 GHz Phased Array for 5G Polarization MIMO

This chapter presents a 5G 28-32 GHz 2×64-element dual-polarized dual-beam transmit/receive (TRX) phased array. The array is based on a SiGe 2×4 TRX dual-beamformer chip with 6-bits of phase and 25 dB of gain control. The chip delivers 11-12 dBm/channel in the transmit-mode and has a noise figure (NF) of 4.8 dB in the receive-mode. Sixteen chips are employed for the construction of a low-cost printed circuit board (PCB) based 2×64-element dual-beam array using flip-chip technology. The phased-array has two 1:16 dual Wilkinson networks and microstrip antennas with rotated feeds for cross-polarization cancellation. The array demonstrates a measured effective isotropic radiated power (EIRP) at Psat of 52 dBm for each beam and is capable of scanning $\pm 50^{\circ}$ in azimuth and $\pm 25^{\circ}$ in elevation with >28 dB cross-polarization rejection. Simultaneous dual-beam operation is demonstrated with near-ideal patterns for each beam. The array demonstrates independent simultaneously transmitted 2×16-QAM and 2×64-QAM data streams delivering an aggregate maximum data rate of 2×20 Gbps and 2×30

Gbps, respectively. Also, measurements done over all scan angles at an EIRP of 41 dBm per polarization and 64-QAM waveforms show a data rate of 2×4.8 Gbps with an EVM≤ -25 dB. To our knowledge, this is the first demonstration of a dual-polarized, dual-beam phased array for 5G polarization-based multiple-input multiple-output (MIMO) systems with 60 Gbps maximum data rates.

3.1 Introduction

Millimeter-wave fifth-generation (5G) new radio (NR) systems currently employ spectrum around 28, 39 and 60 GHz using phased-arrays that can deliver >10 Gbps of data to each user with low latency [1, 6–8]. To further increase capacity without increasing the modulation order, which comes at the cost of reduced effective isotropic radiated power (EIRP) and very low phase noise requirements, polarization-based multiple-input multiple-output (MIMO) systems are proposed in the 5G standard. Such systems are also suitable for line-of-sight links with little reflections between the base-station and the user.

A simple way of achieving a polarization MIMO system is to employ two separate phased arrays at the user terminal, one oriented in the vertical-polarization and the other oriented in the horizontal-polarization [9]. The use of two separate apertures with single-polarized vertical and horizontal antennas in each aperture, instead of a single-aperture with dual-polarized antennas, eliminates a major coupling path between the vertical (V) and horizontal (H) streams. This leads to preserving signal integrity and achieving a low system error-vector-magnitude (EVM).

There is, however, a great value in sharing the same antenna for both V- and H- streams since this would allow a reduction in the system cost and the use of half of the aperture size. Fig. 3.1 presents the architecture of such an array based on 2×4 dual-polarized dual-beam transmit/receive (TRX) beamformer chips feeding dual-polarized antennas [8]. Two independent Wilkinson beamforming networks are placed on the printed circuit board (PCB) to scale the array

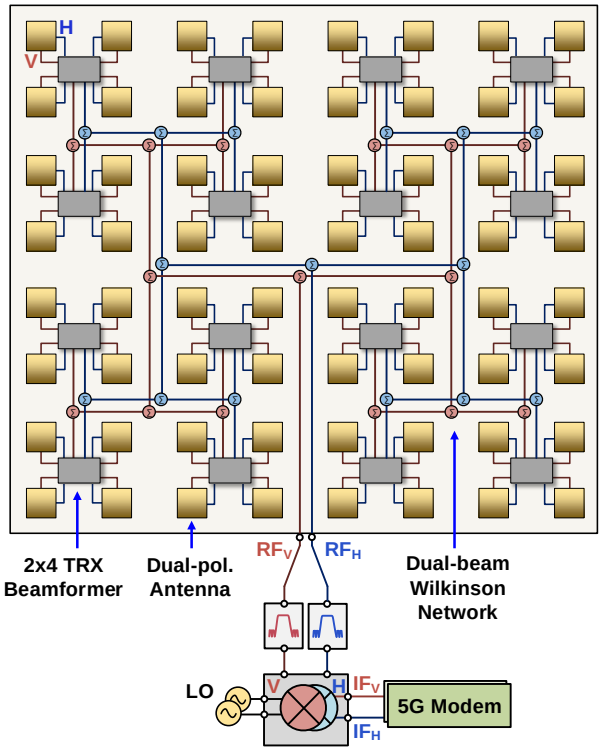

Figure 3.1: Block diagram of 2×64-element dual-polarized dual-beam 5G phased-array.

to any size as required by the system specifications. Two transceivers are then placed at the sum port, and bandpass filters are used to further reduce the local oscillator (LO) and image signal leakage [5, 6].

A 2×2 dual-polarized (DP) MIMO link introduces several challenges that must be addressed at the chip, PCB and antenna levels. At the chip level, it is critical to isolate the V- and H- channels and also, the on-chip 1:4 Wilkinson networks, and to maintain the same chip performance (such as output power, noise figure (NF), gain) when the V- and H- channels are turned on together. This generally doubles the chip power consumption, and therefore, it is important to characterize the chip with all channels turned on.

At the PCB level, the Wilkinson beamforming networks should be well isolated to maintain signal purity between the two independent data streams. This can be achieved by placing Wilkinson networks on different metal levels with ground planes in between as detailed in Section

3.3.3. The antenna must be designed to have low coupling between the V and H feeds and to maintain a low cross-polarization levels over the scan range (see Section 3.3.2).

This work expands on [10] and addresses these challenges to achieve 2×2 DP-MIMO links without any polarization equalization (generally done at the digital signal processing (DSP) level in the modem). Also, this work investigates the performance of DP-MIMO links when both beams are scanned over space to the same user, a feature which has not been presented in prior work [8, 9, 11–15].

3.2 Cross-Polarization and Self-Interference

Fig. 3.2a illustrates a DP-MIMO link where a transmit array is radiating V & H-beams in the broadside direction. A critical aspect in such communication systems is the radiated polarization purity. The V-to-H cross-polarization component acts as an interferer to the H-stream and vice versa for H-to-V coupling, and increases the EVM. Fig. 3.2b presents the system EVM degradation for different cross-polarization levels. In general, channel measurements and DSP in the modem can correct for much of these effects, and one should strive for a cross-polarization level of -20 dB to achieve near-ideal performance with DSP correction (such as 3% EVM). Still, it is important to achieve as low cross-polarization level as possible to operate both data streams at their maximum capacity without much correction.

3.3 2×64-Element Dual-Polarized Dual-Beam Phased-Array Design

The 2×64-element phased-array is designed on a low-cost PCB based on the Megtron-6 substrate (ε_r=3.3, $\tan\delta$=0.005 at 30 GHz). The stack-up in Fig. 3.3a incorporates 12-metal layers (M1-M12). The array employs a 2×4 SiGe beamformer-based unit-cell architecture as shown

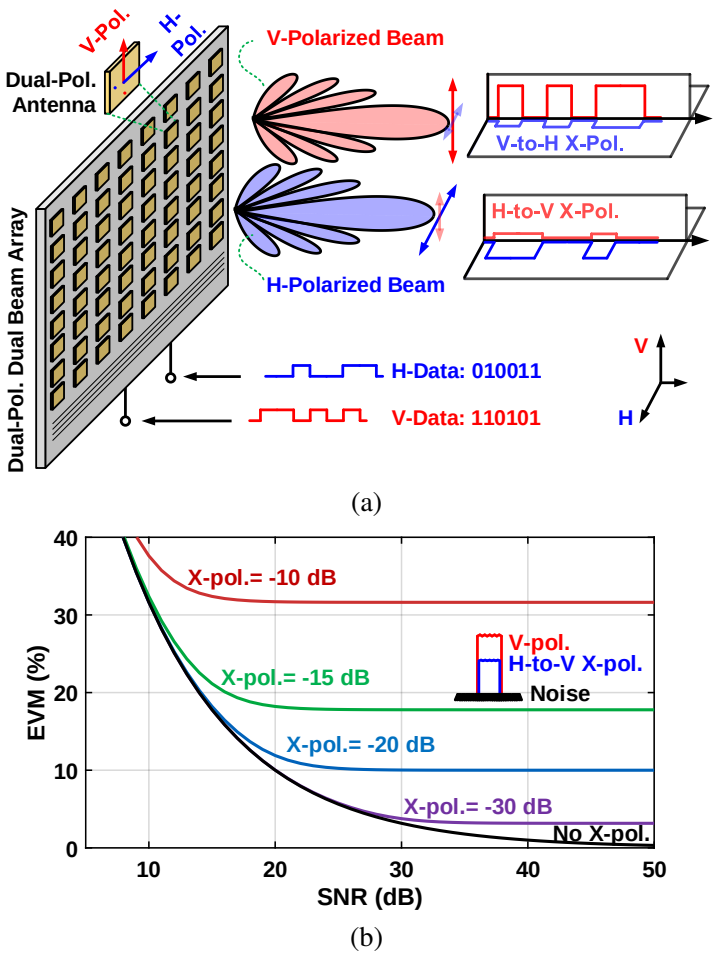

Figure 3.2: (a) Self-interference via cross-polarization coupling in a dual-polarized dual-beam array, and (b) EVM versus signal-to-noise ratio (SNR) at different cross-polarization levels.

in Fig. 3.1 where the 16 beamformer chips are flipped onto the top metal layer (M1). Layers M1-M5 are dedicated to the RF and digital SPI routing, while layers M7-12 are used for the antenna placement with M6 serving as the ground plane.

3.3.1 2×4 TRX Beamformer Chip

Fig. 3.3b presents the block diagram of the 2×4 TRX beamformer chip fabricated in the 0.13-μm TowerJazz SBC18H3 SiGe BiCMOS process with a flip-chip package and 400 μm pitch balls [8]. Each beamformer contains 8 TRX channels with dual Wilkinson networks to combine

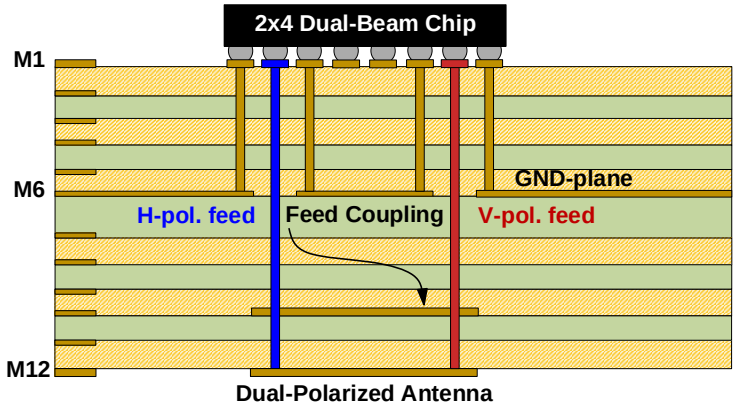

(a)

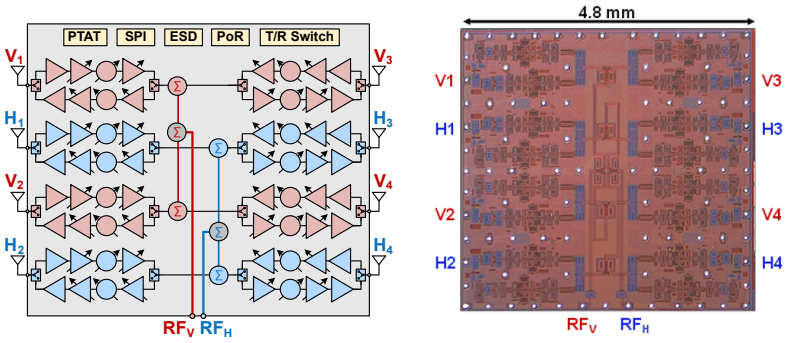

(b) (c)

Figure 3.3: (a) Low-cost PCB stack-up. 2×4 TRX beamformer chip (b) block diagram, and (c) microphotograph (4.8×4.8 mm^2).

four channels into two common ports for dual-beam operation. The TRX channels contain 6-bit phase and 20-25 dB gain control in the transmit (TX) and receive (RX) modes with low rms phase and amplitude errors [8]. The chip has 18 dB gain, 4.8 dB NF and -21 dBm IP1dB in the RX mode at 28-32 GHz, and the IP1dB can be increased to -7 dBm at the lowest gain setting. In the TX mode, the chip has a gain of 21 dB and delivers 11-12 dBm/channel at P1dB at 28-32 GHz. The chip features ESD protection on all dc and control pads, fast T/R switching (<100 ns), on-chip PTAT current generation, power-on-reset (PoR) circuitry and a 4-wire serial peripheral interface (SPI). The chip photo is shown in Fig. 3.3c and its performance metrics are summarized in Table 3.1.

Table 3.1: Summary of the 2×4 dual-beam chip

Parameter	RX-Mode	TX-Mode
Gain (dB)	18	21
Bandwidth (GHz)	28-32	28-32
NF (dB)	4.8	-
RX-IP1dB/ TX-OP1dB (dBm)	-21	11-12
Phase step (degree)	5.6	5.6
Gain Control (dB)	25	20
Pdc / ch. (mW)	150	220@P1dB

3.3.2 Antenna Design and Cross-Polarization Suppression

The antenna element is a probe-fed dual-polarized stacked-patch, with a driven element on M10 and a parasitic element on M12 to improve the bandwidth (Fig. 3.4a). The antennas are placed in a rectangular grid with a spacing of 5.08 mm $\times$ 6.3 mm ($0.5\lambda \times 0.62\lambda$ at 29.5 GHz) to scan up to $\pm 50^\circ$ and $\pm 25^\circ$ in the azimuth and elevation planes, respectively, for both vertically- and horizontally-polarized beams.

The antenna is first optimized using Ansys HFSS in a master/salve environment (infinite-periodic-array simulation) for operation in the 28-32 GHz band. By adjusting the amount of coupling between the patches and their respective resonance frequencies, a dual-resonance matching characteristic could be attained. Both patches are square for dual-polarization operation. An offset co-axial via feed is used to obtain an impedance level close to 50 Ω.

Fig. 3.4 presents the simulated transmission and reflection coefficients of the V- and H-ports to V- and H- plane waves, respectively. Both polarizations are matched with S_{11}<-10 dB at 27.5-32 GHz and with a transmission coefficient (includes ohmic and mismatch losses) of <1 dB at broadside. As the array is scanned up to $\pm 50^\circ$ in azimuth and $\pm 25^\circ$ in elevation, S_{11} remains <-6 dB. At 31.5-32 GHz, the scan is limited to $\pm(45^\circ$-$40^\circ)$ and $\pm(22^\circ$-$20^\circ)$ in the E-plane (azimuth of H-pol. and elevation for V-pol.) due to effects associated with scan-blindness (TM_0 onset). Note that the cross-polarization values and S_{11} and S_{22} values will be improved when feed-rotation is employed on a sub-array level.

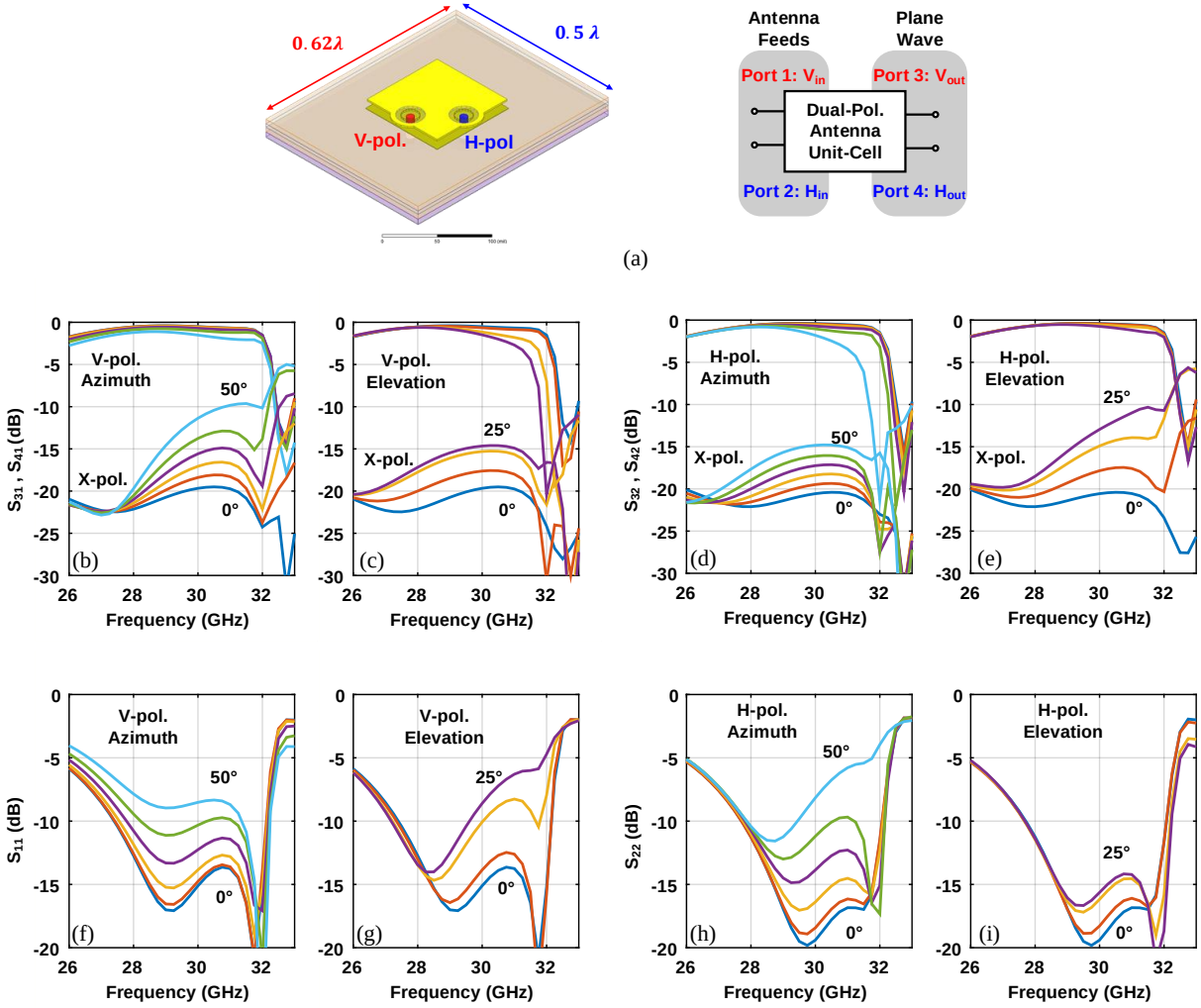

Figure 3.4: (a) Stacked patch antenna unit-cell and simulation results: (b)-(e) transmission coefficients and (f)-(i) reflection coefficients for different scan angles in azimuth and elevation planes for V- and H-polarizations.

As can be seen in Fig. 3.4(a-d), the cross-polarization rejection is only 18-19 dB at broadside and 10 dB when scanned to the edge of the H-plane range (azimuth for V-pol. and elevation for H-pol). One of the limiting factors is the coupling between the two V and H feed probes. This coupling occurs in the feed portion between the antenna and the ground plane (M6-12) where the vias are in close proximity without a ground shield. The coupling between the V and H probes in the same antenna is -18 dB and is much higher than the couplings between the V and H probes of neighbouring antennas (< -33 dB). Another factor contributing to cross-

polarization and which becomes dominant at large scan angles in the H-plane is the magnitude and phase imbalance of the cross-polarized magnetic currents on the non-radiating edges of the patch antenna. This imbalance is created due to the square patch symmetry-perturbation introduced by the presence of the feeding probes [16].

One method to improve the cross-polarization rejection of a dual-polarized patch antenna is to feed both polarizations differentially [17–23]. However, such a feed would require two baluns per antenna and needs to be implemented inside the extremely crowded unit-cell area. Also, if differential signaling is used on the chip RF ports, then this would require double the number of RF bumps per port thus increasing the chip area and cost. Also, four signal lines would need to be routed per antenna. This makes it very challenging for 2-D dual-polarized phased-arrays but feasible when a single antenna element is used [22, 23].

Another way to realize high polarization-purity antennas is with the use of sub-array design techniques [24]. This is commonly found in wideband circularly-polarized arrays using sequential feed-rotation [24–26] and was also adapted to non-scanned dual-linear arrays [27]. In this work, a sub-array feed-rotation technique is utilised and its cross-polarization performance under scanned conditions is investigated.

In order to improve the phased-array cross-polarization performance, a modified 2×2 sub-array is used (Fig. 3.5). In this design, antenna element A is mirrored along the x-axis and then elements (A,B) are mirrored along the y-axis. This gives the net effect of having the feeds rotated by 90° clock-wise within a 2×2 cell. For V-polarization operation, elements (B,C) are excited with a current I_v while elements (A,D) are excited with a 180° out of phase current ($-I_v$) due the flipping of the feed locations. Looking at the parasitically induced components on the H-polarization feed of each antenna, it is observed that elements (A,B) will have the same H-feed current excitation but with opposite sign ($i_H^B = -i_H^A = C_{VH} I_v$). Since the H-feeds of antennas (A,B) have the same relative location (non-flipped) and with current excitations equal and opposite, the radiated cross-polarized fields of antennas (A,B) will cancel at all angles. Additionally, the

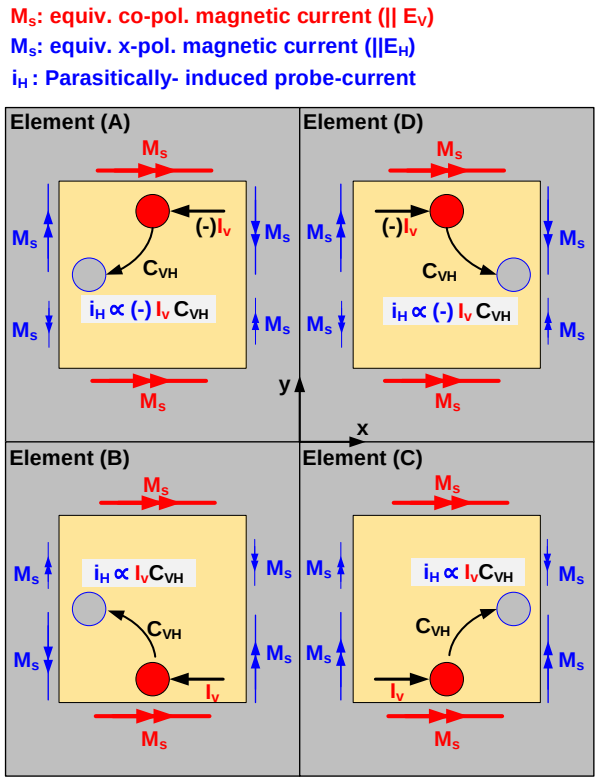

Figure 3.5: Cancellation of feed-probe coupling and cross-polarization components in a 2×2 rotated-feed sub-array for a V-pol. excitation.

unbalanced cross-polarized magnetic currents on the non-radiating edge of antenna (A) is balanced out by corresponding ones in antenna (B) and this prevents cross-polarization degradation when scanning in the H-plane (xz-plane in Fig. 3.5) [16]. A similar argument could be made for the H-pol. excitation and scanning in the yz-plane.

To verify the proposed operation, a 2×8 finite array was simulated in HFSS with an interelement spacing of 0.5λ and 0.62λ in the azimuth and elevation planes (Fig. 3.6). The cross-polarization rejection at the beam pointing angle is plotted in Fig. 3.6e for the rotated-feed case, and is >60 dB for all scan angles. The co-polarized patterns for the rotated and regular feeds cases are almost identical except for some increase in the E-plane far-out side-lobes at ∼-20 dB level. The realized gain of the 2×8 finite array is shown in Fig. 3.7. It is shown that feed-rotation results in well-behaved performance versus scan angle at 27-32 GHz, and with very low cross-polarization levels. Note that the antennas with rotated-feeds configuration exhibits

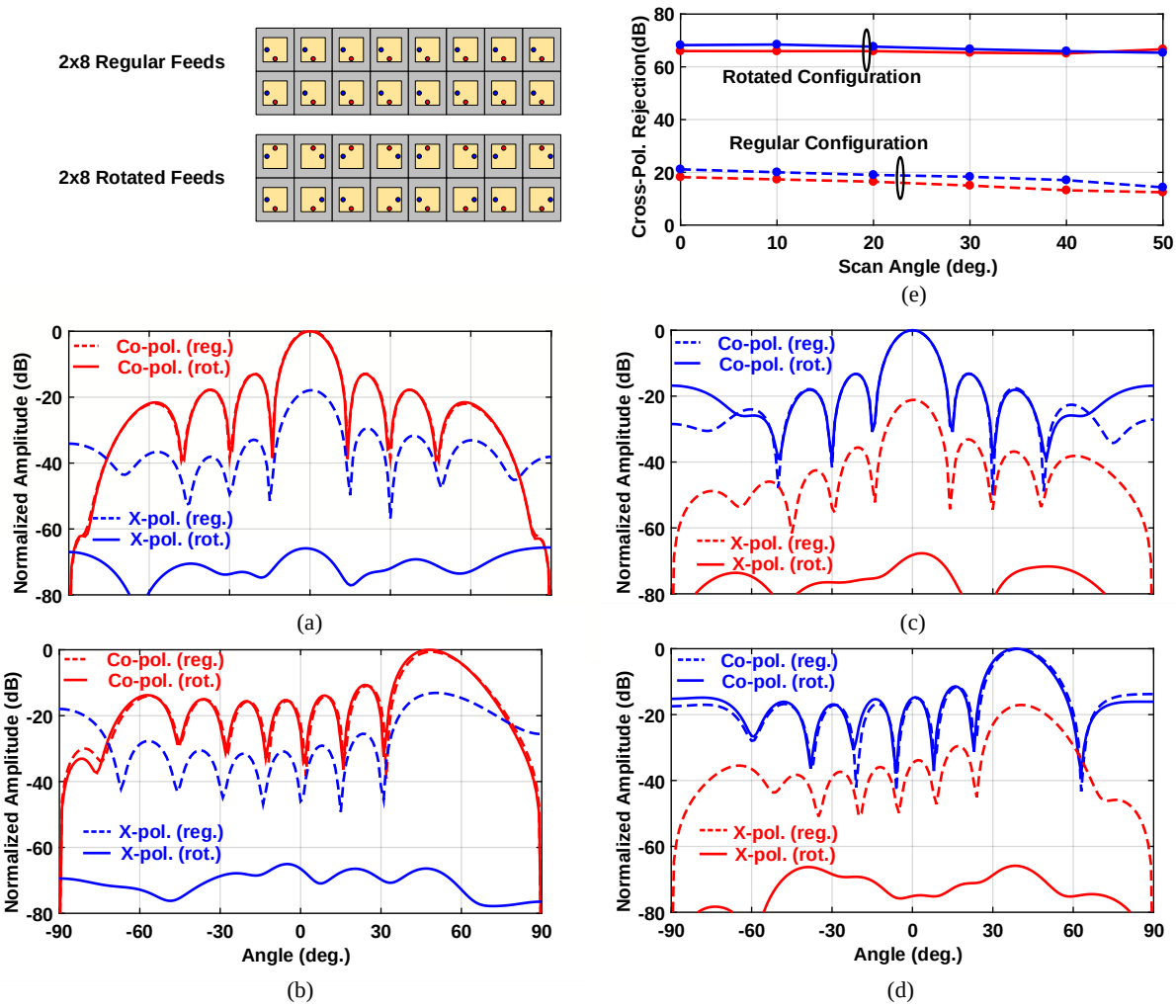

Figure 3.6: Simulated radiation patterns in azimuth for a 2×8 array with regular and mirrored feeds at 29 GHz. (a), (b) V-pol. at 0°, 50° scan and (c), (d) H-pol. at 0°, 50° scan and (e) X-pol. rejection over azimuth scan for V- and H-polarizations.

better reflection coefficients compared to the regular-feeds case especially in the E-plane [Fig. 3.7(c-d)]. The simulated cross-polarization levels of -60 dB represent the theoretical limits of this configuration under ideal conditions. In practice, cross-polarization levels are limited to $\simeq -30$ to -35 dB by other effects such as edge diffraction, amplitude and phase excitation errors and also by measurements imperfections such as small mechanical misalignment ($\pm1^\circ$) or reflections in the set-up.

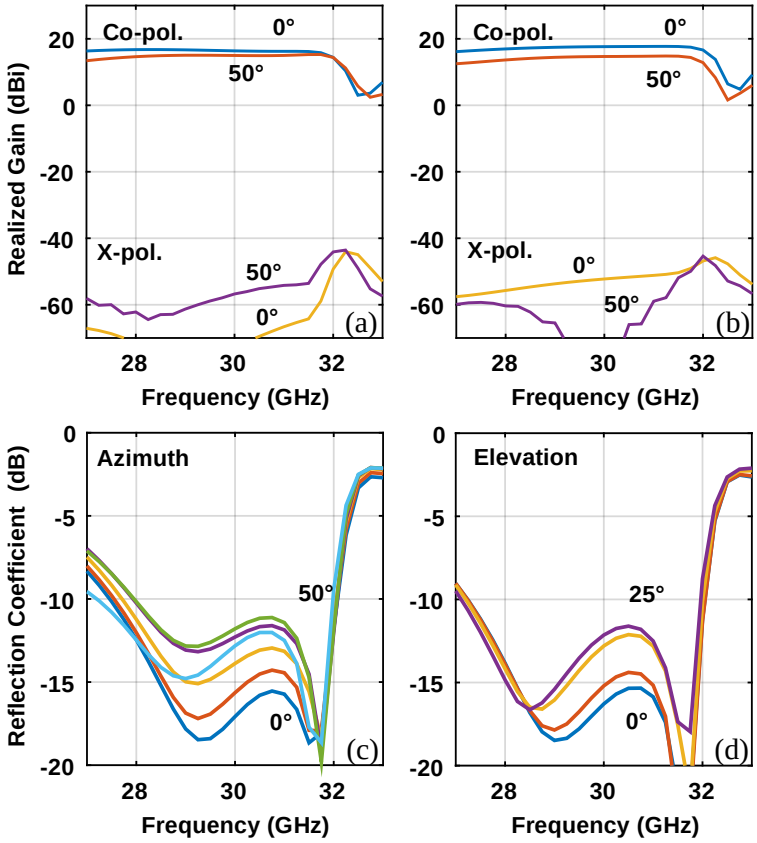

Figure 3.7: Simulated realized gain (Co. and X-pol.) versus frequency for the 2×8 array with rotated feeds: (a) V-pol. at 0°, 50° azimuth scan and (b) H-pol. 0°, 50° azimuth scan. Simulated active reflection coefficients for H-pol. under different scan angles in (c) azimuth (E-plane) and (d) elevation (H-plane).

3.3.3 Wilkinson Beamforming Network Design

Two 1:16 Wilkinson divider/combiner networks are used to feed the H- & V- beams. To maximize isolation, the feed networks are kept on separate layers. The feed network for H-beam is implemented in microstrip form and occupies M1-M2, whereas for V-beam the network is implemented in strip-line form and occupies M2-M3-M4 (Fig. 3.8). Both Wilkinson couplers exhibit an insertion loss <3.4 dB and port-to-port isolation >20 dB. Also, the cross-coupling between the microstrip and the strip-line Wilkinson couplers is <-50 dB. Fig. 3.9 presents the simulated results for the cascaded network from the array input to the chip common port. The simulated insertion loss in the TX-mode is 16-17 dB (12 dB division loss, 5-6 dB ohmic loss).

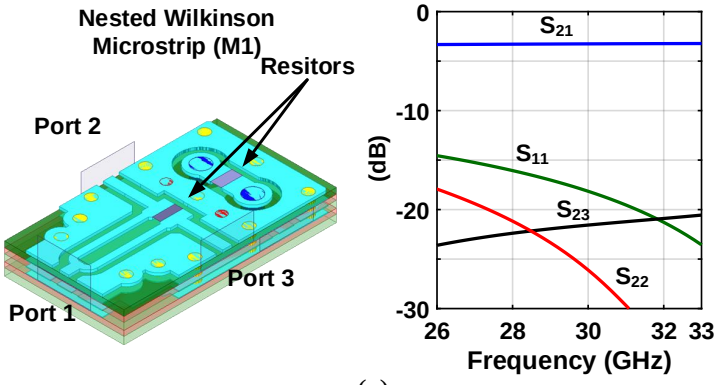

(a)

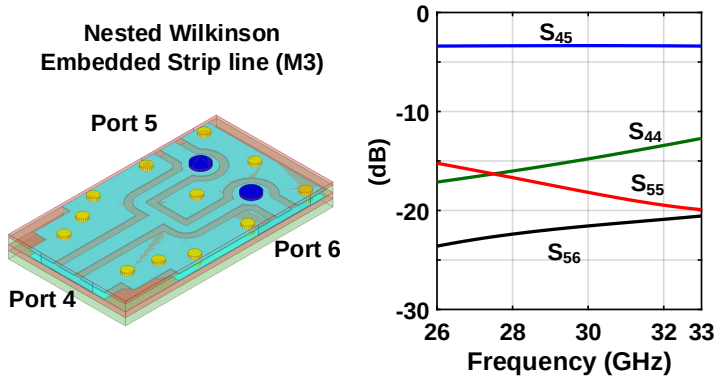

(b)

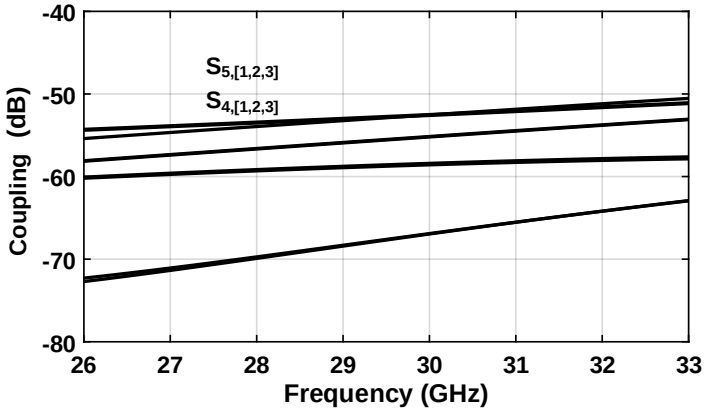

(c)

Figure 3.8: Simulated nested Wilkinsons: (a) microstrip line Wilkinson S-parameters, (b) strip-line Wilkinson S-parameters and (c) Inter-wilkinson coupling.

The cross-coupling levels from V to H is <-52 dB (isolation ≥ 35 dB).

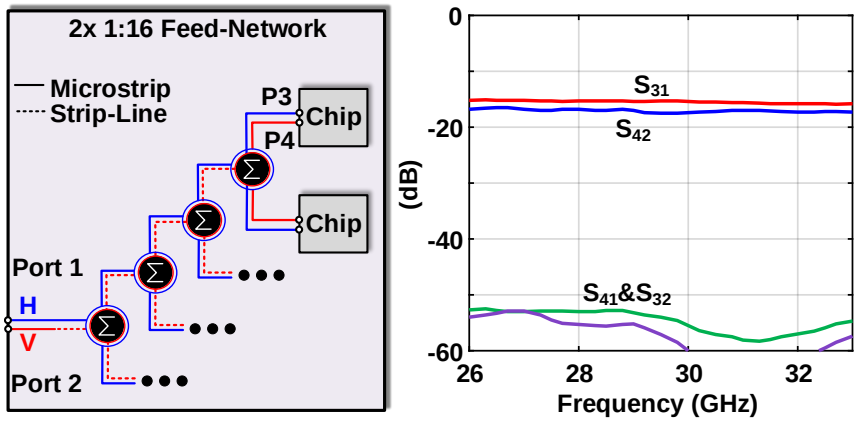

Figure 3.9: Simulated transmission and coupling coefficients for the H- and V- beamforming networks.

3.4 Measurements

3.4.1 Phased-Array Calibration, Frequency Response and EIRP

The phased-array (Fig. 3.10) was characterized in the far-field ($D = 1.9$ m $> 2D^2_{\max}/\lambda$) using a standard gain horn antenna which is aligned to either a horizontal or a vertical polarization. The channels were first characterized individually at their maximum gain and zero-setting phase state by taking over-the-air transmission measurements to the horn using a vector network analyzer. The results for the H-polarized channel are shown in Fig. 3.11. The 64 amplitude measurements are spread within mostly ± 2.5 dB with an rms value of 1.2 dB and 1.7 dB for the H- and-V-polarized elements respectively. The measured phases form two distinguishable clusters that are separated by 180° due to the effect of the antenna feed-rotation for the H-polarization. The V-polarized channel has two extra phase clusters due to having un-equal transmission lines interconnects between the chip and the antennas. The phase offsets are calibrated out using the channel phase shifters to within $\pm 11^\circ$, while the gain is left uncalibrated.

After the channel calibration is done, the broadside frequency response in the RX mode (Fig. 3.12a) was measured with all the channels at their maximum gain state. Both polarizations exhibit nearly the same frequency response with a 3-dB bandwidth of 28-32 GHz. Additionally,

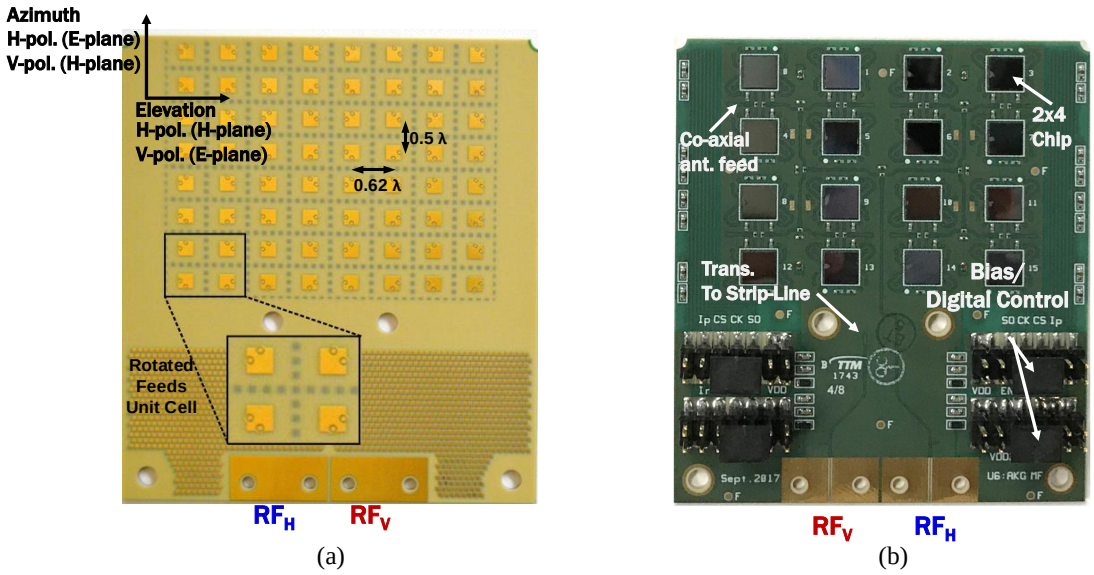

Figure 3.10: Dual-beam dual-polarized phased-array PCB: (a) Antenna-side view, and (b) chip-side view.

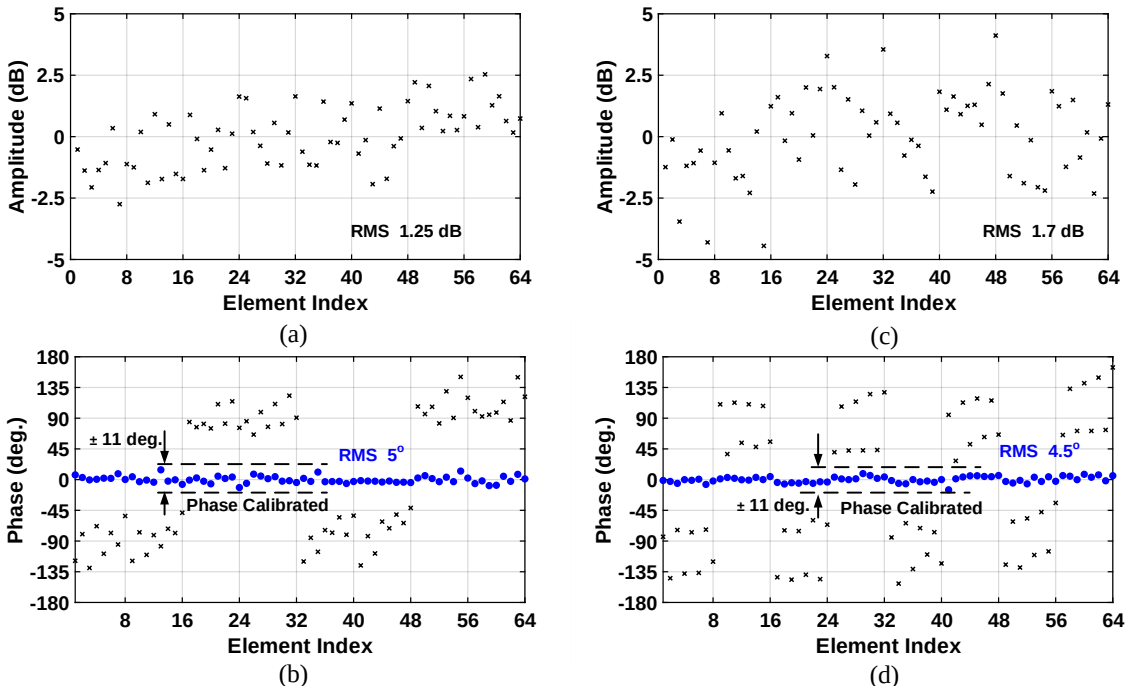

Figure 3.11: Measured normalized amplitude and phase of all 64 H-polarized elements (a, b) and 64 V-polarized elements (c, d) in the far-field at 29 GHz before and after calibration.

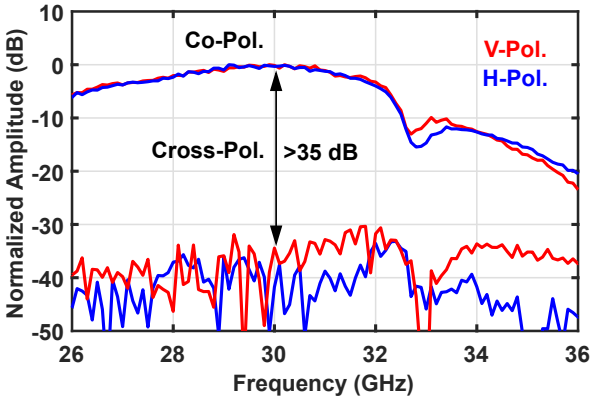

(a)

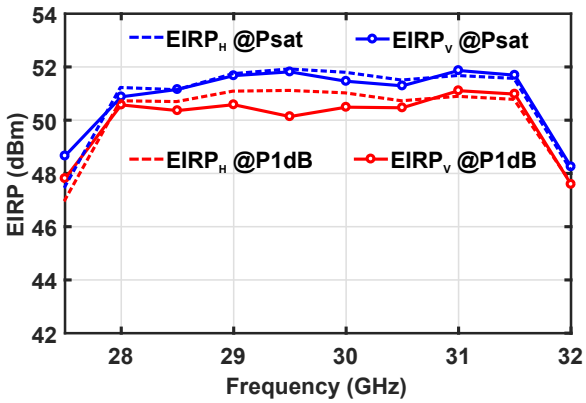

(b)

Figure 3.12: Measured (a) RX frequency response at broadside and (b) EIRP at broadside for vertical and horizontal polarizations.

the polarization purity is very high with both beams showing >35 dB of cross-polarization rejection at broadside.

The measured EIRP is 52 dBm at Psat, and 50-51 dBm at P1dB (Fig. 3.12b). This agrees well with simulations ($\text{EIRP}_{\text{P1dB}} = 20\log N + G_{\text{ant}} + P_{\text{element}} = 36 + 4.5 + 11 = 51.5$ dBm), and the difference could be due to additional antenna loss, mismatch and self-heating. A $G_{\text{ant}} = 4.5$ dB is used and is based on $D_{\text{ant}} = 5.5$ dB with 1 dB antenna loss. The 3-dB EIRP bandwidth extends from ~27.5 GHz to 32 GHz. Note that the dual-beam phased-array consumes 14-15 W at P1dB and Psat per beam (28-30 W when two beams are ON), and a fan was used behind the array to keep the PCB temperature at <55°C.

On the RX side, the measured dual-polarized dual-beam SiGe beamformer NF is 4.8 dB

with an IP1dB of -21 dBm (Table I) [8]. The phased-array system NF therefore becomes 5.3 dB at 29 GHz when the transmission-line loss between the antenna and chip (0.5 dB) is included. For a 100 MHz waveform, this translates into a total system noise of ~ -89 dBm and a dynamic range of $\sim$68 dB. The dynamic range can be improved with the use of gain control in the beamformer chip which improves its IP1dB to $-$ 11 dBm while keeping the NF to <10 dB [8].

3.4.2 Single-Beam Operation and Characterization

Fig. 3.13 present the measured azimuth and elevation patterns under uniform illumination for the vertical and horizontal polarizations, respectively. In single beam-mode operation, one beam is active at a time and the unused beam is shut off (no bias current applied). The array is capable of scanning up to $\pm 50^{\circ}$ in azimuth and up $\pm 25^{\circ}$ in elevation without grating lobes (see Fig. 3.10 for the definition of azimuth and elevation planes). For the horizontally-polarized beam, the scanned pattern envelope (scan loss) follows a $\cos^{1.2}\theta$ profile with a maximum scan drop of 2.9 dB at $\pm 50^{\circ}$. In the elevation plane, the beam can scan up to $\pm 30^{\circ}$ with less than 0.7 dB drop and follows a $\cos^{1.0}\theta$ profile. The vertically-polarized beam follows a $\cos^{1.0}\theta$ scan-loss profile in azimuth with a maximum scan drop of 2 dB at 50°. In elevation, the beam can scan up to $\pm 25^{\circ}$ with less than 1.3 dB drop and up to $\pm 30^{\circ}$ with 3.9 dB drop. The scan loss includes the antenna impedance mismatch, and these results show that the antenna is well matched up to the scan range limit.

At broadside, the array pattern has a 3-dB beam-width of 12.5° in azimuth and a 3-dB beam-width of 10.5° in elevation for the V- and H- polarizations. The pattern is narrower in elevation due to the antenna placement on a rectangular grid (0.5λ in azimuth and 0.62λ in elevation). The array patterns are virtually the same for TX/RX modes. The side lobes are generally <-12 dB and can be reduced to <-18 dB with the application of raised-cosine amplitude taper. The radiation-patterns are also shown at different frequencies in Fig. 3.14. Channel calibration was carried out at only 29 GHz and this is sufficient to produce near-ideal

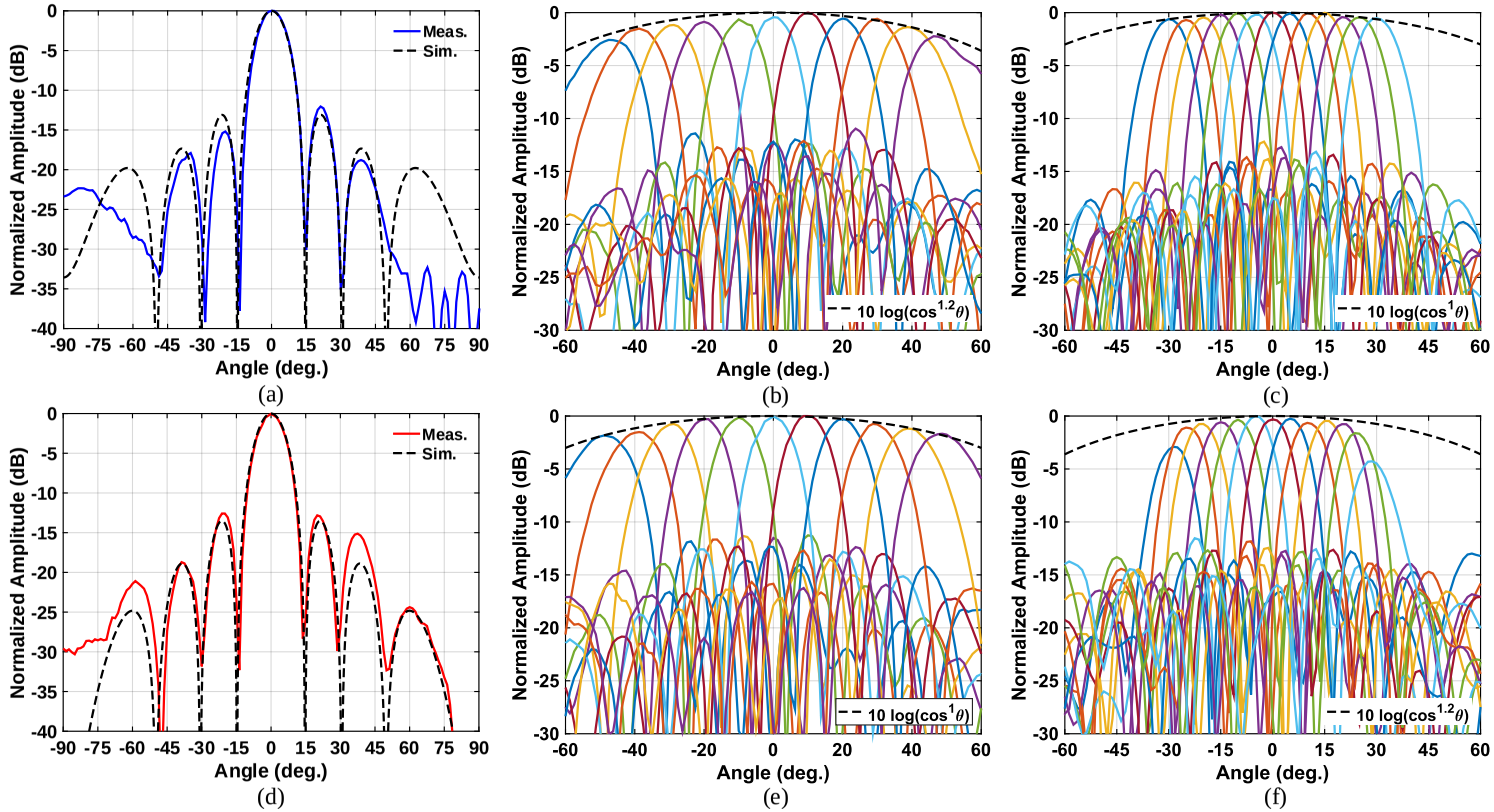

Figure 3.13: Measured beams at 29 GHz. Horizontally-polarized beams: (a) broadside in azimuth (E-plane), (b) azimuth-scanned (E-plane) (c) elevation-scanned (H-plane). Vertically-polarized beams: (d) broadside in azimuth (H-plane), (e) azimuth-scanned (H-plane) (f) elevation-scanned (E-plane).

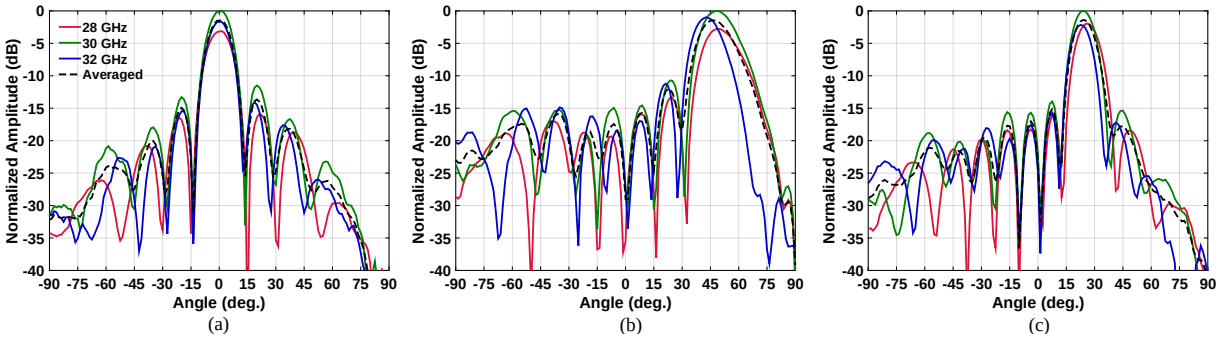

Figure 3.14: Measured beam squint at 28-32 GHz for: (a) V-beam in azimuth, (b) V-beam scanned to 50° in azimuth and (c) H-beam scanned to 25° in elevation.

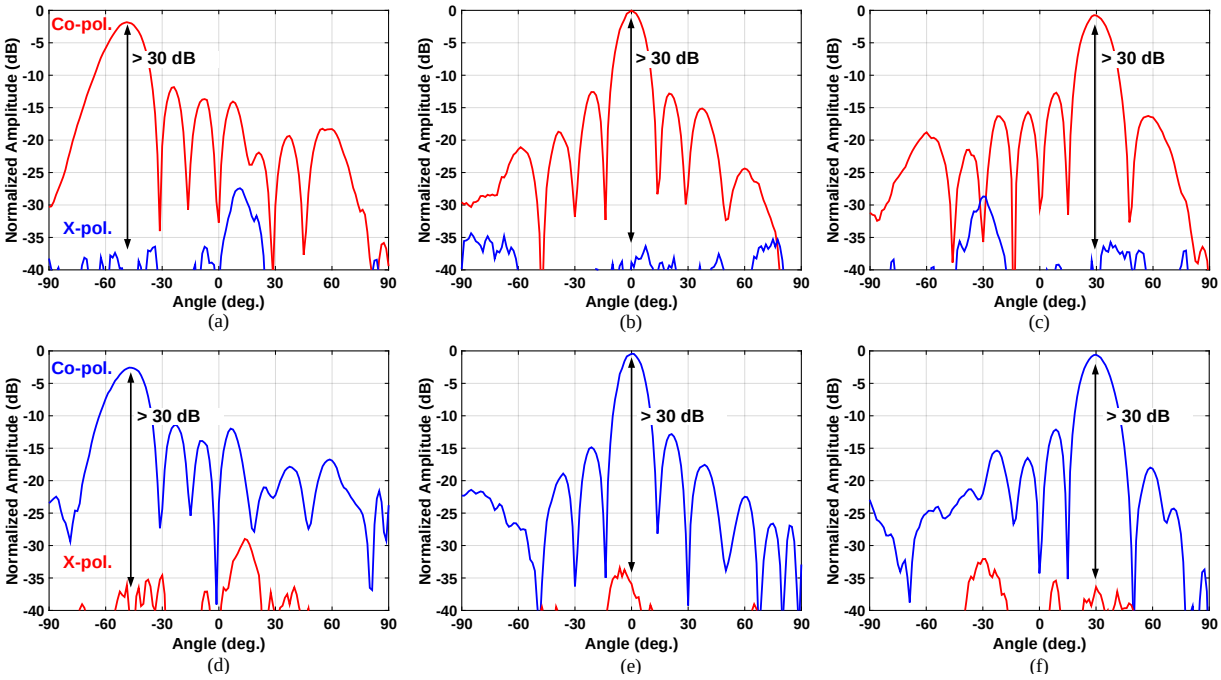

Figure 3.15: Measured co-polarized and cross-polarized patterns at 29 GHz in azimuth: (a,b,c) V-Beam scanned to −50°, 0° and 30° and (d,e,f) H-Beam scanned to −50°, 0° and 30°.

beam across the operating bandwidth. However, as expected, the beam pointing angle changes slightly due the use of a phase shifter with constant phase shift versus frequency (as opposed to true-time delay at each element). The amount of beam squint at 28-32 GHz is <2.5°-6.25° at the maximum scan angle in elevation and azimuth, respectively, which is acceptable knowing that the beamwidth is ∼12.5°-17° at the maximum scan angles.

Fig. 3.15 presents the measured co- and cross-polarized patterns for the vertically and

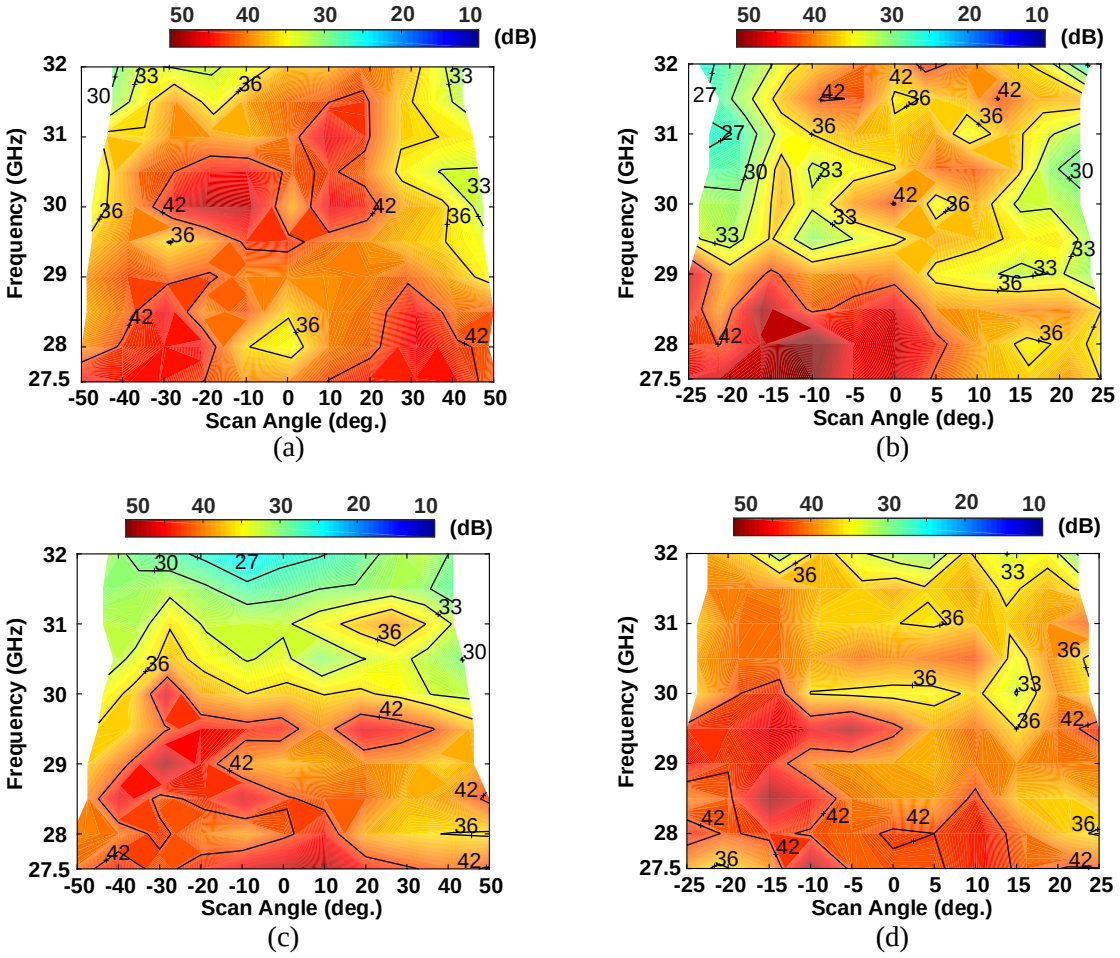

Figure 3.16: Measured cross-pol. rejection versus frequency and scan angle: (a,b) V-beam in azimuth and elevation and (c,d) H-beam in azimuth and elevation.

horizontally polarized beams scanned in azimuth, and with >35 dB cross-polarization rejection in the beam pointing direction. A color-map showing the main-beam cross-polarization rejection versus frequency and scan angle is presented in Fig. 3.16 for the azimuth and elevation scans. As can be seen, the cross-polarization rejection of each beam remains >30 dB over almost the entire bandwidth and scan angles.

3.4.3 Dual-Beam Operation and Characterization

The phased-array was also tested under dual-beam operation with both beams activated and pointing to similar and different angles. This test includes cross-polarization contributions due to antenna coupling as well as contribution from all coupling interactions between the two beams on the chip and on the PCB, and includes any coupling between the V and H Wilkinson beamforming networks.

An example of a dual-beam experiment is presented in Fig. 3.17(a,b) where both beams are scanned to the same angle in azimuth $\theta_H = \theta_V = 0^\circ$, and $\theta_H = \theta_V = 45^\circ$. Both beams have near-ideal patterns, and with active cross-pol. rejection $\geq$28 dB for both vertically and horizontally-polarized beams. Another example is shown in Fig. 3.17(c) where the V- and H-beams are scanned to different angles in azimuth ($\theta_V = 30^\circ, \theta_H = -30^\circ$). The patterns are very close to theoretical expectation and exhibit cross-polarization levels <$-$30 dB. Fig. 3.18 presents the measured cross-polarization rejection for the dual-beam case versus scan angle in the azimuth plane, and it remains >30 dB at nearly all scan angles, except broadside for the H-beam. The lower H-beam cross polarization rejection relative to that of the V-beam near broadside could be due to a constructive superposition of H-beam antenna cross-polarization radiation component (~ -34 dB) and H-to-V coupling at the chip and Wilkinson beamformer (~ -35 dB). Also mechanical misalignment could be a contributing factor, considering that a small misalignment of $\pm 1^\circ$ results in an apparent cross-polarization level of -35 dB. Overall, this result suggests that the total H-V coupling in the array PCB and chip is better than -29 dB.

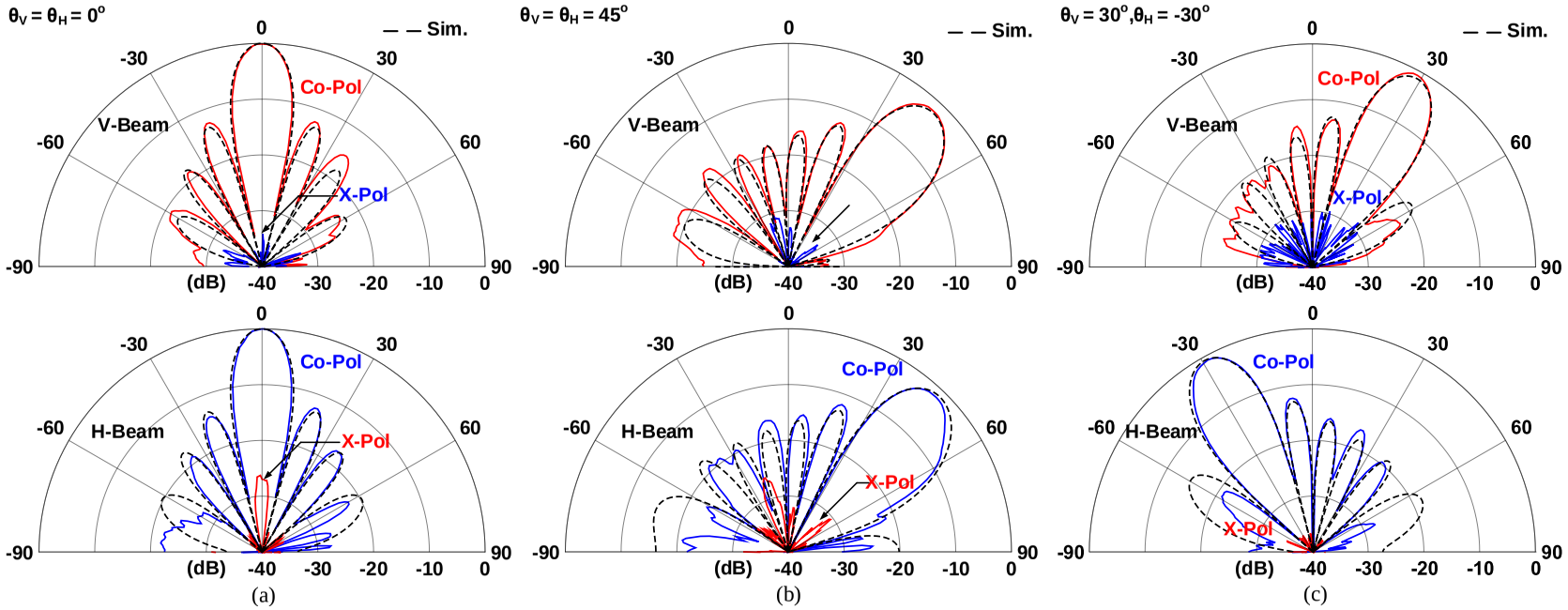

Figure 3.17: Measured simultaneously transmitted beams in the azimuth plane at 29 GHz: (a) $\theta_V = \theta_H = 0^\circ$, (b) $\theta_V = \theta_H = 45^\circ$ and (c) $\theta_V = 30^\circ, \theta_H = -30^\circ$.

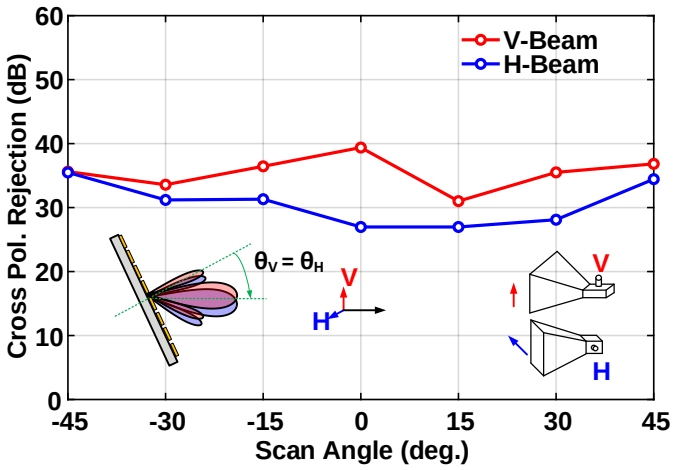

Figure 3.18: Measured cross-polarization rejection with simultaneously transmitted beams ($\theta_V = \theta_H$) versus scan angle in azimuth at 29 GHz.

3.5 Single- and Dual-Beam Communication-Link Measurements

The dual-polarized dual-beam phased-array is tested with complex modulated signals using the set-up shown in Fig. 3.19. On the TX-side, two independent data streams of 16-QAM and 64-QAM formats are simultaneously generated at an IF of 7 GHz using two channels of a Keysight M8195 arbitrary waveform generator (AWG). The modulated waveforms are up-converted to 29 GHz using a 22 GHz LO, amplified and fed into the phased-array V- and H-co-axial ports. The power amplifiers are operated at a fixed output power level of 16 dBm which corresponds to a 9 dB back-off level for high linearity. The input power level to the array, and hence the transmit EIRP, is controlled by adjusting variable attenuators after the amplifiers. This ensures that any EVM degradation is due to non-linearity contributions of the array itself and not the amplifier and mixers in the transmit chain. On the RX-side, the horn is linearly polarized and is aligned vertically when receiving from the V-beam, and horizontally when receiving from the H-beam, of the array. The signal received by the horn is demodulated using the Keysight DSOZ632A sampling scope with a real-time bandwidth of 63 GHz. The input power to the array

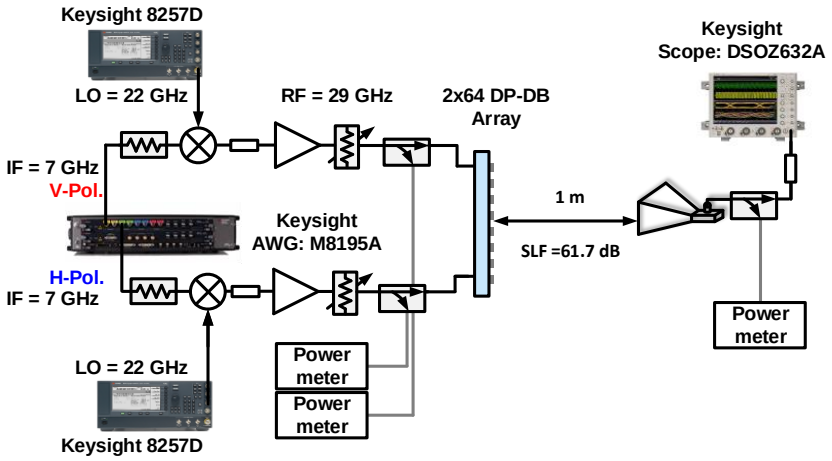

(a)

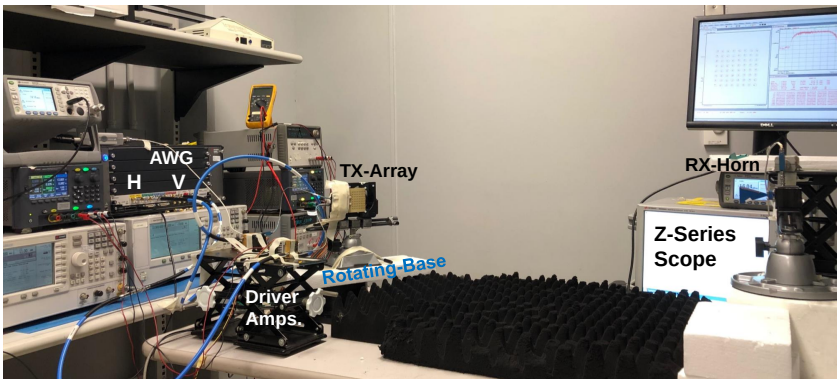

(b)

Figure 3.19: Measurement setup for array EVM measurements: (a) block-diagram and (b) photograph.

and the received power at the horn are monitored using couplers connected to power meters.

Fig. 3.20a presents the measured EVM for different transmitted EIRP levels using 64-QAM signals with 800 Mbaud symbol rate and with a root-raised cosine pulse filter with $\alpha = 0.35$ and a peak to average power ratio (PAPR) of 7.7 dB. All reported EVM values are referenced to the peak of the constellation (EVM_{max}) [28], and it can be translated to EVM_{rms} using a multiplicative factor of 1.53 for 64-QAM. When only one AWG channel is active (H or V), referred to as single-beam operation, the EVM for V- and H-polarized beams is 1.5% in deep backoff and is limited by the AWG wideband noise and the LO and sampling scope phase noise (more details on a similar measurement have been presented in [6]). The EVM is <3.26%

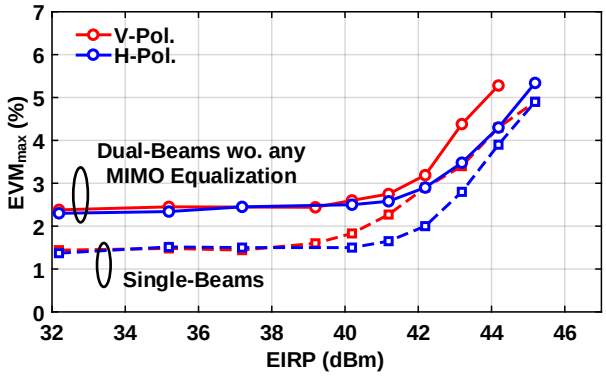

(a)

EIRP	32 dBm	42 dBm	44-45 dBm
V-pol. Constellation	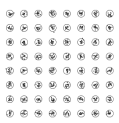	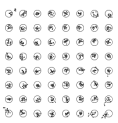	
V-pol. EVM	2.3%	3.1%	5.2%
H-pol. Constellation	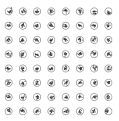		
H-pol. EVM	2.1%	2.9%	5.3%

(b)

Figure 3.20: (a) Measured EVM versus EIRP levels using 800-Mbaud 64-QAM, (b) constellations in dual-beam operation.

(EVM_{rms} =5%, −26 dB) up to a transmit EIRP of 43-44 dBm corresponding to 6-7 dB back-off level from the array EIRP at P1dB.

When both V and H-polarizations are transmitting data simultaneously, referred to as dual-beam operation, and keeping EIRP_V=EIRP_H and the pointing angle to broadside $\theta_V = \theta_H = 0$, the lowest measured EVM degrades to 2.2% (EVM_{rms}=3.3%) due to the cross-polar interference between both data streams at the ~ -30 dB level. Fig. 3.20b presents example constellations in dual-beam operation. At an EIRP of 32 dBm, the EVM is limited mostly by contribution from cross-polarization ($\sim$ 1.9%) and SNDR ($\sim$ 1.4%). Beyond an EIRP of 42 dBm, the power amplifier nonlinearities start to dominate the overall EVM. At an EIRP of 45 dBm, the effect of

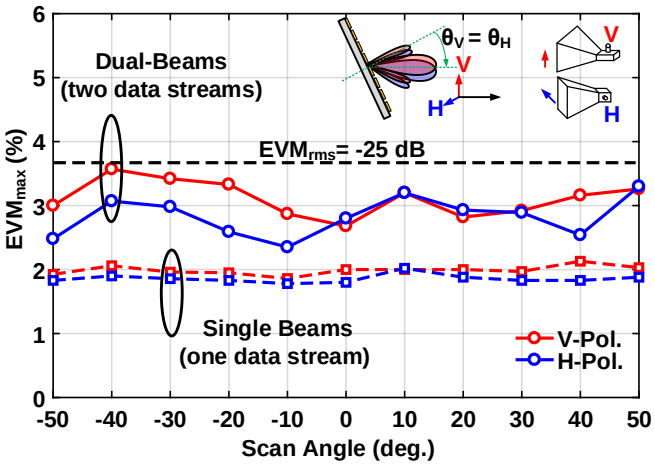

Figure 3.21: Measured EVM versus scan angle in azimuth using 800-Mbaud 64-QAM waveform at an EIRP of 41 dBm per polarization.

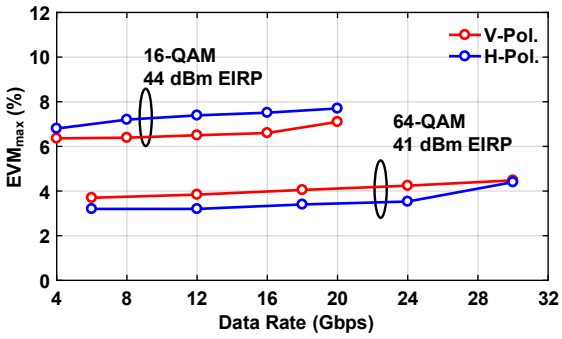

(a)

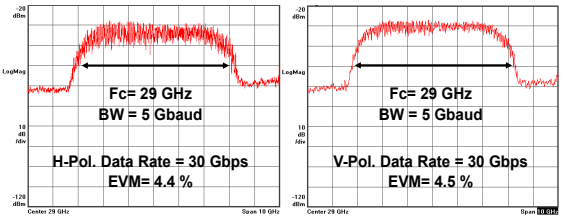

(c)

Modulation EIRP	16-QAM 44 dBm		
Data-Rate per pol.	4 Gbps	12 Gbps	20 Gbps
V-pol. Constellation		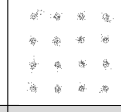	
V-pol. EVM	6.4%	6.5%	7.1%
H-pol. Constellation	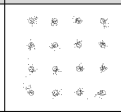		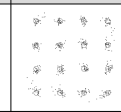
H-pol. EVM	6.7%	7.4%	7.7%
Modulation EIRP	64-QAM 41 dBm		
Data-Rate per pol.	6 Gbps	18 Gbps	30 Gbps
V-pol. Constellation		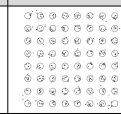	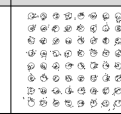
V-pol. EVM	3.7%	4.0%	4.5%
H-pol. Constellation		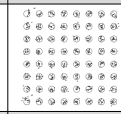	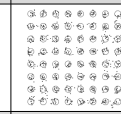
H-pol. EVM	3.3%	3.4%	4.4%

(b)

Figure 3.22: (a) Measured EVM versus data-rate using 16-/64-QAM waveforms and dual-beam operation ($\theta_V = \theta_H = 0°$), (b) measured constellations and (c) measured spectra at maximum data rate using 64-QAM waveform.

PA compression can be clearly seen and the EVM_{max} is 5% (-22.4 dB).

The EVM was also measured over scan angle in azimuth using 800 Mbaud 64-QAM

waveforms, at an average EIRP of 40.5-41 dBm (Fig. 3.21). In single-beam operation, the EVM is nearly constant at 2% over $\pm 50^\circ$ scan range for both horizontally- and vertically- polarized beams. In dual-beam operation ($\theta_V = \theta_H$), the EVM increases by 0.5-1.5% and shows more variation over scan angle depending on the average cross-polarization levels ($\sim$28-40 dB). Nevertheless, the overall EVM remains below 3.6% (-25.2 dB) for both polarizations over the entire scan range.

Fig. 3.22a and Fig. 3.22b present the measured EVM and constellations for increasing data rates using 16- and 64-QAM waveforms in dual-beam operation, and with both beams pointing to broadside ($\theta_V = \theta_H = 0^\circ$). A data rate of up to 2×30 Gbps can be supported in 64-QAM at average EIRP of 41 dBm per polarization with an EVM less than 4.5% (-23.3 dB). The array has 4.5 GHz bandwidth and can support a 30 Gbps 64 QAM signal. The measured spectra at the peak data rate are shown in Fig. 3.22c. Also, since a 16-QAM waveform has a lower PAPR of 6.6 dB, a link data rate up to 2×20 Gbps at an EIRP of 44 dBm is achieved with an EVM less than 8% (-18.3 dB). Such a signal also requires a 4-5 GHz bandwidth from the array. Table 3.2 summarizes the performance of the 8×8 dual-polarized array. A comparison with other state-of-the-art 28 GHz dual-polarized phased-arrays is also shown.

3.6 Conclusion

This work presents a 2×64-element 28-32 GHz dual-polarized dual-beam phased array for 5G applications. The array incorporates a shared aperture for both vertically- and horizntally-polarized beams while maintaining high-beam isolation and cross-polarization suppression over scan. An 8-channel SiGe 2×2 quad-beamformer chip is used together with feed-rotation on the 2×2 antenna cell for improved cross-polarization performance. Also, a dual-Wilkinson beamforming network is used in the PCB to obtain two simultaneous beams. Dual-beam operation and over-the-air (OTA) link measurements were demonstrated achieving record-setting data rates

Table 3.2: Comparison with State-of -the-Art 28 GHz Dual-Polarized Phased-Arrays

		This work		IBM '17 [9]	Qualcomm '18 [11,12]	Tokyo Tech. '19 [8]			UCSD '18 [3]	
IC process		**0.18 um SiGe BiCMOS**		0.13 um SiGe BiCMOS	28 nm LP-RF CMOS	65 nm CMOS			0.18 um SiGe BiCMOS	
Frequency (GHz)		**28-32**		27.2-28.7	26.5-29.5	26.5-29.5			28-32	
Number of antenna elements		**(8x8) TRX**		(8x8) TRX	(8x32) TRX	(4x8) TRX			(2x2) TRX	
Phase step (deg)		**5.6**		4.9	45	11.2			5.6	
RX Chip NF (dB)		**4.8**		6	4.4-4.7	4.2			4.8	
RX IP1dB (dBm)		**-21**		-22.5	-	-30#			**-21**	
Pdc RX / ch. (mW)		**163**		206Δ	42Δ	113Δ			150	
Pdc TX / ch. (mW)		**228 @ P1dB**		319Δ@ Psat	122Δ @ P1dB	253Δ @ 11.3 dBm / ch.			220 @ P1dB	
EIRP / pol. (dBm)		**52 @ Psat**		54 @ Psat	64 @ Psat	45.6 @ Psat			26.5 @ P1dB	
Scan Range Az. ±(V/H) (deg)		**50/50**		50/50	55/55	50/50			-	
Cross-Pol. Rejection over scan Range Az. (dB)		**≥ 28**		-	-	-			27 at broadside	
OTA 2x2 MIMO at broadside	**Modulation**	**16-QAM**	**64-QAM**	-	-	**16-QAM**	**64-QAM**	**256-QAM**	**16-QAM**	**64-QAM**
	Data-Rate (Gbps)	**2x20**	**2x30**			**2x1.6***	**2x2.4***	**2x0.8***	**2x12**	**2x12**
	TX-EIRP/pol. (dBm)	**44**	**41**			**-**	**-**	**-**	**19.9**	**18.5**
	EVM (dB)	**≤ -19.7**	**≤ -23**			**≤ -26.2**	**≤ -26.2**	**≤ -31.1**	**≤ -19.4**	**≤ -22.3**
OTA 2x2 MIMO data rate over scan		**2x4.8 Gbps 64-QAM over ±50 Az. Scan EIRP = 41 dBm/pol. EVM ≤ -25.2 dB**		-	-	-			-	

*: Done using a 4x4 module, # :estimated from Pout-Pin curve, Δ :based on single channel measurement not array (no thermal effects)

up to 40 Gbps and 60 Gbps using 16- and 64-QAM waveforms at broadside. Link performance with both beams scanned off-broadside to the same direction was also demonstrated achieving a data rate of 9.6 Gbps using 64-QAM waveform with an EVM≤ -25 dB over $\pm 50^{\circ}$ scan range. The design can be scaled to larger arrays such as 256-elements with no change in the antenna or Wilkinson beamforming networks for increased coverage.

3.7 Acknowledgement

This work was supported in part by the U.S. Department of Commerce, National Institute of Standards and Technology, and in part by Facebook

Chapter 3, in part, is a reprint of the material as it appears in IEEE MTTS Int. Microw. Symp. (IMS), 2019. A. Nafe, M. Sayginer, K. Kibaroglu, and G. M. Rebeiz. The dissertation author was the primary investigator and author of this paper.

Chapter 3 is also mostly a reprint of the material as appears in IEEE Transactions on Microwave Theory and Techniques, 2020. A. Nafe, M. Sayginer, K. Kibaroglu, and G. M. Rebeiz. The dissertation author was the primary investigator and author of this paper.

Chapter 4

In-Situ Self-Test and Self-Calibration of 5G Multi-Beam Phased-Arrays Leveraging Quadrant-Level Antenna Mutual Coupling

This chapter presents an in-situ self-test and self-calibration technique and its application to 5G phased arrays. The built-in self-test (BIST) procedure, labeled Quad-BIST, enables the relative channel calibration, channel gain/phase characterization and failure detection of 5G phased-arrays. Quad-BIST relies on mutual coupling between antennas in neighboring arrays arranged in Quad-fashion to extract the calibration coefficients and perform channel characterization. The calibration technique was successfully applied to 5G 28 GHz arrays with 4x4 and 8x8 elements in each quadrant. The results show that Quad-BIST predicts the channel states (gain and phase control) with rms errors of 0.2 dB/2° and 0.4 dB/2.5° for the 4x4 and 8x8 quadrants, respectively. The relative channel ratios are found to be within rms errors of 0.8 dB/7.5° from their far-field counter-parts for both cases. Experimental results also show that near-ideal uniform-illumination patterns are attained using the quadrant-level calibration for both arrays, and with low-side lobe operation (<-20 dB over scan). The technique is all-electronic,

requires neither moving parts nor a far-field range, can be applied for initial calibration as well as for re-calibration in the field (as a result of aging, environmental changes, etc.), and is well suited for 5G MIMO base-station systems. To our knowledge, this work presents the first demonstration and detailed analysis of in-situ calibration for mm-Wave 5G phased arrays.

4.1 Introduction

Recently, there has been surging interest in millimeter-wave phased arrays due to their role in the upcoming 5G new radio (5G NR) standard. It is expected that 5G base-stations will deploy massive multiple-input multiple-output (MIMO) phased-array systems supporting multiple directional beams to increase the data rate and network capacity. The holy grail from a communication theory perspective is to provide a complete TX/RX chain with digitization (ADC) for each antenna with complete beam-forming control in the digital domain. However, at mm-Waves, this approach is not practical due several constrains of power, cost, and physical antenna spacing. In practice, each antenna is connected to a transmit/receive radio with a digital receiver at the array level (a transceiver and ADC/DAC for every 4x4 sub-array or larger) with analog beamforming (RF, IF or LO) occurring within each sub-array. Such hybrid (analog/digital) beamforming configuration with four sub-arrays arranged in quadrants is illustrated in Fig. 4.1a. Each quadrant array can form its own beam that can point to different users and directions. Also, data-streams from different sub-arrays can be combined, in the digital domain, for different forms of MIMO processing. Over the past few years, several 5G phased arrays have been developed with sizes ranging from 16 (4×4) to 64 (8×8) elements for the 28, 39 and 60 GHz bands [5, 6, 10–12, 14, 15, 29–31]

A main cost point for mm-Wave phased arrays is testing and calibration. For proper array operation, each channel is measured and the relative channel offsets need to be determined and corrected so as to accurately set the radiated beam properties (pointing angle, side-lobe level,

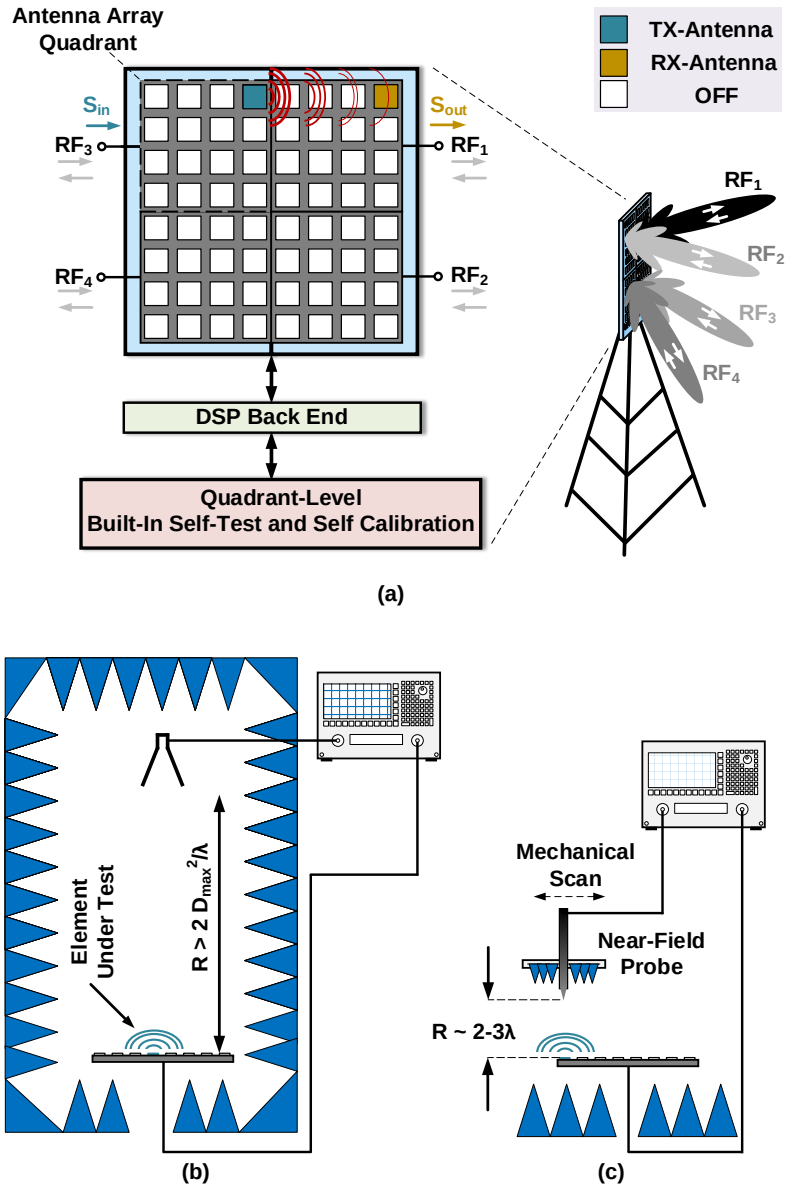

Figure 4.1: (a) Simplified diagram of a 5G multi-beam transmit/receive phased array with in-situ self-test and self-calibration capabilities leveraging array-to-array antenna-coupling. Conventional ex-situ phased array testing and calibration in: (b) far-field range and (c) near-field scanning range.

null placement, etc.). This process is not only required at production time (initial-calibration) but also needs to be done periodically to account for element drift due to environmental effects. Conventional array calibration is mainly carried out using a far-field range (Fig. 4.1b) or a near-field scanner (Fig. 4.1c) [32–36]. Both methods suffer from requiring complex laboratory set-ups and are not practical once the array is deployed.

It is, therefore, of interest to develop in-situ testing and calibration methods that can be periodically applied for fielded arrays. In-situ built-in-self-test (BIST) methods on the chip level are possible and have been the topic of several recent papers [37–43]. These methods have been limited to single-chip demonstrations and not on the array level. Although on-chip BIST is helpful in characterizing the electronic channel properties, it cannot capture the full channel response from the array feed point up to the antenna air-interface, and hence does not reflect the actual over-the-air (OTA) performance.

An important goal for in-situ calibration (also known as BIST) is to capture the full array-response up to the antenna air-interface. This kind of calibration can be achieved with the use of antenna mutual coupling and was originally introduced by [7,8]. In previous work, these arrays were part of a discrete T/R module-based radar system which had the capability of transmitting on one element and receiving on all of its direct neighbors. This design typically necessitates couplers after every electronic channel (between the T/R module and antenna) and a dedicated Wilkinson beamformer for the sampling path. Also, every element needs to be turned-on in Tx-mode singly, while the neighboring elements turned-on in Rx mode, a feature which is not possible using single beamformer chips with 8 or 16 TX/RX channels on the same chip.

In this work, the mutual-coupling concept is utilized for calibration of mm-Wave 5G antenna arrays. A theoretical and experimental framework show that by using 4 transmit/receive (TRX) sub-arrays as quadrants (Quads), each array can be calibrated in the TX and RX mode by using its direct neighbors in the RX or TX mode, respectively. This technique can be applied for in-situ phased-array calibration, channel monitoring and fault-detection. The technique is applicable to RF, LO and IF beamforming architectures, operating in a hybrid-phased-array, and with a summer/beamformer (active or passive) at the RF or IF level. A single RF or IF port is required for every quadrant.

This chapter is an expanded version of [44] and provides additional details, measurements,

performance and limitation analysis. The organization of this chapter is as follows. In section 4.2, the effect of excitation errors on setting the array radiation beam properties is discussed. Section 4.3 presents the calibration methodology, antenna coupling studies. In section 4.4, detailed quadrant-level near-field coupling signal and noise levels are analyzed, and the corresponding dynamic range is presented. Section 4.5 includes implementation details, finite isolation limitations and mitigation approaches, and a detailed characterization of $4 \times [4 \times 4]$ and $4 \times [8 \times 8]$ 5G arrays. A discussion of calibration accuracy and required number of measurements is presented in section 4.6. Finally, section 4.7 summarizes and concludes this chapter.

4.2 Array Excitation Errors and Beam-Setting Accuracy

Since the array radiation pattern is essentially a Fourier transform of its aperture distribution (the antenna current coefficients), therefore any error in the aperture excitation coefficients will cause a deviation from the ideal pattern. Excitation errors can occur due to imprecise knowledge of the different channels or due to discretization (amplitude and phase steps). Depending on the nature of the errors, random or spatially correlated, the far-field patterns will be affected differently, the spatially correlated errors being more serious as they can give rise to distinct side lobes [45]. Examples of spatially correlated errors include errors on a sub-array level, for instance due to an imbalance in the Wilkinson branch that feeds a sub-array, or due to a particular chip being offset in gain which contains many neighboring channels. Fully random errors are not spatially correlated, for example, the errors occurring independently in the electronic channel level due to the phase shifter setting accuracies (rms phase and gain errors of a phase shifter) and the gain setting accuracies of a VGA (rms gain error of VGA steps). The effect of random errors have been studied extensively [3, 45–47].

The process of calibrating the array refers to the different channel responses in their various states (phase/gain settings) over frequency and temperature. Under ideal calibration,

all the array channels are perfectly known with high precision and can be set to any desired excitation with residual errors given by the channel rms errors (phase shifter, VGA). In practice, the calibration process itself will have some imprecision, which will add to the overall uncertainty of the excitation coefficients. It is however assumed that these calibration errors have zero mean (containing no systematic bias) leaving only residual random errors on the aperture.

The impact of random errors on the array patterns can be visualized with the aid of Monte-Carlo simulations. The channel amplitude δ_n and phase α_n errors are drawn from a Gaussian distribution, with a standard deviation σ_a and σ_p, respectively. The Gaussian distribution standard deviation is basically the root-mean square value of the error $\sigma_a = \sqrt{E[\delta^2]}$ and $\sigma_p = \sqrt{E[\phi^2]}$. The resulting pattern from a given excitation error is computed from the array factor with the addition of errors (δ_n and α_n), and with an element factor taken as $\cos(\theta)$.

$$|P(\theta,\phi)| = |\sum_{k=1}^{n} I_k(1+\delta_k)e^{j\alpha_k+\Delta}e^{j\vec{k}.\vec{r_k}+j\Delta_k}|\cos(\theta) \tag{4.1}$$

Fig. 4.2 presents simulated patterns of an 8×8 array on a half-wavelength square grid for different rms errors and excitations (uniform and 10-dB raised-cosine taper). Each rms error value is run 100 times, and the resulting patterns are shown. It is observed that errors impact the side-lobes more than the directivity and 3-dB beamwidth. In particular, the 3-dB beamwidth is barely changed $< \pm 0.25^\circ$ even for the highest rms error of 2 dB/20°. The directivity is also a forgiving function of the errors, and in the worst case, the directivity drops by <0.7 dB for 2 dB/20°, <0.2 dB for 1 dB/10° errors, and <0.05 dB for 0.5 dB/5° rms errors. However, the peak side lobes can change significantly for a 2 dB/ 20° error from -13 dB to -10.5 dB under uniform illumination and from -23 dB to -15 dB under tapered illumination. To ensure side-lobes lower than -20 dB, the residual and random calibration errors should be better than 1 dB/10° for an 8×8 array.

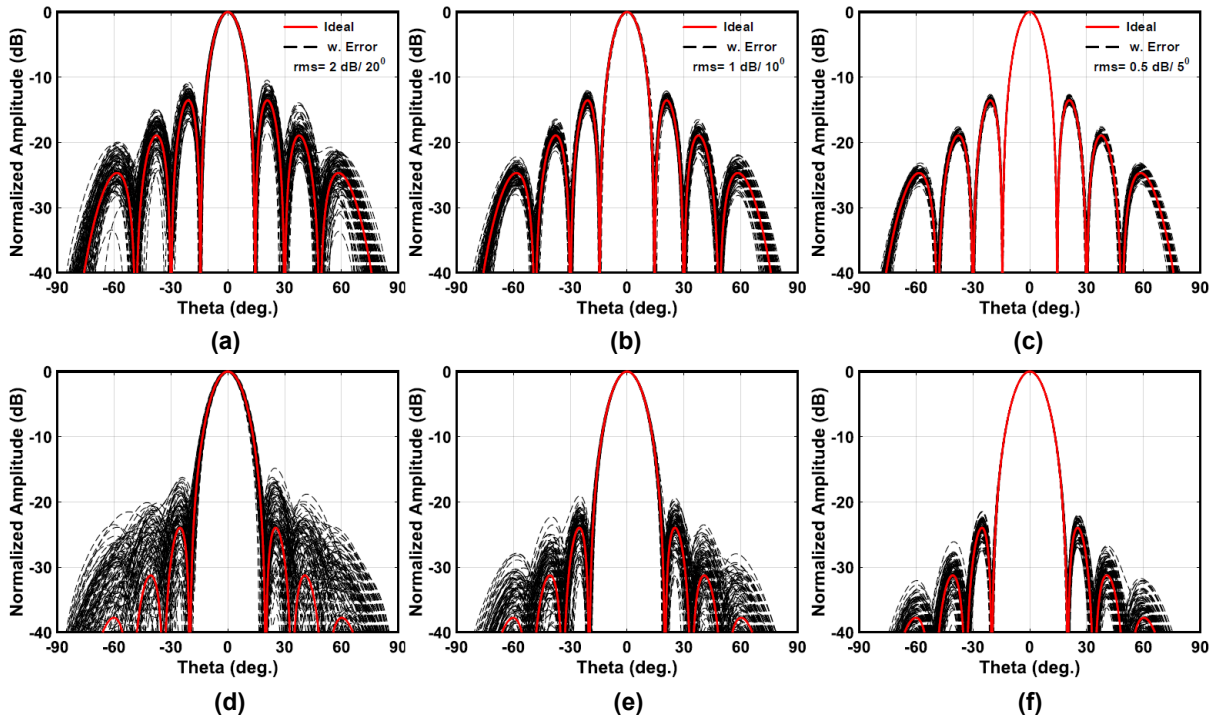

Figure 4.2: Simulated 8×8 array amplitude and phase residual-calibration errors effects on patterns under uniform and 10 dB raised-cosine taper illuminations: (a,d) 2 dB/ 20°, (b,e) 1 dB/ 10°, and (c,f) 0.5 dB/ 5°.

4.3 Calibration Methodology

The channel response in the transmit (S_{21}) and receive mode (S_{43}) refers to the response from the array common port to the antenna interface as shown in Fig. 4.3. It includes the Wilkinson beamformer (at RF or IF), the beamformer chips and the chip-to-antenna connections. If a transceiver is used at the sum port, it also includes the transceiver response (reference port is 1' and 4'). If the transceiver contains ADCs and DACs and has a digital interface, the 1' and 4' are digital bits at base-band. The channel response includes everything from (IF or baseband) to the antenna. The array BIST is divided into two steps. The first step is to test the individual channels states in terms of their gain and phase with respect to a reference state in the same channel (the zeroth state). The second step is to determine the array channel offsets when all the channels are in their reference states. More formally, the channel transfer function at row r, column c and in

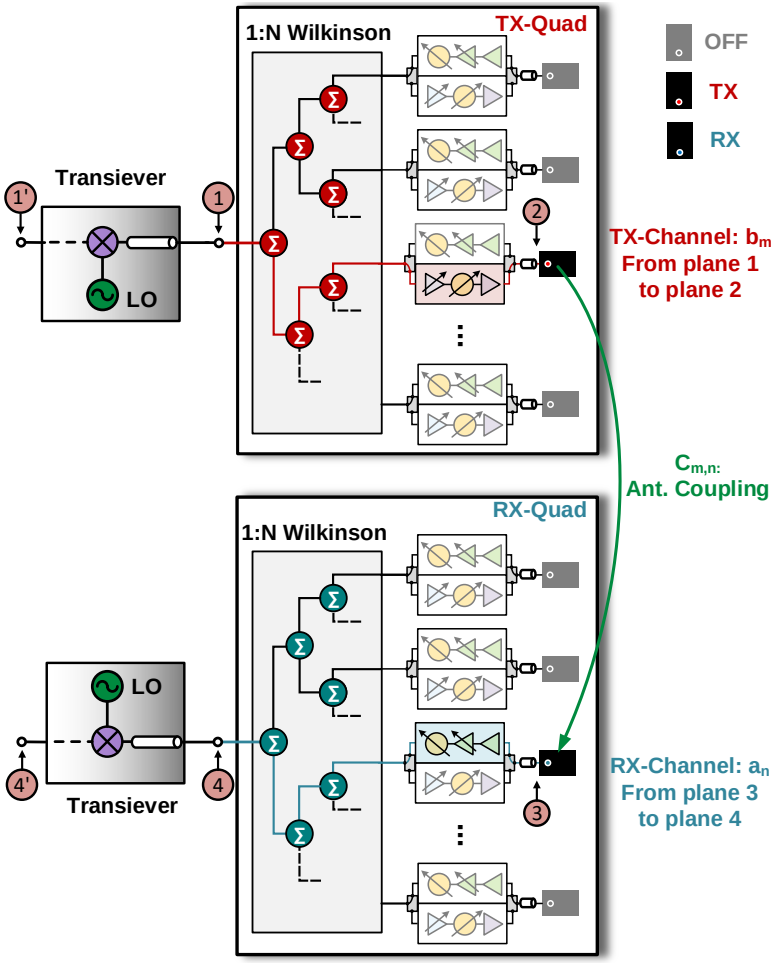

Figure 4.3: Phased-array- quadrant coupling and transmit/receive channel definitions.

state n is represented as:

$$\begin{aligned} a_{(r,c)}[n] &= a_{(r,c)}[0] \times \hat{a}_{(r,c)}[n] \\ &= a_{(0,0)}[0] \times \kappa_{(r,c)} \times \hat{a}_{(r,c)}[n] \end{aligned} \tag{4.2}$$

The self-normalized channel states ratios (SNCSRs) are written as $\hat{a}_{(r,c)}[n] = a_{(r,c)}[n]/a_{(r,c)}[0]$. The channel-to-reference-channel ratios (CCRs) are written as $\kappa_{(r,c)} = a_{(r,c)}[0]/a_{(0,0)}[0]$. Once the CCRs , $\kappa_{(r,c)}$, and the SNCRs, $\hat{a}_{(r,c)}$ are determined for all the channels, the array is calibrated and these values can be fed into a beam-setting processor to produce the correct channel excitation for any desired beam shape within a scaling constant factor $a_{(0,0)}[0]$.

4.3.1 Antenna Mutual-Coupling

The mutual coupling between neighboring antennas is first analyzed. Since, the excitation signal originates from an antenna in a different quadrant than the receive antenna, the coupling distance can be up to $N \times d$, when a quadrant is composed of $N \times N$ elements.

A $4 \times [4 \times 4]$ antenna array is simulated at 28-GHz with a spacing of 5.1 mm in both the x- and y- directions. Four antenna probes are also added, P[1-4], for additional assistance in the calibration. The array element is a probe-fed stacked-microstrip antenna with a driven bottom patch and a parasitic top patch for bandwidth improvement. The substrate is Megtron-6 with $\varepsilon_r \approx 3.3$ at 30 GHz. The antenna coupling reference plane is taken as the co-axial feed port as shown in Fig. 4.4a. The simulated reflection coefficients of all the antennas is < -10 dB at 28-31 GHz (Fig. 4.4b).

Fig.4.4c, presents the port-to-port coupling between two antennas separated by N-elements in the E-plane, H-plane, and the diagonal-plane. The coupling along the E-plane, $C_E(n)$, is expectedly the strongest for a given distance [48–50], starting at -20 dB for the closest neighbor and decaying at average rate of about -7.5 dB per element. The H-plane coupling, $C_H(n)$, starts at -21 dB for the first neighbor but drops at an average rate of -11.5 dB per element. The D-plane coupling, $C_D(n)$, starts at -35 dB for the first neighbor and drops moderately at an average rate of -9 dB per element. Note that the mutual coupling is in the near-field and does not follow the far-field Friis equation predicting 20 dB/decade power drops versus distance.

4.3.2 Coupling Symmetries

In order to calibrate the different channels with respect to each other ($\kappa^{(r,c)}$), the mutual-coupling symmetries are used. This is because each transmission measurement between an antenna pair produces an equation with three unknown quantities (the TX-channel-response, the mutual coupling, and the RX-channel response). Even if a common fixed TX antenna is used, the

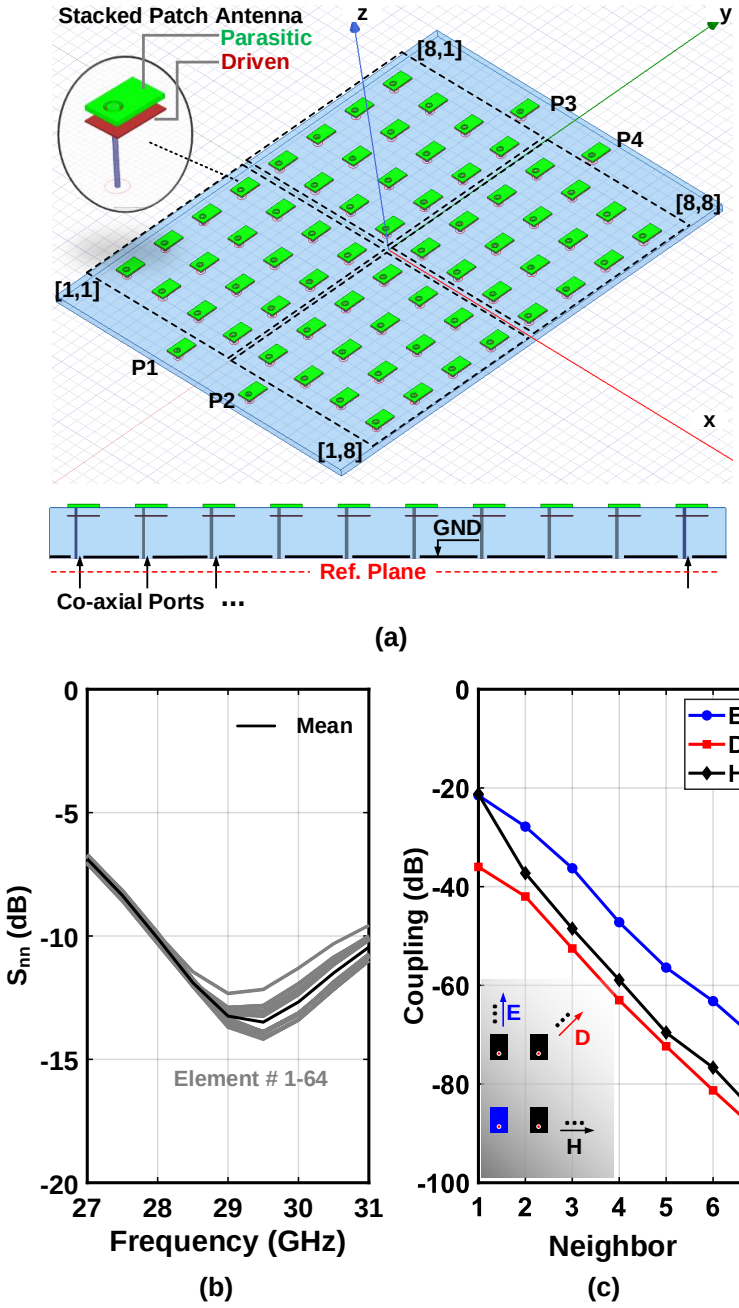

Figure 4.4: Antenna couplings simulation results: (a) simulation model, (b) antenna reflection coefficients and (c) antenna-to-antenna coupling levels for different distances and lattice directions at 30 GHz.

mutual-coupling coefficients from the TX antenna to the different RX antennas under-test need to be known. In practice, simulations do not predict the mutual coupling accurately-enough to produce low-calibration errors. This is especially true since the mutual-coupling can be -60 dB to

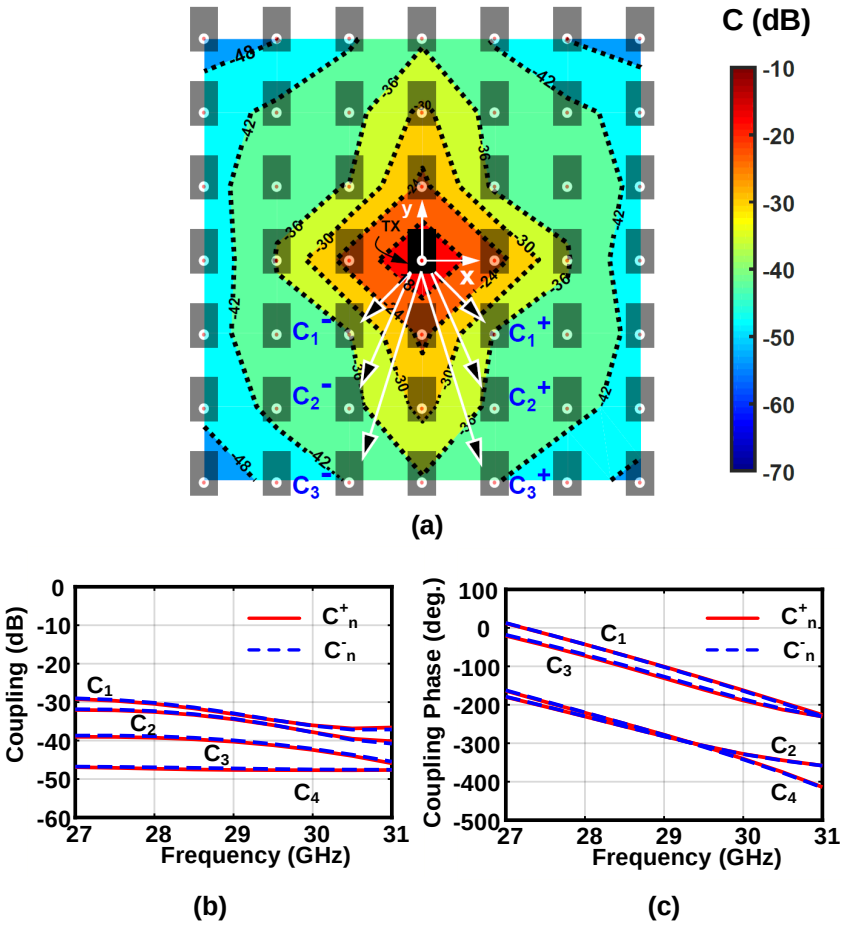

Figure 4.5: Simulated antenna couplings: (a) 2D heat-map at 30 GHz, (b,c) symmetric coupling coefficients versus frequency in magnitude and phase, respectively.

-80 dB, and this is hard to simulate accurately using numerical techniques. For example, a ± 1 dB error for a -80 dB value requires a convergence error of 1e-5, and this needs to be met for a large phased array simulation model with >5 million tetrahedral mesh cells.

However, phased-arrays with uniform spacing and natural symmetry can present distinct advantages for mutual coupling (Fig. 4.5a) [4, 51]. A key observation is that although coupling is generally direction dependant, it exhibits even symmetry around the antenna axes (x/y-axis in Fig. 4.5a). The first neighbor diagonal coupling looking to the left and to the right are the same $(C_1{}^- = C_1{}^+)$. This is also true for the second $(C_2{}^- = C_2{}^+)$, third $(C_3{}^- = C_3{}^+)$, and in general the n$^{\text{th}}$ neighbor diagonal couplings $(C_n{}^- = C_n{}^+)$. Since this symmetry is based on geometry, it

holds true for both magnitudes and phases of the mutual coupling coefficients and is independent of frequency (Fig. 4.5(b,c)). Also, since the array is periodic, the couplings properties are also periodic, and the results in Fig. 4.5 are applicable to any antenna location in an infinite array.

4.3.3 Channel-to- Reference-Channel Ratio Extraction

Consider the case of four arrays arranged in quadrants, which is a common way for building multi-beam hybrid-beamforming arrays (Fig. 4.6). The arrays are assumed to be on a half-wavelength grid, and each array is capable of transmit and receive functionalities. Each Quad-array consists of 16 elements (4x4) but it can be NxN without affecting the calibration procedure.

Consider now the scenario to calibrate[1] a given Quad, labeled Quad(A), using the neighbouring Quads(B,D). The procedure is illustrated below for Quad(A) in the RX mode, but it also applies for Quad(A) in the TX mode (just reverse the TX and RX operations below). The channel transfer functions at (row i and column j) are labeled as $a_{i,j}$ for Quad(A) RX channels, and as $b_{i,j}$ and $d_{i,j}$ for Quad(B) and Quad(D) TX channels, respectively. As mentioned earlier, the channel transfer function refers to the overall response from the array co-axial ports to the antenna. The calibration coefficients are denoted by $\kappa^{i,j}$ which refer to the ratio of channel $a_{i,j}$ to the reference channel in the same Quad(A), chosen as $a_{1,1}$. Moreover, we refer to intermediate calibration coefficients (channel $a_{i,j}$ with respect to channel $a_{m,n}$) as $\kappa^{i,j}_{m,n} = a_{i,j}/a_{m,n}$.

Calibrating Rows in Quad(A)

Each row is first calibrated with respect to its own reference channel, and these are chosen to be the left-most channels $a_{i,1}$ for a given row i (Fig. 4.6). For this purpose, Quad(B) directly above Quad(A) is used. The signal is injected into the RF input port of Quad(B) and picked up

[1] Calibrating a Quad is used synonymously to mean extracting the channel-to-reference-channel-ratios $\kappa^{(r,c)}$, and not necessarily aligning their phases and gains.

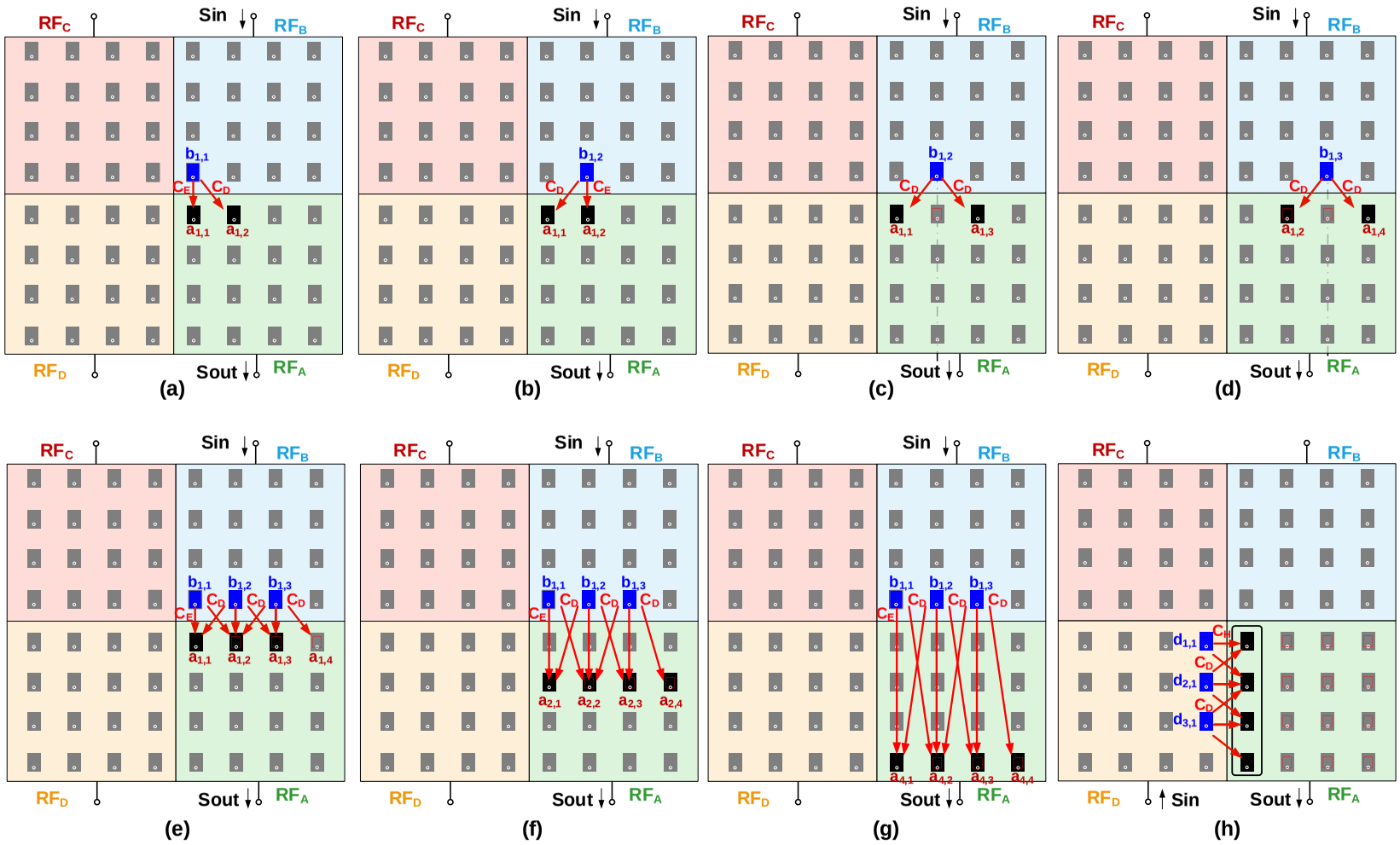

Figure 4.6: Traversal steps, calibrating the first row: (a,b) virtual pivot at $b_{1,1}, b_{1,2}$, (c,d) pivot at $b_{1,2}$, $b_{1,3}$ and (e) Row 1 completed w..r.t. $a_{1,1}$. (f,g) calibrating Row 2, Row 4 w.r.t. $a_{2,1}$ and $a_{4,1}$ respectively (h) calibrating the reference column w.r.t $a_{1,1}$.

from Quad(A)'s RF output port, and is done as a typical S_{21} measurement using a VNA. For all measurements, only a pair of channels (1 TX in Quad(B) and 1 RX in Quad(A)) are active with all other channels are in the OFF state. In order to calibrate the first row, we begin by transmitting from antenna $b_{1,1}$ and receiving from antenna $a_{1,1}$, and then $a_{1,2}$. Then transmitting from antenna $b_{1,2}$ and receiving from antenna $a_{1,1}$, and then $a_{1,2}$ (Fig. 4.6(a,b)). These four measurements can be expressed as:

$$M_1(b_{1,1} \rightarrow a_{1,1}) = \frac{\mathrm{S_{out}}}{\mathrm{S_{in}}} = b_{1,1} C_E^1 a_{1,1} \tag{4.3}$$

$$M_2(b_{1,1} \rightarrow a_{1,2}) = \frac{\mathrm{S_{out}}}{\mathrm{S_{in}}} = b_{1,1} C_D^1 a_{1,2} \tag{4.4}$$

$$M_3(b_{1,2} \rightarrow a_{1,1}) = \frac{\mathrm{S_{out}}}{\mathrm{S_{in}}} = b_{1,2} C_D^1 a_{1,1} \tag{4.5}$$

$$M_4(b_{1,2} \rightarrow a_{1,2}) = \frac{\mathrm{S_{out}}}{\mathrm{S_{in}}} = b_{1,2} C_E^1 a_{1,2} \tag{4.6}$$

Note that coupling C_E^1 and C_D^1 are the same in (4.3), (4.6) and (4.4), (4.5) above due to the array symmetry and periodicity. The calibration coefficient for channel $a_{1,2}$ can be obtained using:

$$\kappa_{1,1}^{2,1} = \frac{a_{2,1}}{a_{1,1}} = \sqrt{\frac{M_2}{M_1}\frac{M_4}{M_3}} = \sqrt{\frac{b_{1,1} C_D^1 a_{1,2}}{b_{1,1} C_E^1 a_{1,1}} \frac{b_{1,2} C_E^1 a_{1,2}}{b_{1,2} C_D^1 a_{1,1}}} \tag{4.7}$$

Notice that in obtaining the relative ratio, no apriori knowledge of the mutual-coupling or the TX-channel information is needed as these cancel out in (4.7). We refer to the steps above as using channels ($b_{1,1}$, $b_{1,2}$) as a *virtual-pivot* to do a relative calibration between $a_{1,2}$ and $a_{1,1}$.

Similarly, in Fig. 4.6c, the calibration coefficient for channel $a_{1,3}$ can be obtained by direct division of the two measurements (M_5 and M_3) as the mutual coupling from the Tx channel

antenna to the two receive antennas is the same. In this case,

$$M_5(b_{1,2} \rightarrow a_{1,3}) = \frac{\mathrm{S_{out}}}{\mathrm{S_{in}}} = b_{1,2} C_D^1 a_{1,3} \tag{4.8}$$

$$\kappa_{1,1}^{1,3} = \frac{a_{1,3}}{a_{1,1}} = \frac{M_5}{M_3} = \frac{b_{1,2} C_D^1 a_{1,3}}{b_{1,2} C_D^1 a_{1,1}} \tag{4.9}$$

This step is referred to as using $b_{1,2}$ as a *pivot* for obtaining the relative ratio of $a_{1,3}$ to $a_{1,1}$. Note that direct pivoting requires only two measurements, but four measurements are needed for a virtual pivot. Also, a virtual pivot results in two solutions with 180° phase difference. The choice of the correct phase needs to be based of coarse knowledge of the expected phases (within ±90° margin) or it can be alleviated through the addition of extra off-grid antenna probes, such as (P$[1-4]$) in Fig. 4.4a

Following the same steps, $b_{1,3}$ can pivot channels $(a_{1,2}, a_{1,4})$ to obtain $\kappa_{1,2}^{1,4} = a_{1,2}/a_{1,4}$ as shown in Fig. 4.6d. By simple processing, one can also calculate $\kappa_{1,4}^{1,1}$ as:

$$\kappa_{1,1}^{1,4} = \kappa_{1,2}^{1,4} \times \kappa_{1,1}^{1,2}, \tag{4.10}$$

and with this, the calibration coefficients of the first row relative to $a_{1,1}$ ($\kappa_{1,1}^{1,2}, \kappa_{1,1}^{1,3}, \kappa_{1,1}^{1,4}$) are all known. This process is then repeated for rows 2, 3 and 4 to obtain all channels relative to the reference channels in their first column: $a_{1,1}, a_{2,1}, a_{3,1}, a_{4,1}$, as shown in Fig. 4.6(e,f,g).

Calibrating the Reference Column in Quad(A)

After the extraction of the calibration coefficients for rows with respect to their reference channels ($a_{[1-4],1}$) is completed, one needs to extract the calibration coefficients of the reference column itself with respect to the reference channel of the Quad ($a_{1,1}$). This is achieved using the same manner described above but using Quad(D) as the TX source (Fig. 4.6h). After this step, all

the channel coefficients for Quad(A), $\kappa^{(r,c)}$, are determined with respect to $a_{1,1}$.

Quad B, C, D Calibration

The same procedure is now applied to the different quadrants as shown in Fig. 4.7(a,b,c). For example, for Quad B calibration, Quad A and Quad C are used as transmitters, and all the channels in Quad B are referenced to $b_{1,1}$. Each Quad is then independently calibrated with respect to its own reference channel $a_{1,1}, b_{1,1}, c_{1,1}, d_{1,1}$.

If each quadrant is operating independently, then the array calibration can stop here. However, in most cases, the quadrants are combined together, either to produce a single large aperture with a narrow beam, or for a 4×4 MIMO link. Therefore, it is important to calibrate the quads with respect to each other. This is done in Step 4.

Quad-to-Quad Calibration

Mutual coupling and pivoting is also used to align the calibrate the quads all together (Fig. 4.7d). For example, $d_{1,1}/a_{1,1}$ can be obtained by virtual pivoting on $(b_{1,1}, c_{1,1})$. Similarly $b_{1,1}/a_{1,1}$ can be obtained by virtual pivoting on $(c_{1,1}, d_{1,1})$, and $b_{1,1}/c_{1,1}$ by virtual pivoting on $(a_{1,1}, d_{1,1})$. This determines $b_{1,1}, c_{1,1}, d_{1,1}$ with respect to $a_{1,1}$ and therefore all 64-channels are determined with respect to $a_{1,1}$. The procedure above is also valid for 4x(8x8) arrays or larger. Any 4x(NxN) arrays can be calibrated, first at the Quad level and then tying the Quads together as shown above.

4.4 Dynamic Range and Accuracy Analysis

Fig.4.8a presents the system analysis for near-field coupling between a pair of transmit and receive antennas. Only one channel is active in a given quadrant array with the rest de-activated (OFF). Each quadrant has a 1:N Wilkinson network to divide or combine the signal from the

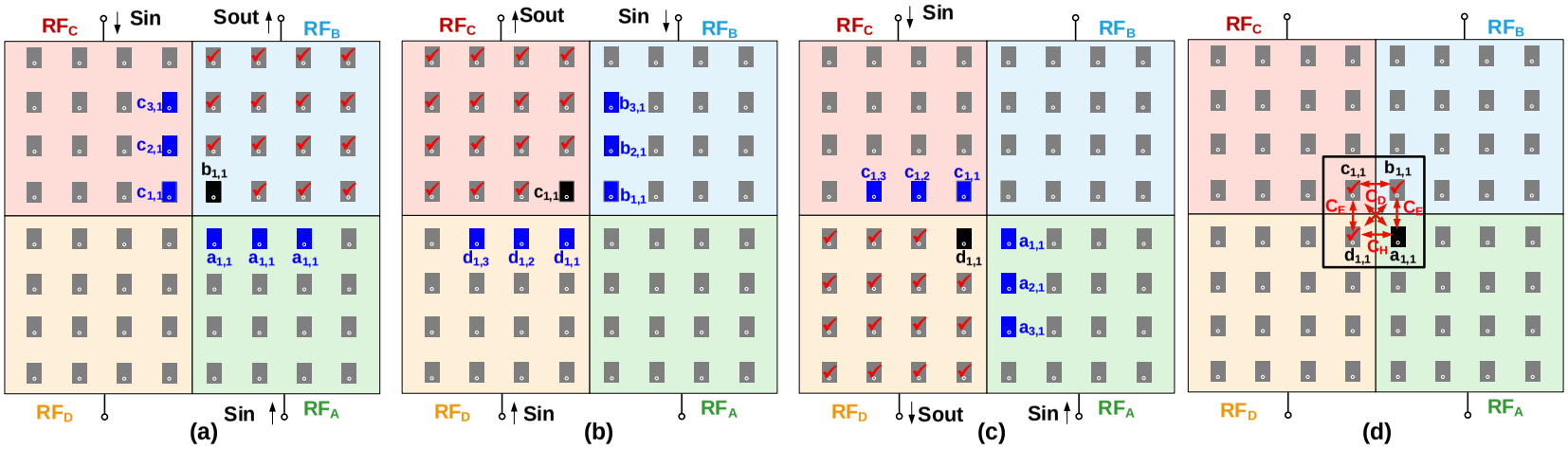

Figure 4.7: Calibrating remaining Quads in Rx-mode: (a) Quad B using Quad (A,C) in Tx mode, (b) Quad C using Quad (B,D) in Tx mode and (d) Quad D using Quad (A,C) in Tx mode and (d) inter-quad calibration of reference elements.

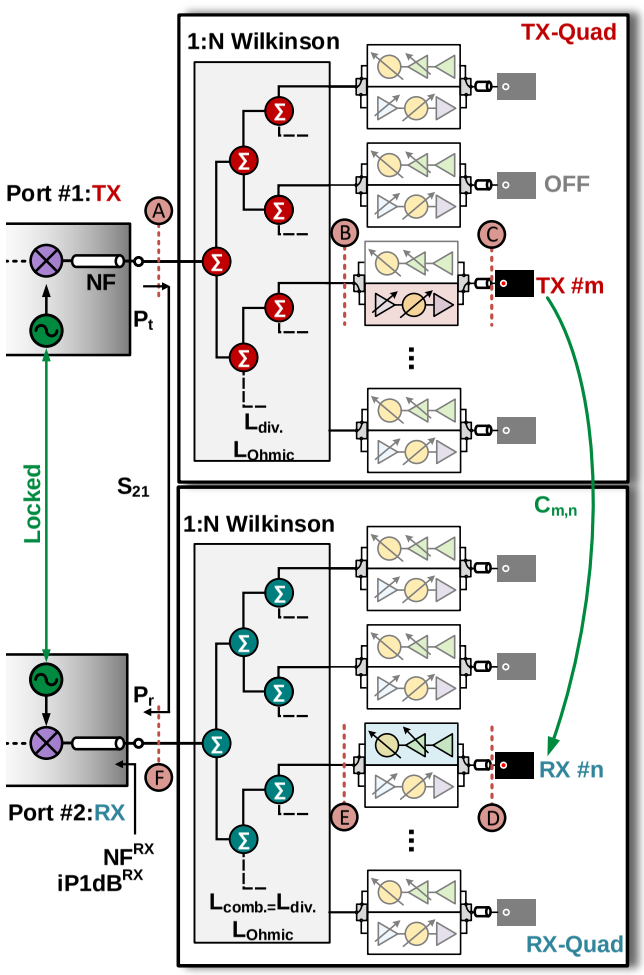

(a)

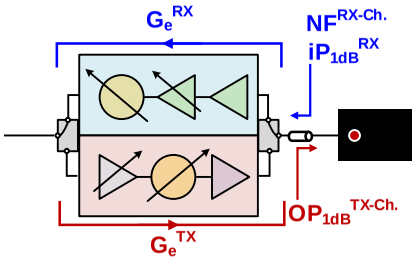

Param.	Describtion	Value 4x4 Quads	Value 8x8 Quads
P_t	Power Transmitted	-16 dBm	-5 dBm
$L_{div.}$	Division Loss	12 dB	18 dB
L_{Ohmic}	Ohmic Losses	3 dB	5 dB
$G_e^{TX-Ch.}$	TX Chan. Gain	24 dB	
$OP_{1dB}^{TX-Ch.}$	TX Chan. OP1dB	12 dB	
Min [$C_{m,n}$]	Ant-to-Ant Coupling	-45 dB	-80 dB
G_e^{RX}	RX Chan. Gain	21 dB	
$NF^{RX-Ch.}$	RX Chan. NF	4.8 dB	
$IP_{1dB}^{RX-Ch.}$	RX Chan. IP1dB	-20 dBm.	
Min. [Pr]	Power Recieved	-45 dBm	-70 dBm
NF^{MXR}	Mixer NF TX/RX	15/13 dB	
$IP1dB^{MXR-RX}$	Mixer iP1dB-RX	0 dBm	
$OP1dB^{MXR-TX}$	Mixer oP1dB-RX	8 dBm	

Point	4x4-Quads S dBm	4x4-Quads N dBm/Hz	8x8-Quads S dBm	8x8-Quads N dBm/Hz
A	-16	-159	-8	-159
B	-31	-163	-31	-163
C	-7	-139	-7	-139
D*	-52	-169	-87	-169
E*	-31	-148	-66	-148
F*	-47	-159	-89	-161

(b)

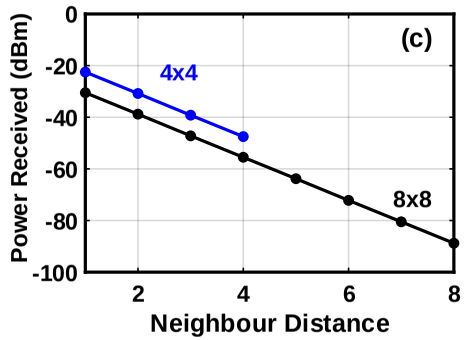

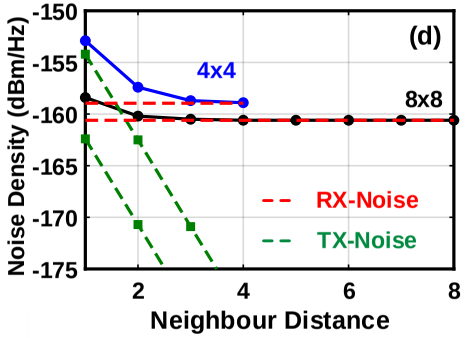

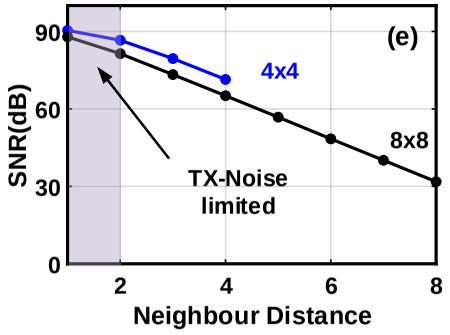

Figure 4.8: Near-field coupling link-budget: (a) phased-array quadrants coupling block-diagram, (b) signal and noise levels at different points in the chain, (c,d ,e) simulated received power, noise density and signal-to-noise ratio at the RX array output (point F) for different TX-RX antenna separations at 30 GHz for 4×4 and 8×8 quadrants size respectively.

different channels. The beam-forming network, electronic channels and up-down/conversion mixer parameters are shown in Fig.4.8.

The RX-quadrant elements are considered to be “under test" and excited from the nearest E-plane neighbor in the TX-quadrant. The RX-channel is iterated through all of its different phase and gain states and a set of S_{21} measurements are recorded between the TX-quadrant port (point A) and RX-quadrant port (point F) for each RX-channel-state. Denoting the transmission measurement from m-th TX-element in its zeroth state to the n-th RX element in its k-th state as:

$$M(b_m[0] \rightarrow a_n[k]) = b_m[0] \times C_{m,n} \times a_n[k] \tag{4.11}$$

The RX-channel self-normalized channel coefficients are obtained as:

$$\begin{aligned} \hat{a}_{(r,c)}[n] &= \frac{M(b_m[0] \rightarrow a_{(r,c)}[n])}{M(b_m[0] \rightarrow a_{(r,c)}[0])} \\ &= \frac{b_m[0] \times C_{m,n} \times a_{(r,c)}[n]}{b_m[0] \times C_{m,n} \times a_{(r,c)}[0]} \\ &= \frac{a_{(r,c)}[n]}{a_{(r,c)}[0]} \end{aligned} \tag{4.12}$$

which is the first step of the in-situ characterization and each channel is characterized with respect to its own reference state.

Two quadrant size are now considered, 4×4 and 8×8. The coupling distance is up to the 8^{th}-neighbor for an 8x8-quadrant and up to 4^{th}-neighbor for the 4x4-quadrant. Also, the Wilkinson network loss is different. The insertion loss, when one channel is ON, for an 8×8 array is 23 dB due to 18 dB of division loss and 5 dB ohmic loss, while it is 15 dB for a 4×4 due to 12 dB of division loss and 3 dB of ohmic loss.

To maximize the signal-to-noise ratio and channel characterization accuracy, the transmit power should be maximized. In this case, although the maximum power for a given TX-channel is 11 dBm, the TX power is chosen to be -7 dBm. This is done in order to ensure the closest neighbor

in the receive array is not saturated or compressed. At this power level, the nearest RX-channel receives ∼-7-21=-28 dBm and is 8 dB below the channel input P1dB. For a TX-channel output power of -7 dBm, the input power required at the TX array input (point A) is -16 dBm and -8 dBm for a 4x4 and 8x8 case, respectively. This is well within the transceiver output power range (OP1dB=8 dBm). For the 4x4 array, the received power at the array point F is -22 dBm (nearest neighbor) to -47 dBm (furthest neighbor) where as for the 8x8 case, the power level is -30 dBm (nearest neighbor) to -90 dBm (furthest neighbor).

The noise level at the output generally depend on both TX-noise sources and RX-noise sources. In the present case, L.O. phase noise does not contribute since the same L.O. source is used for up- and down-conversion. The TX-noise at point C is dominated by the channel noise $N_C^{TX} = -139$ dBm/Hz as the mixer noise contribution is much lower due to the Wilkisnon network losses ($-150, -158$ dBm/Hz for the 4x4 and 8x8 quadrant size). The output noise levels at point F for different RX-element distances are displayed in Fig. 4.8d. It can be observed that the closest two elements noise levels are higher than the rest due to the contribution of the TX-noise, beyond the fourth neighbor the output noise is nearly constant. It is worth mentioning that the RX- noise is different from the case when the entire RX-array is receiving. This is due to the fact the Wilkinson network adds extra $10\log(N)$ losses when only one channel is ON, which significantly drops the overall gain before the noisy mixer. This becomes more clear in the 8x8 case because when the entire array is ON the equivalent RX noise figure is 5.7 dB, which is 0.8 dB higher than the channel noise figure. However when only one channel is ON, the network loss is 23 dB instead of 5 dB, and the resulting noise figure is 15.4 dB, which 9 dB higher than the channel noise figure and is mainly determined by the RX-mixer noise figure.

The resulting signal to noise ratio is illustrated in Fig. 4.8e. For an integration bandwidth of 10 KHz (100-μsec integration time), a signal-to-noise ratio $\geq$30 dB can be realized for the furthest element in an 8x8 array and $\geq$60 dB fo a 4x4 array. The SNR for close-in element is limited to about 90 dB due to thr TX-noise. Note that the presented results are all when the

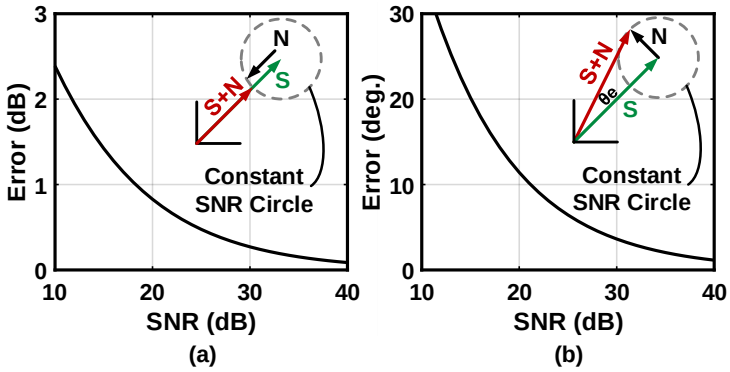

Figure 4.9: Simulated relative channel state error for different measurement SNR levels: (a) amplitude error and (b) phase error.

RX-channel is operated at its maximum gain. When the RX-channel gain is dropped to lower gain states for characterization, the integration time needs to be increased accordingly to maintain the same SNR.

Having higher SNR translates to higher accuracy in the channel characterization, the resulting error will depend on the relative angle between the signal and noise vectors. It can shown that, for a given SNR, the worst case phase error will occur when the noise and signal vectors are orthogonal whereas the worst case amplitude error will occur when the noise and signal are parallel or anti-parallel. Since, in the case of computing relative channel ratios two measurements are done, the errors add up. The channel self-normalized coefficient errors, $\hat{a}_{(r,c)}[n]$, can be estimated from (4.2), (4.3) for a given measurement SNR. The results are also displayed in Fig. 4.9, and show that for errors less than 0.5 dB and 5 degrees a SNR better than 25 dB is needed.

$$\text{Error (dB)} \leq 20\log(1+10^{-SNR/20}) \tag{4.13}$$

$$\text{Error (deg.)} \leq 2\tan^{-1}(10^{-SNR/20}) \tag{4.14}$$

4.5 Implementation and Measurements

Two different arrays were used to verify the quadrant-level calibration (QL-Cal) method. The first test array is a 4x(4x4) phased array, Fig. 4.10(a-b), where each Quad is a 4x4 array employing TRX beam-former chips and 1:4 Wilkinson divider/combiner network (Fig. 4.10b). The beamformer chips are flipped onto the top metal layer and connected to co-axial antenna-feeds using CPW transmission lines to feed the patch antennas on the bottom metal layer. The antennas are placed in a square grid with a spacing of 5.1 mm ($\lambda_\circ/2$ at 29.5 GHz). Two dummy antenna rows are added on the edges of the array to mitigate edge effects and simulate a larger array. Also,

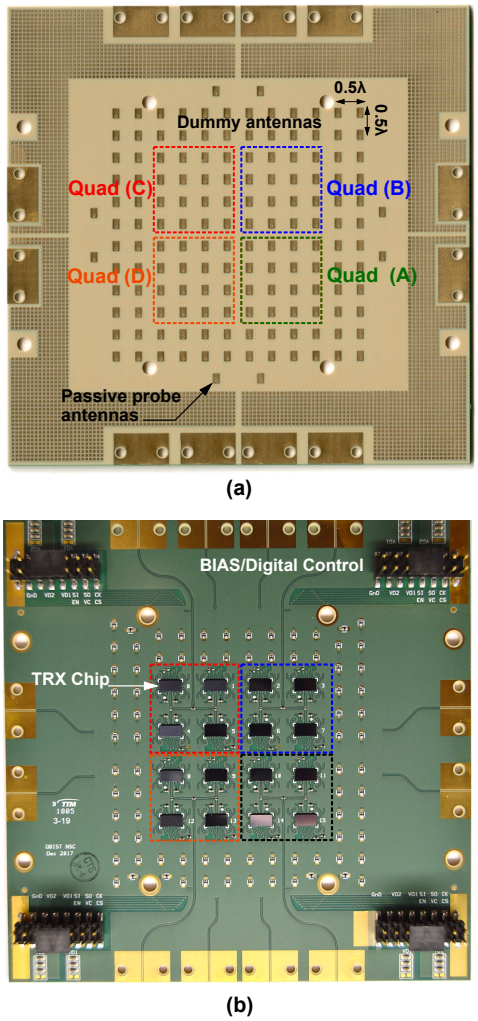

Figure 4.10: Fabricated 5G Quadrant-based 2x2 MIMO Phased Arrays with 4×4 quadrants: (a) antenna-side and (b) chip-side

Table 4.1: Phased Arrays Main Parameters

Parameter	4×4	8×8
Antenna grid dx/dy (mm)	5.1/5.1	5.1/5.9
Bandwidth (GHz)	28-31	24.5-29.5
RX-Chan. Gain (dB)	18	25
RX-Chan. NF (dB)	4.8	5.3
RX-Cahn. IP1dB	-21	-29
TX-Chan. Gain (dB)	26	27
TX-Chan. NF (dB)	11	16
TX-Chan. OP1dB	11	11
Phase Shifter step (deg.)	5.6	5.6
VGA Gain Control Range (dB)	10+7	10+7

two passive antennas are included in each Quad with an offset of half a grid cell (Fig. 4.10b). A 2x2 SiGe beamformer-chip is employed for the construction of this phased array [5, 52]. The SiGe chip contains four TRX channels operating at higher-side of the 5G FR-2 band (28-32 GHz). Each channel has a 4-bit variable gain amplifier (VGA) and a 6-bit phase shifter. The chip results in a noise figure of 4.6 dB in the RX-mode and an output power of 11.5 dBm at P1dB in the TX-mode. An SPI interface is used to turn the channels ON and OFF, and for gain and phase control.

The second test array is a 4x(8x8) as shown in Fig. 4.11, having the same architecture and a very similar 2x2 SiGe chip and antennas but operates in the lower end of the 28-GHz 5G band (25-29 GHz) [53]. In this array, the antennas are placed on slightly rectangular grid with $dx = 5.1$ mm and $dy = 5.9$ mm allow more scanning in the horizontal plane than in the vertical plane. Also, the antenna co-axial feeds are rotated every other row to minimize cross-polarization in the H-plane scan. No extra dummies or probes are employed in this array. The fabricated arrays main specifications are summarized in Table 4.1.

The setup used for characterizing the array is shown in Fig. 4.12 and allows for doing both mutual-coupling experiments as well as far-field calibration and evaluation for bench marking the quadrant-level mutual-coupling-based calibration. First, the arrays are characterized using a standard gain horn antenna in the far-field. The distance between the horn to the array is 1.9 m,

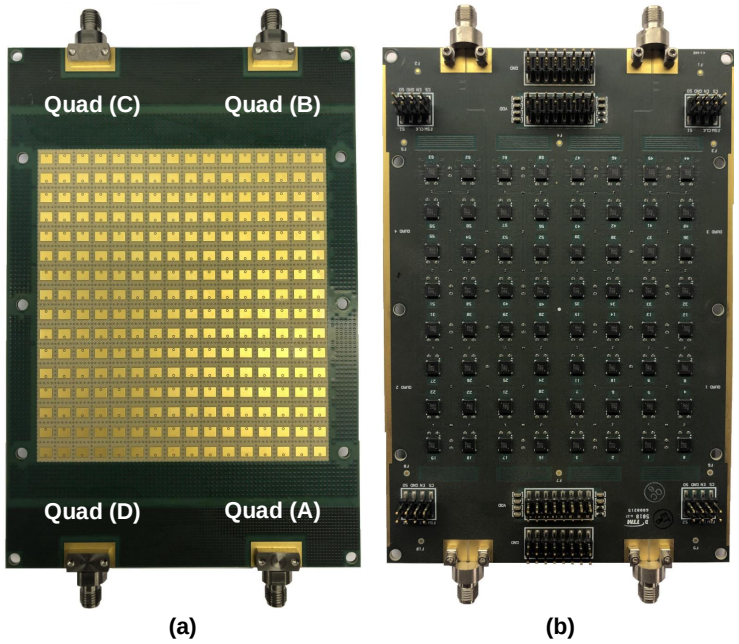

Figure 4.11: $4 \times [8 \times 8]$ phased-array photo: (a) antenna side and (b) chip-side.

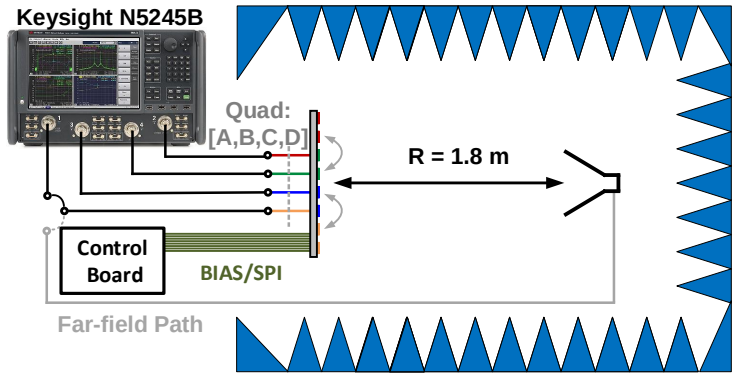

Figure 4.12: Measurement set-up for near-field mutual coupling and far-field testing.

which results in near-ideal uniform phase illumination over the array aperture with negligible phase curvature, less than $< 3^{\circ}$, at the corners. The array channels are then turned ON one at a time and the transmission between the horn and the array ports (S_{21}) is recorded for each channel and for every channel gain/phase state.

In the second step, the four Keysights PNA-X ports are connected to the four co-axial ports of quadrants of the arrays under test and transmission measurements are carried out between

the different elements. The cabling loss (≈5 dB) and the higher noise figure of the wide-band high linearity receivers of the PNA-X result in a substantial increase in the total RX noise figure to about 40 dB. Therefore, the IFBW of the measurements was reduced to be 10-100 Hz to ensure a sufficiently high SNR ($>$ 30 dB) for both the coupling and far-field measurements in accordance with the analysis in Section(4.4). Note that with the use of tuned 5G transceivers integrated on phased array PCB, the RX noise figure could be easily reduced to 15-20 dB allowing for 100x integration time reduction in future implementations.

4.5.1 $4 \times [4 \times 4]$ Array Results and Finite-Isolation Effects

Initially, when comparing the results of channel characterization from far-field and BIST, an appreciable deviation from far-field results was observed. This deviation occurred particularly for weakly-coupled far-out channels and could produce errors up to to 3 dB/ 40 deg. when characterizing some of the 4th-neighbor channels. This error occurred despite of having a signal-to-noise ratio of $>$ 30 dB for the far-out couplings and did not diminish by neithe‘r increasing the integration time nor averaging the measurements.

Upon more investigation, the root cause of the problem was found to be un-desired TX-antenna to RX-Array output leakage. Un-like, the ideal-isolation situation analyzed in Section(4.4), the signal at the array output when one channel is ON, is not only due to the activated channel under test, but also there is leakage signal from the TX-antenna arriving at the output Fig. 4.13a. This is due to part of TX signal being received by the OFF-channel antennas that can still couple to the beam-forming network and appear at the arrays common port as well as due to the beam-forming network and RX-connectors directly receiving part of the radiated TX-energy. Fig. 4.13c shows the measured leakage level when everything (RX and TX) is OFF and when the all RX-array elements are OFF but with the one neighboring array TX-element ON. An S_{21} level of -70 dB is observed in the OFF/OFF case whereas a S_{21} of about -55 dB is observed when one TX-antenna is ON.

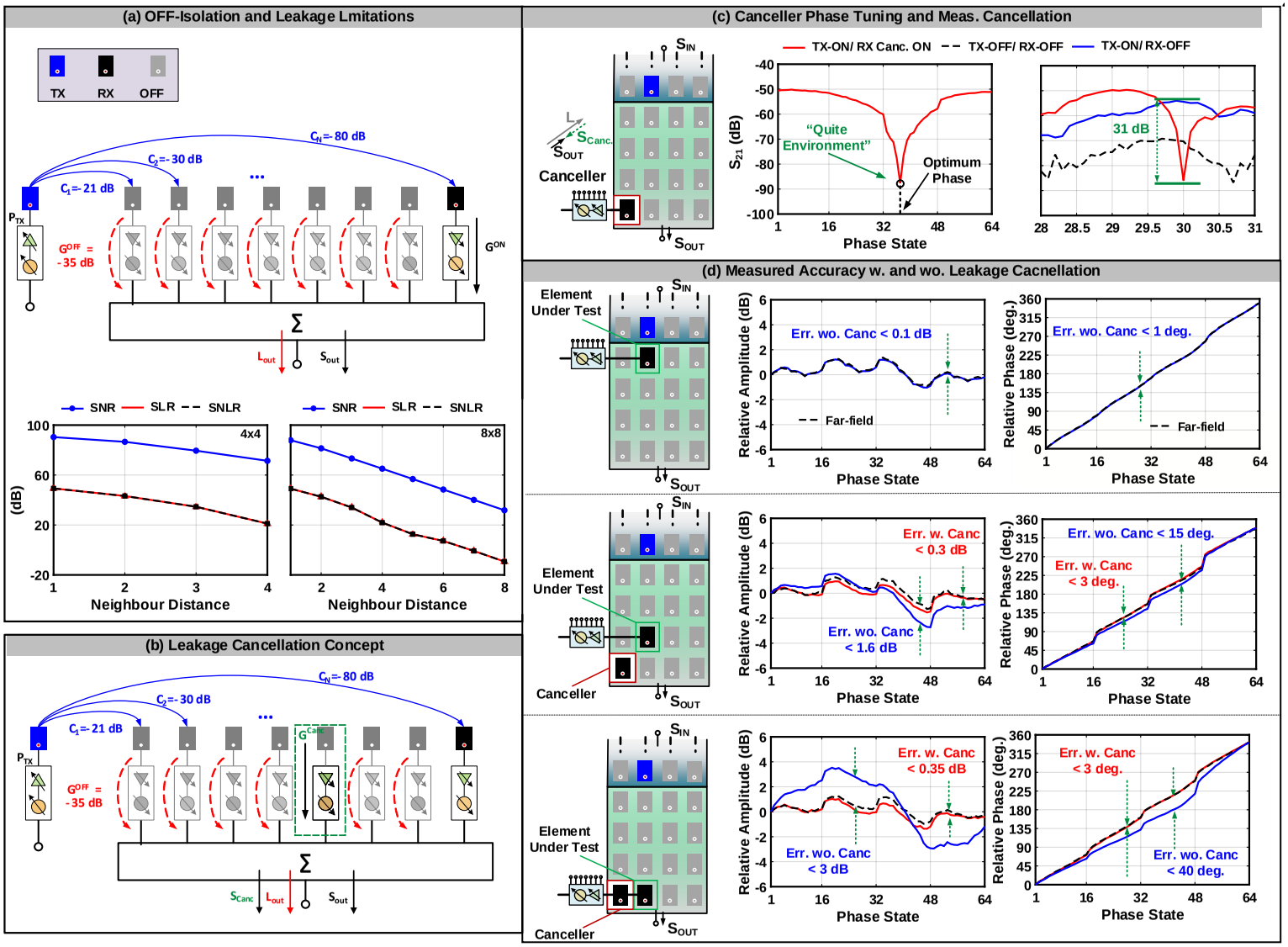

Figure 4.13: (a) Finite-isolation and leakage paths limitations, (b) Active-leakage cancellation concept, (c) Measured tuned-leakage canceller and (d) Measured quadrant-level characterization accuracy versus far-field for different element at 30 GHz with and without the use of a leakage canceller.

The scenario of OFF-Leakage is illustrated in Fig. 4.13a, where one TX-antenna is attempting to excite a far-off antenna in the presence of OFF channels having finite OFF-isolation gain of $G^{OFF} = -35$ dB. In this case, the output-leakage when the nth neighbor is being testing is:

$$L_n = \sum_{k=1,k\neq n}^{k=N} C_k G_k^{OFF} \tag{4.15}$$

which can be bounded by:

$$L_n^{max} \leq G^{OFF} \sum_{k=1,k\neq n}^{k=N} |C_k| \tag{4.16}$$

if the OFF- channel gain is the same, and the leakage paths are phase aligned which is the worst case. The following expression for the resulting signal-to-leakage ratio (SLR) can be obtained:

$$SLR_n^{min} = \frac{S_{out}}{L_{out}} = \left[\frac{G_m^{ON}}{G^{OFF}}\right] \times \left[\frac{C_n}{\sum_{k=1,k\neq n}^{k=N} |C_k|}\right] \tag{4.17}$$

Examining the signal-to-leakage ratio (SLR) expression above, it becomes clear that a low-coupling active path is at a disadvantage when competing with many close-in inactive leakage paths as given by the $\frac{C_n}{\sum_{k=1,k\neq n}^{k=N} |C_k|}$ term which can be as low as -80-(-20)=-60 dB for the far-out channels. Also, the effect of the ON-to-OFF gain ratio of the channel $\frac{G_m^{ON}}{G^{OFF}}$ becomes apparent. This ratio needs to be high even for the lowest VGA gain state of every channel to help obtain a high SLR and therefore an accurate characterization. The SLR expression is evaluated for different neighboring distances for the 4x4 and 8x8 quadrant size, based on the simulated coupling matrix of the antennas. The single-to-noise-and-leakage ratio (SNRL) is computed as:

$$SNLR_n^{min} = \frac{S_{out}}{N_{out} + L_{out}} = \frac{1}{SNR^{-1} + SLR^{-1}} \tag{4.18}$$

The results are illustrated in Fig.4.13a, showing that even for a 4th-neighbor case and just

considering the coupling through the OFF-channels, can lead to limiting the SNLR to 10/20 dB (at min/max gain) and as a result to substantially limit the channel characterization accuracy as observed in Fig. 4.13d despite the sufficiently low noise.

In order to resolve this problem, a leakage cancellation approach was sought. The idea is to activate an additional channel, different from the channel under test, and adjust its amplitude and phase in order to generate a signal at the output that has an equal magnitude to leakage signal but with an opposite phase ($S_{Canc.}(f_\circ) = L(f_\circ)e^{j\pi}$). This element is referred to as a leakage canceller. Fig. 4.13(b,c) illustrates the use of such approach, where originally a leakage level of -50 dB is observed. A suitable element, at min-gain state, is then chosen based on the required leakage level. Afterwards, the phase of that element is tuned and the output level is monitored. At a given phase, the output signal will reach a minimum level and hit the noise-floor in the case of prefect cancellation ($|S_{out}(f_\circ)| = |S_{Canc.}(f_\circ) - L(f_\circ)| \approx 0$). Once this state is reached the array is in a *quiet*-environment where leakage has been fully balanced. The canceller is kept ON in the this state and the channel-under-test characterization is carried out. The results of channel characterization with and without canceller for different elements are depicted in Fig. 4.13d. As can be seen, the use of canceller can significantly reduce the errors from 3 dB down to 0.3 dB and 40 deg. down to 3 deg. for the farthest-out elements.

The cancellation technique is applied to the different TX-probes when characterizing the channels of Quad(A). The results of the Quadrant level channel characterization of all Quadrant-A channels in the different VGA and phase shifter states are shown in Fig. 4.14 in comparison with their corresponding far-field counterparts at 30 GHz. The results agree very well with the far-field ones with peak error $\leq$0.35 dB/3°, this holds true even when the VGA is cycled to its lowest gain state which drops the SNLR by more than 10 dB relative to that at the max gain state and this is where most of the peak errors occur as observed in Fig. 4.14f. Note that, throughout the measurements, the phase shifters are cycled at maximum gain and the VGA is cycled at the zeroth phase with the reasonable assumption that they operate independently and that the overall

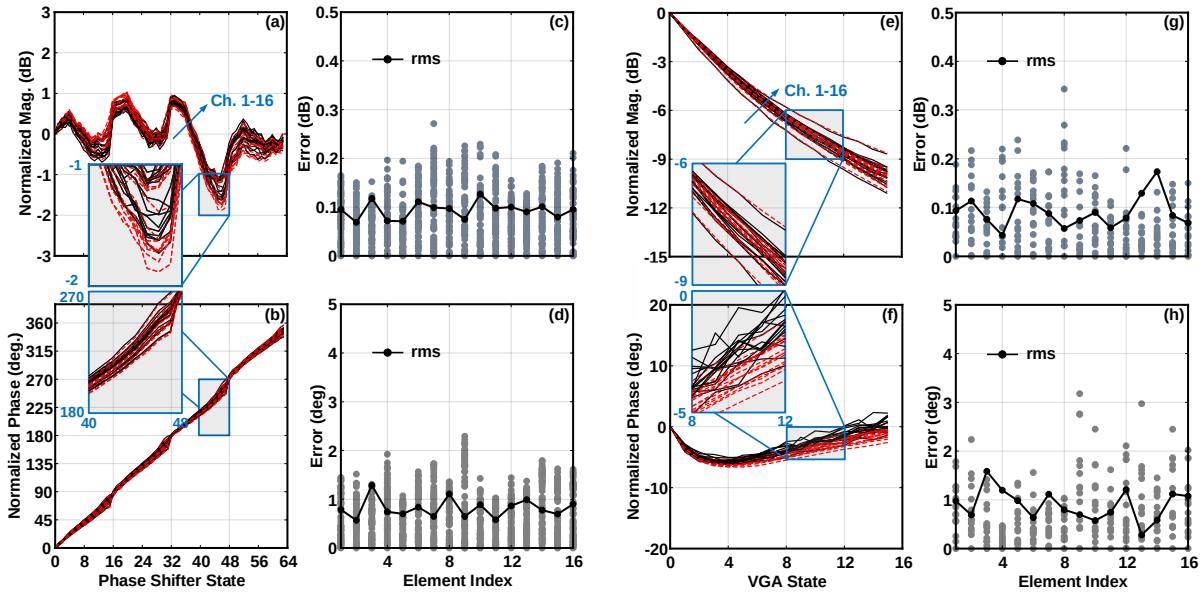

Figure 4.14: Measured channel-testing results for quadrant (A) using BIST and far-field characterizations at 30 GHz: (a,b) phase-shifter's gain versus phase-state and phase versus phase-state, (c,d) BIST errors relative to far-field for phase-shifter's gain versus phase-state and phase versus phase-state, (e,f) VGA's gain versus gain-state and phase versus gain-state, (g,d) BIST errors relative to far-field for VGA's gain versus gain-state and phase versus gain-state.

channel state is approximately the product of the VGA and phase shifter transfer characteristics $a(m,n) = a_{VGA}(n) \times a_{PS}(m)$. Although this assumption is not necessary, it is usually made when characterizing arrays. This is because it reduces the number of states to be characterized to 64 (phase states) + 16 (gain states) = 96 states instead of $16 \times 64 = 1024$ states, and hence introduces negligible errors.

A summary of the results of channel characterization of all qaundrants (A,B,C,D) in RX-mode is illustrated in Fig. 4.15. As can be seen the errors of the different quadrants are better than 2.5 dB/2.5°. The SLR in the near-field measurements is $\geq$ 50 for all the channels in all the quadrants in the maximum gain state. However, for the far-field, it is actually limited to about 30-40 dB, which is potentially due to the connector picking up part of the signal from the horn (even when covered). Observing the errors in Fig. 4.15(b,e), it is apparent that the errors follow an inverse relation with the far-field SLR in Fig. 4.15(a) Error(B)$\geq$ Error(C)$\geq$ Error(D) and FF-SLR(B)$\leq$ FF-SLR(C)$\leq$FF-SLR(D). This highly suggests that the error is driven by far-field

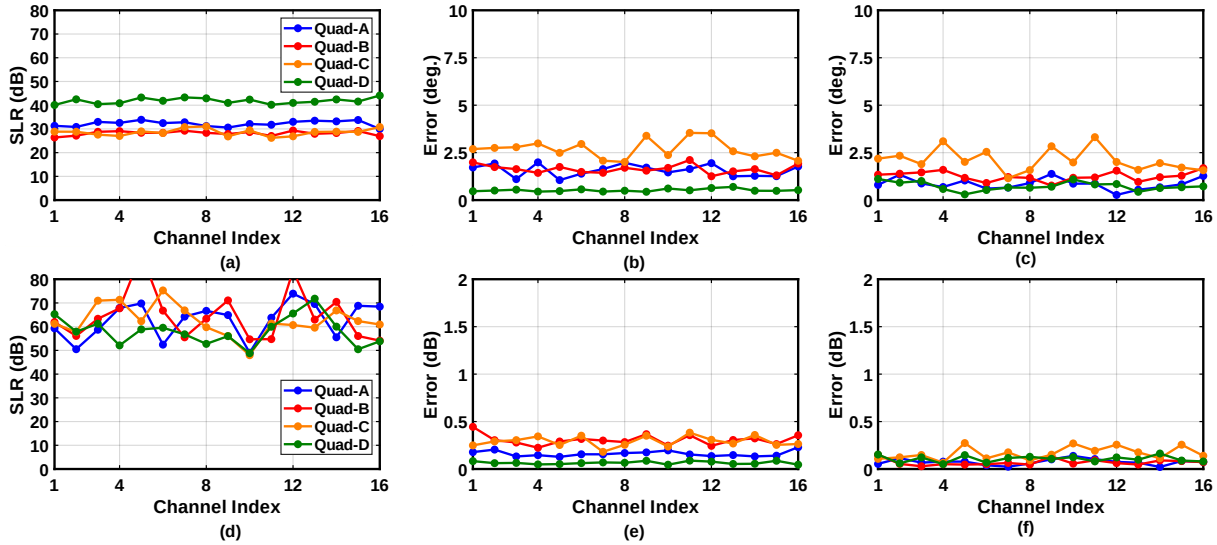

Figure 4.15: Measured Signal to Leakage Ratio (SLR) for the different 4x4-quadrants (A,B,C,D) in RX-mode at 30 GHz: (a) Far-field SLR, (b) BIST SLR, (c,d) Phase-shifter-states amplitude/phase errors, (e,f) VGA-states amplitude/phase errors.

limited-SLR and not by the near-field one.

The channel-to-channel gain and phase offsets of all 64-channels in the four quadrants relative to channel $a_{1,1}$ obtained from the far-field and BIST measurements are displayed in Fig. 4.16. It is observed that the far-field and BIST generally agree well within an rms error of 0.78 dB and 7.5°. More than eighty percent of errors are distributed around ± 1 dB, $\pm 10°$. Although the error are reasonable, they are noticeably higher than channel characterization error accuracy (limited by SLR). This is believed to be an inherent limitation due error-propagation involved in successive pivoting steps in the extraction procedure and will be further investigated in Section(4.6). The quadrant-level calibration data is used in order to correct of the channel offsets and variations in the VGA/Phase shifter characteristics and set the radiated beam. The beam is then measured in far-field to verify proper operation. Several cases are tested using Quad(A) in RX mode and are illustrated in Fig. 4.17. It is observed that the characterization results in near-ideal sum and difference beam patterns with side-lobe level of -12.5 dB and mono-pulse null depth of -30 dB.

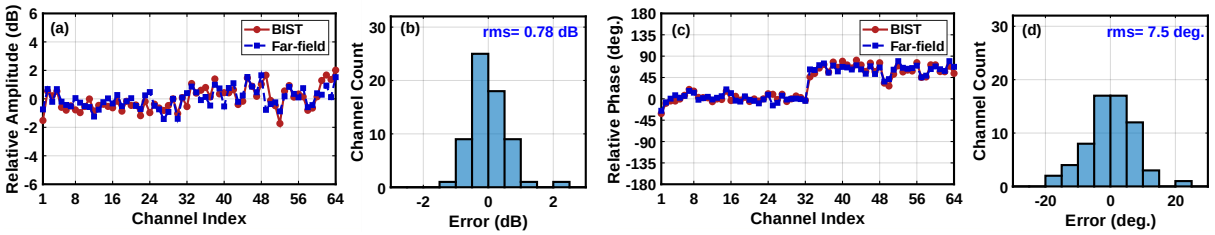

Figure 4.16: Measured channels relative gains/phases at the zeroth-state in RX-mode using BIST and far-field for all four 4x4-quadrants: (a) channel amplitudes, (b) channel amplitudes errors, (c) channel phases, (d) channel phases errors.

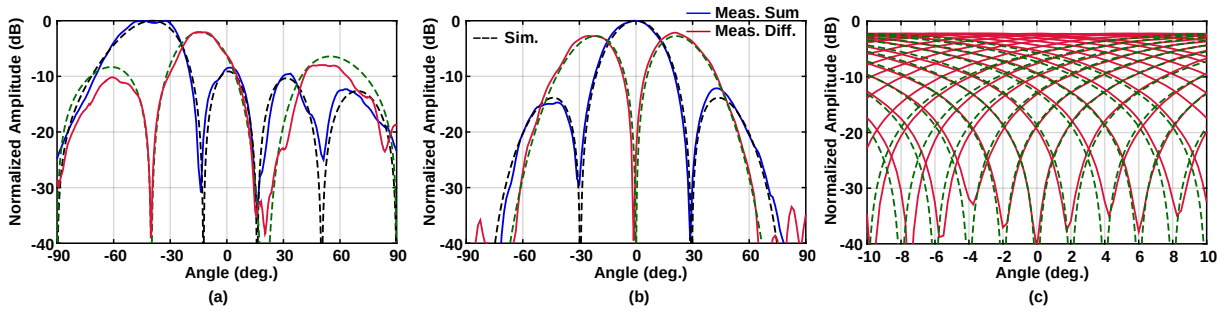

Figure 4.17: Measured 4x4-quadrant patterns with Quad-BIST calibration in RX-mode at 30 GHz: (a) sum and difference patterns scanned to -40° (b) sum and difference patterns at broadside and (c) fine-scanned null of difference pattern.

4.5.2 $4 \times [8 \times 8]$ Array Results

Similar procedure is applied to the Quad(A) of the 4x8x8 array (shown in Fig. 4.11) to test the performance in case of larger and consequently weaker antenna couplings. Leakage cancellation is also adapted to synthesize quiet environment at 27 GHz as illustrated in Fig. 4.18a. Although, only phase-tuned cancellers were employed, element gain is not tuned and is set to min-gain state, the leakage could be suppressed by 18-30 dB for the different TX-probes as illustrated in Fig. 4.18c. It is worth mentioning that, the cancellation instantaneous 3 dB-BW is generally narrow ($\approx$ 100 MHz), but it can be tuned for any frequency. Attaining higher instantaneous cancellation bandwidths is potentially possible with the use of multi-element cancellation strategy, however this requires a non-trivial synthesis procedure and is not the primary interest of this work.

For the 8x8 array, an near-field SLR better than 44 dB could be attained for every channel

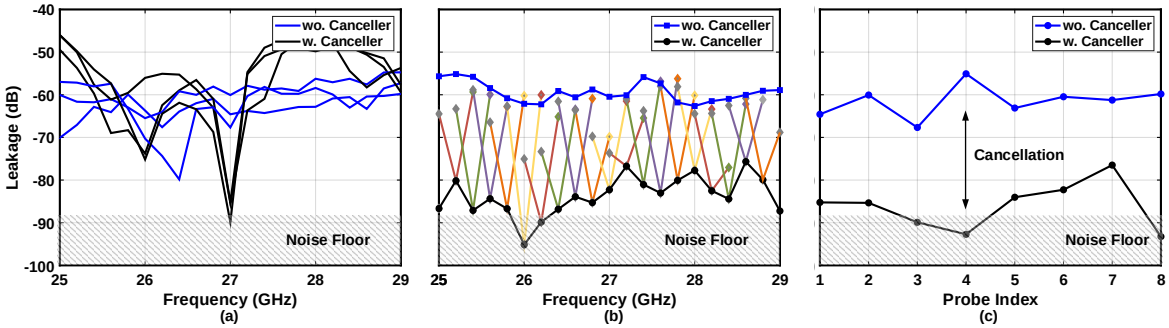

Figure 4.18: Measured 8x8-Quad-A in RX-mode: (a) Quad-B TX- leakage before and after using tuned cancellers at 27 GHz for TX-probes (#2,3,4), (b) Quad-B leakage level from TX-probe#4 before and after using tuned leakage cancellers at different frequencies and (c) Quad-B leakage-levels from different probes before and after using a phase-tuned leakage canceller at 27 GHz.

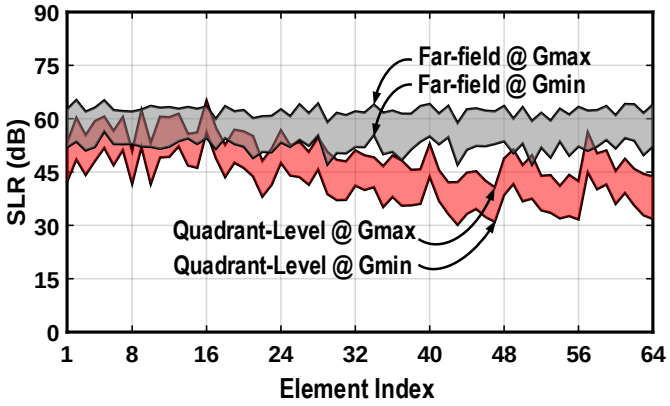

Figure 4.19: Measured signal-to-leakage-ratio at every element in Quad(A) of the 4x[8x8] array at 27 GHz in far-field and quadrant-level characterization.

at the maximum gain state which is better then 30 dB for the lowest gain state as observed in Fig. 4.19. Different from near-field SLR which can vary based on the element position and coupling strength, the far-field SLR has less variation for the different channels and remains above 50 dB for all elements. Fig. 4.20 represent the SNCSs using far-field and near-field quadrant-level testing for the 64-channels over all their 64-phase states and 39-gain states. The deviation errors are found to be mostly below 0.3 dB/ 3°. In few channels, the peak error at the lowest gains states could reach a maximum of 0.7 dB/ 5 deg. The error distributions are illustrated showing that the majority of errors are clustered around zero with a standard deviations of 0.09 dB/0.61 deg. for

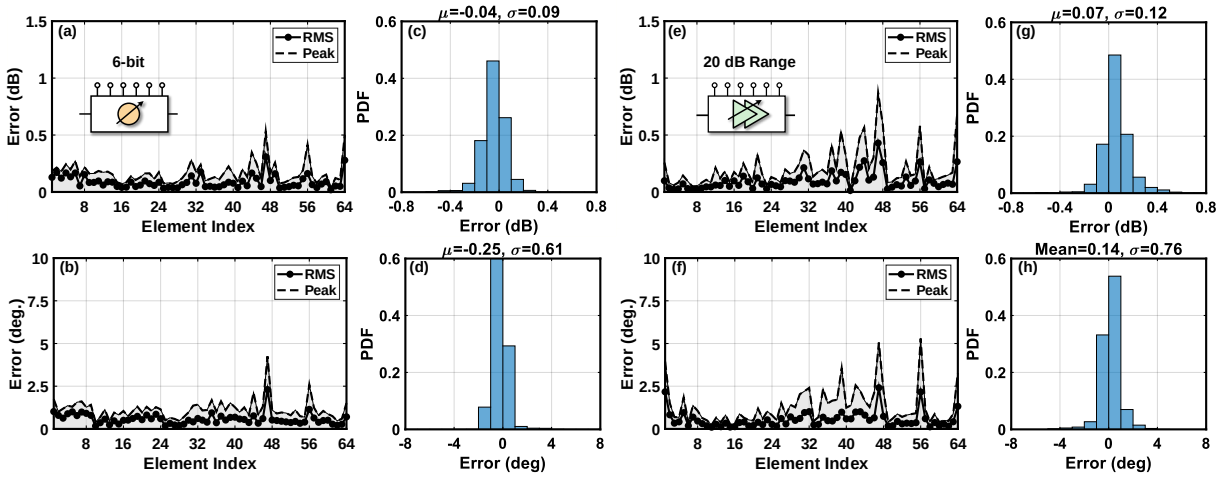

Figure 4.20: Measured 8x8-Quad-A channels characterization errors between BIST and far-field at 27 GHz: (a-b) phase-states peak and rms errors per channel, (c-d) phase-states amplitude/phase error distribution, (e-f) gain-states peak and rms errors per channel, (g-h) gain-states amplitude/phase error distribution.

phase states and 0.07 dB/0.8 deg. for VGA states. The channel are also compared to far-field and deviation errors are evaluated in Fig.4.21. The errors are found to be mostly ± 1 dB/ ± 10 with an rms error value of 0.7 dB/5.5°. Most of the peak errors are observed to happen at the edge element locations, mainly for element index $56-64$, which are likely induced by coupling symmetry perturbations associated with edge-induced coupling asymmetries due to the absence of dummies in this array. The ability to detect channel failures is also tested. This is done by purposely dropping elements by 10 dB and running the extraction routine again and comparing versus far-field measurements. The detected distributions for different dropped element location are illustrated in Fig. 4.21(g-i), in all cases the element can be easily detected and the rms error accuracy does not change much.

The pattern setting accuracy of the 8x8 array is tested using the data collected from far-field and quadrant-level calibration. The measured pattern under scanned condition with uniform illumination and an 8-dB raised cosine taper are compared in Fig. 4.22. It can be observed than for uniform illumination, the pattern are near-ideal for all scan conditions with a beam width of 12.8° and side lobes of -13 dB at broadside. Under taper conditions, the side lobe levels are dropped to -23 dB at broadside and -20 dB with scan. The results are a bit higher than

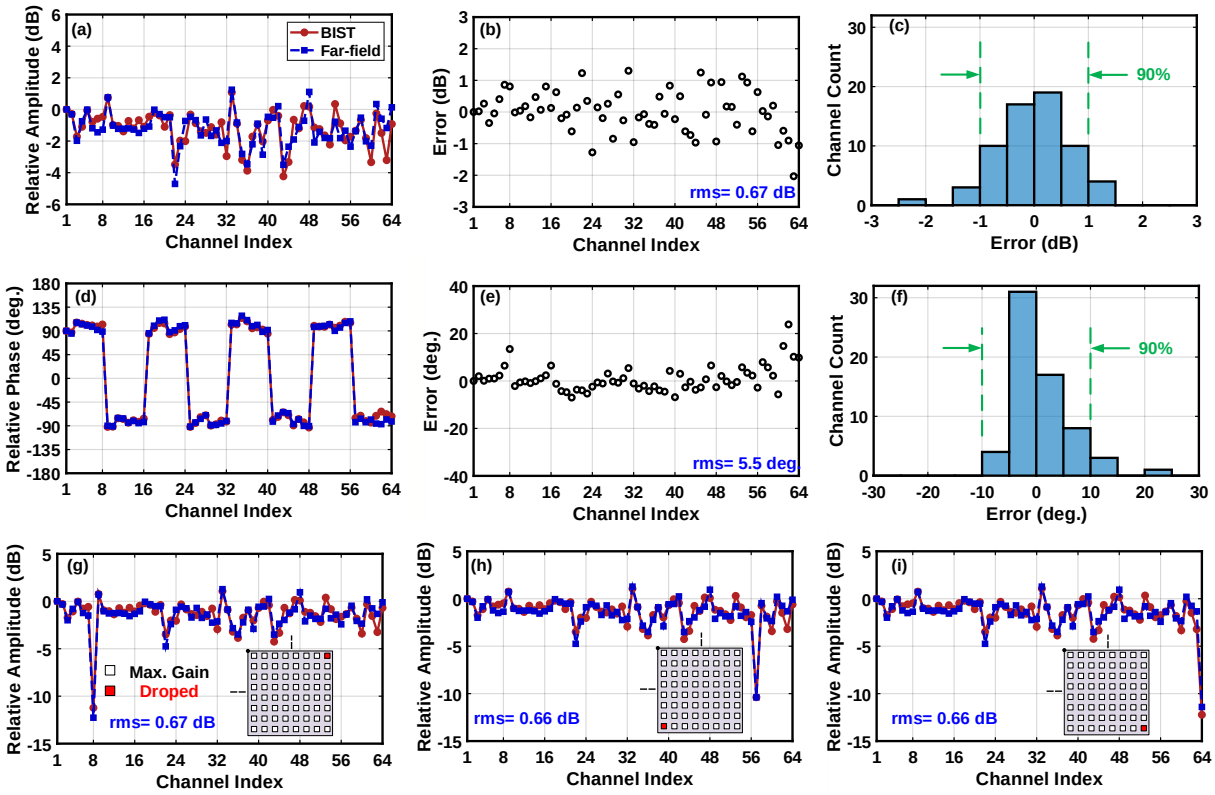

Figure 4.21: Measured 8x8-Quad-A relative channel gains/phases in zeroth-state and RX-mode at 27 GHz: (a,d) BIST and far-field amplitudes and phases, (b,e) BIST amplitude/phase errors w.r.t. far-field, (c,f) amplitude/phase error distributions and (g,h,i) in presence of different low-gain malfunctioning elements.

theoretical ones for both far-field and quadrant-level self-calibration. The similarity of the far-field and near-field patterns suggest that part of the deterioration is due to the resolution limitation of the array phases/gains. Fig. 4.23 illustrates the measured patterns based on Quadrant-level self-calibration data with uniform, 6-dB and 10-dB raised cosine tapers. The results show that the side lobes can be dropped even down to -26 dB at broadside and -23 dB over scan, however the pattern control starts to noticeably worsen at this high taper level. Mono-pulse patterns are shown in Fig. 4.24 based on the near-field calibration, the observed mono-pulse null depths are generally better than -33 dB. It is worth mentioning that detecting null depths is generally challenging as it requires very fine angular sampling in order to capture the exact peak null value. If the peak null does not exactly align with a sample, the null-depth will be under-estimated. In this experiment, the sampling is done with 0.25° step.

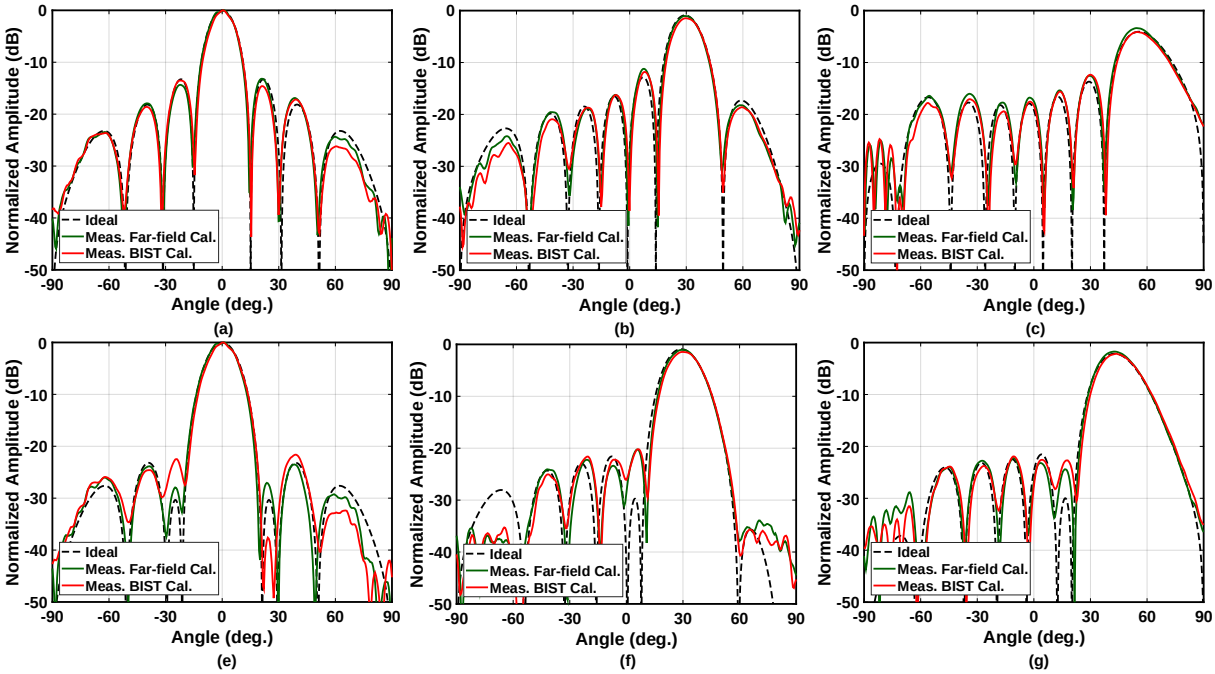

Figure 4.22: Measured 8x8-Quad-A patterns with BIST and far-field calibrations in RX-mode at 27 GHz, under uniform-illumination scanned to: (a) 0°, (b) 30°, and (c) 60°, and under 8-dB raised cosine taper-illumination scanned to: (e) 0°, (f) 30°, and (g) 60° all in the azimuth-plane.

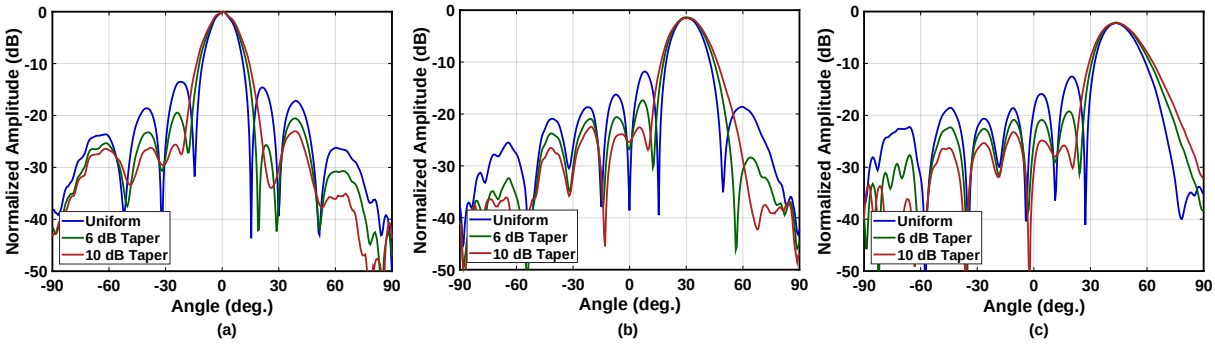

Figure 4.23: Measured 8x8-Quad-A patterns with BIST and far-field calibrations in RX-mode at 27 GHz:, scanned to: (a) 0°, (b) 30°, and (c) 45° in the azimuth-plane with increasing taper (uniform, 6-dB raised cosine and 10-dB raised cosine).

Fig. 4.25 represents the measured side lobe level versus scan angle for ideal, far-field calibrated array, and quadrant-level calibrated array. It is observed the performance is nearly identical for uniform illumination and within 1.5 dB for the tapered case at the different scan angles. Note that, due to the pattern broadening with taper, the side lobe levels are limited by the entrance of a grating lobes at $\pm 60^{\circ}$ scans which agrees with theoretical expectations. The

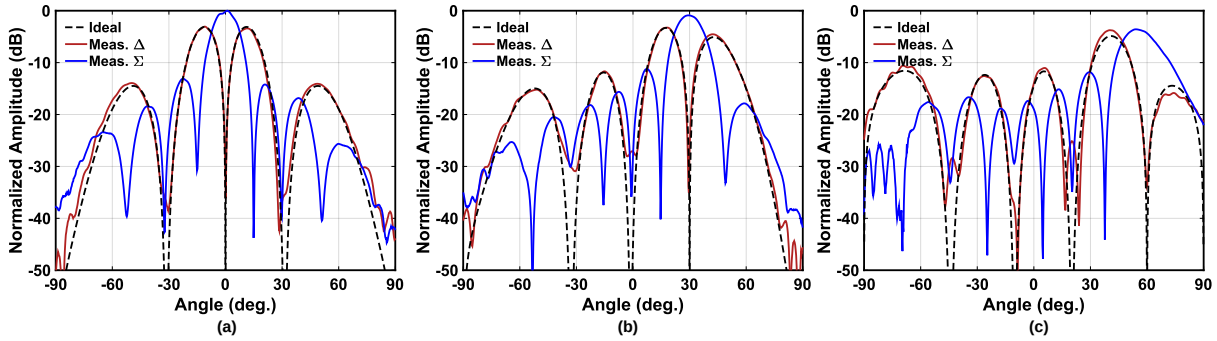

Figure 4.24: Measured 8x8-Quad-A patterns mono-pulse radiation patterns based on quadrant-level calibration at 27 GHz, scanned to: (a) 0°, (b) 30°, and (c) 45° in the azimuth-plane.

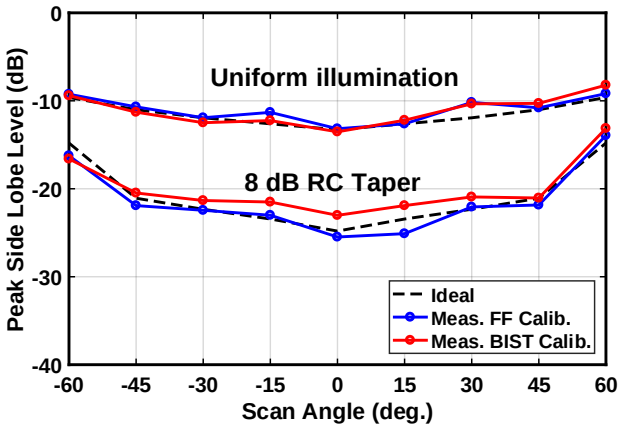

Figure 4.25: Measured peaks side-lobe levels versus scan angle at 27 GHz using far-field and BIST calibrations.

null-rejection accuracy and null-position errors are also evaluated for the different mono-pulse null scan angles in Fig. 4.26. The measurements indicate that the null depth is at least 32 dB over the different scan angles, also the nulls can be positioned with an accuracy of $\pm 0.5^{\circ}$.

4.6 Discussion

A summary of the performance is given in Table 4.2, as can be seen, the SNCS can be determined with very high accuracy. However, the over-all errors is dominated by the CCR values. These are likely arising from errors in the ideally-symmetric antenna-couplings. In practical implementations symmetry perturbation may exits due element location close to an edge or due to

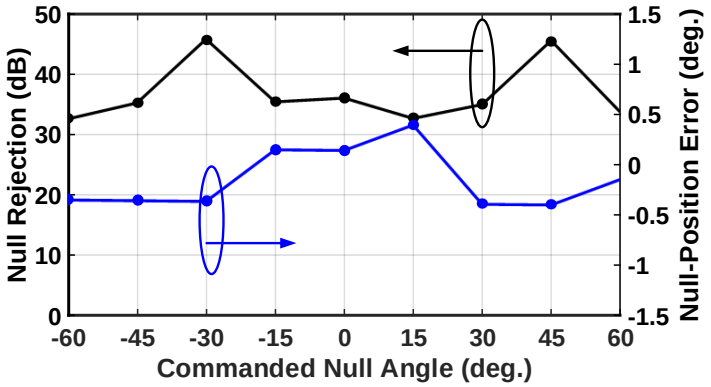

Figure 4.26: Measured mono-pulse null depth and null-positioning accuracy using BIST calibration.

Table 4.2: Summary of QL-BIST Performance

Metric	4x4	8x8
Frequency (GHz)	30	27
Channel Self-Normalized RMSE	0.2 dB/2°	0.4 dB/3°
Channel-to-Ref.-Channel RMSE	0.78 dB/7.5°	0.67 dB/5.5°
Total RMSE	0.81 dB/7.6°	0.81 dB/6.3°
Signal-to-Noise-and-Leakage Ratio [dB]	> 40	> 30
Side-Lobes (Uniform) [dB]	-12.5	-13
Side-Lobes (Tapered) [dB]	-	-26
Mono-pulse Null Depth [dB]	< -26	< -32
Mono-pulse Null accuracy [deg.]	$< 1°$	$< 0.5°$

ground plane imperfections (small routing slots), as well as fabrication tolerances. Since to extract the ratio of channel (m,n) with respect to channel (1,1) needs passing through (m-1) vertical hops followed by (n-1) horizontal hops, small error in each hope can propagate. To investigate this effect, the rms measurement error is evaluated as the array size is grown away from the reference element (1,1) within the 8x8 array quadrant in Fig.4.27. It is observed that elements very close the reference element suffer from very low error <0.3 dB/3 deg, however as the array size is grown, the error increases in a logarithmic fashion due to error accumulation. It is also observed that at the very last row the phase error increases abruptly from 3 to 5.5 deg. rms which indicates an edge asymmetry issue. This particular jump is expected to be resolvable with the addition of dummy elements to terminate the aperture.

A concern about calibration accuracy of testing each single element at a time is that

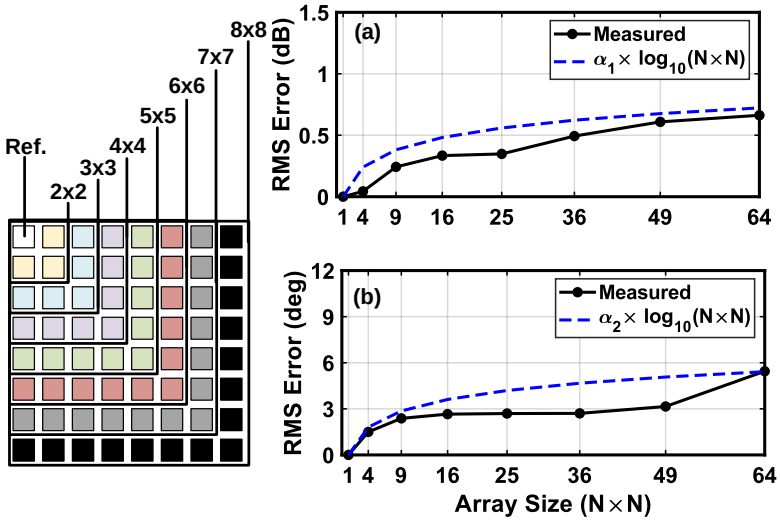

Figure 4.27: Channel-offsets error growth versus array size: (a) amplitude and (b) phase.

this might not reflect the actual channel properties when the full-array is activated. It is well known that the input impedance of antenna within an array will depend on the excitation of the surrounding elements [45, 54]. This very true for ultra-wide band tightly coupled array designs such PUMAs and TCDA where a large portion of the input impedance comes from the mutual-coupling coefficients [55–57]. In conventional lightly coupled designs ($C_{max} < -20$ dB), the impedance change is less pronounced that it does not affect pattern synthesized down to the -26 dB level as evident in our experiments. To further investigate the issue, we measured the chip-level, four channels simultaneously active, in far-field and compared it with the values extracted from the near-field (one-channel at a time) that are mathematically combined to yield the expected chip level data. It is found that the coefficients on the chip level agree very well with an error of 0.56 dB and 4.5 deg. which suggest that one at a time measurements can be accurate even when all channels are active. Nevertheless, it is good to investigate means of measuring the array while several elements are active and extract their properties in in-situ from the near-field couplings.

In regards to the time-frame of quadrant-level calibration, a measurement count of the traversal procedure for an array of N-elements is computed as follows. To be able to determine

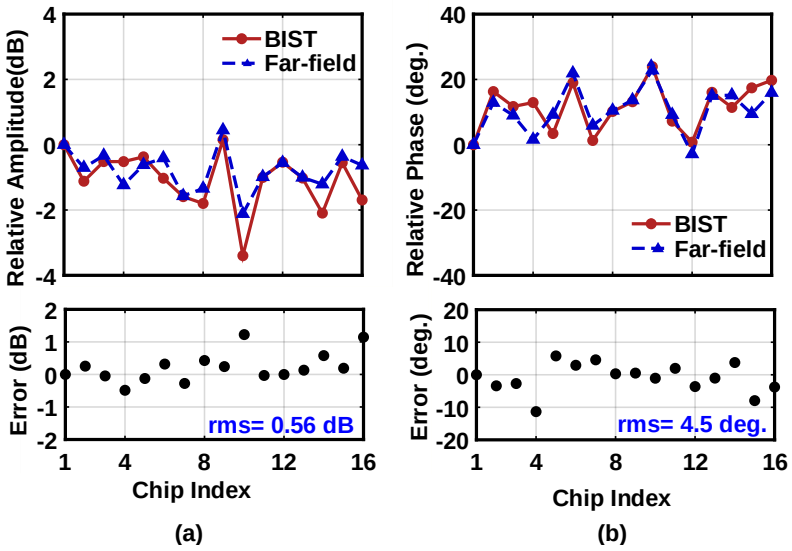

Figure 4.28: Measured chip-level offsets in far-field and based on Quad-BIST channel estimates at 27 GHz: (a) relative amplitude and (b) relative phases.

the CRC ratios, multiple coupling measurements are needed from different TX-probe for each element under test. The steps of obtaining all the CRC ratio for a general array with $M = N \times N$ elements is illustrated in Fig. 4.29. The first main step is to traverse the columns. In this step, Fig 4.29a, the nearest TX-probe in columns 1 to N in the neighboring Quad is activated. Then for each TX-probe, the RX elements in the same column as well as the column just before and just after in the Quad-under-test are activated one at a time and a transmission measurement is carried out. This results in a number of measurements using the TX-probe in column k of $N_c(k) = 3N$. This is true for all columns except the first and the last which only need $N_c(k = 1, N) = 2N$ measurements. The total number of measurements to traverse all column probes is then $N_c^{tot} = 2N + (N-2)3N + 2N = 3N^2 - 2N$.

The second main step is to traverse across the rows of the reference column as illustrated in Fig 4.29b. This requires $N_r^{tot} = 2 + (N-2)3 + 2 = 3N - 2$ transmission measurements. Therefore the total number of transmission measurements needed to collapse the array into one reference element is $N^{tot} = N_c^{tot} + N_r^{tot} = 3N^2 + N - 2 = 3M + \sqrt{M} - 2$. This result shows that the number of traversal measurements has a predominant linear growth with the total number of elements

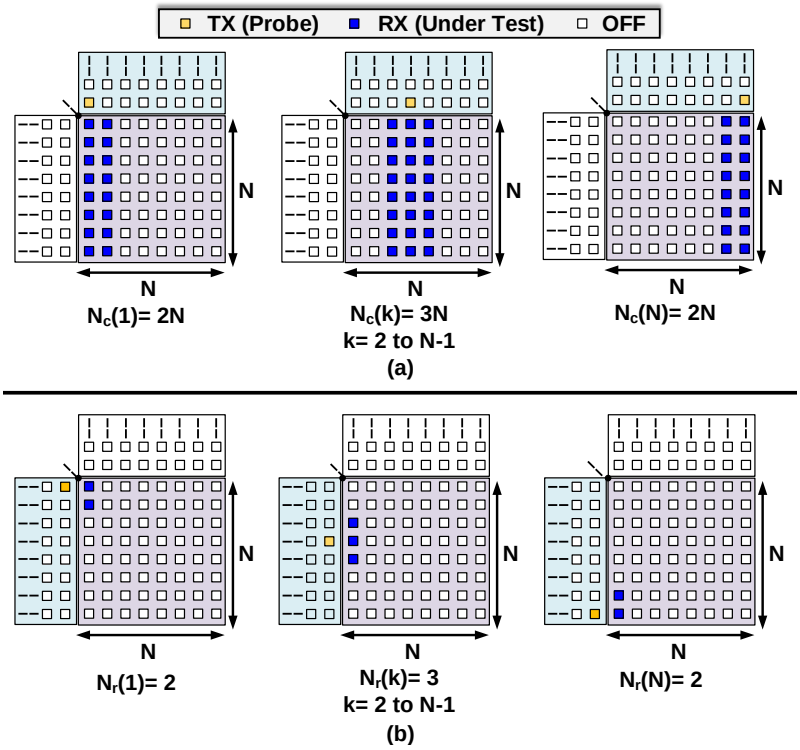

Figure 4.29: Number of measurements needed for QL-Traversal scheme fo a general N×N array-quadrant: (a) traversing column and (b) traversing rows of the reference column.

$N^{tot} \approx 3M$.

Compared to traditional far-field that requires $N_{meas}^{FF} = N$ measurements, the quadrant calibration approach requires $N_{meas}^{QL} = 3 \times N + \sqrt{N} - 2$ measurements to extract the relative channel offsets. There is also an additional overhead time if leakage canceller are needed but this is generally negligible relative to the array characterization itself in the order of $C_0\sqrt{N}$. For an average measurement integration time of $\tau = 100$ μsec, the quadrant-level traversal requires $50\tau = 5$ msec and $198\tau = 19.9$ msec for a 4x4 and 8x8 quadrant size, respectively. In comparison, the far-field requires $16\tau = 1.6$ msec and $64\tau = 6.4$ msec, respectively. To characterize all channel states (K-states per channel), the number of measurements needed is $N \times K$ and is the same for far-field or near-field.

4.7 Conclusion

This work presented an in-situ self-test and self-calibration method for single-polarized multi-beam 5G mmWave TRX MIMO phased arrays based on quadrant-level antenna couplings (QL-BIST). The method relies on antenna-mutual-coupling between neighboring phased array MIMO quadrants to perform channel testing and calibration. Different impairments and limitation such noise, leakage are investigated in detail. Performance was experimentally verified using 4x4x4 and 4x8x8 quadrant-arrays showing good calibration accuracy with error below 0.4 dB/3° for channel testing and below 0.7 dB/7° for relative offset estimation. QL-BIST based calibration demonstrated low-side lobe array operation down to -23 dB over scan and null pointing accuracy $\pm 0.5°$ over scan. QL-BIST offers several attractive feature compact and all-electronic, requires no moving parts or a far-field range, and can be applied for initial calibration as well as for re-calibration in the field (as a result of aging, environmental changes, etc.), and is well suited for 5G MIMO base-station systems. Future work include, implementation of complete built-in QL self-calibration online-system and extensions to dual-polarized 5G based phased array.

4.8 Acknowledgement

This work was supported by Intel. Additional support was also provided by Keysight and JUMP program under DARPA/SRC DSSP funding. The authors thank Keysight for assembly of the phased-array with BIST capabilities.

Chapter 4, in part, is a reprint of the material as it appears in IEEE MTTS Int. Microw. Symp. (IMS), 2019. A. Nafe, K. Kibaroglu, M. Sayginer, and G. M. Rebeiz. The dissertation author was the primary investigator and author of this paper.

Chapter 4 is also mostly a reprint of the material as submitted to IEEE Transactions on Microwave Theory and Techniques, 2020. A. Nafe, Z. Zhang, Y. Yin, M. Sayginer, K. Kibaroglu, and G. M. Rebeiz. The dissertation author was the primary investigator and author of this paper.

Chapter 5

In-Situ Self-Test and Self-Calibration of Dual-Polarized 5G TRX Phased Arrays Leveraging Orthogonal-Polarization Antenna Couplings

In this chapter, an in-situ self-test and self-calibration technique for 5G dual-polarized dual-beam TRX phased-arrays is presented. The procedure, labeled dual-polarized built-in self-test (DP-BIST), exploits the mutual coupling between different antennas of orthogonally polarized beams sharing the same aperture to enable relative channel offset extraction, channel gain/phase characterization and failure detection for the channels of each beam. DP-BIST was applied to a 16-element dual-polarized dual-beam linear phased-array at 29 GHz and predicted the relative channel states (gain, phase) with rms errors $\leq$0.2 dB /2.5° and the relative channel offsets with rms errors of 0.8 dB /7°. DP-BIST is all-electronic, and can be done using a single aperture without any assistance from neighboring arrays. It can be used for initial calibration as well as for re-calibration in the field, and is well suited for 5G polarization-based multiple-input

multiple output (MIMO) systems.

5.1 Introduction

Fifth-generation (5G) mobile networks seek to provide high-speed Gbps data links to mobile users at mm-Wave frequency bands around 28, 39 and 60 GHz. At these frequencies, phased arrays are used to provide directional steerable beams to compensate for the increased free-space path loss [1, 6, 29]. To further increase the communication-link capacity, polarization-based multiple-input multiple-output phased array systems are proposed in the 5G standard (Fig. 5.1b). Such a phased-array system, utilizes two beams that are orthogonally-polarized and can carry different data streams [10, 14, 31].

A cost-driving point for mm-Wave phased arrays is testing and calibration. For proper array operation, each channel needs to be tested and the relative channel offsets need to be determined and corrected to be able to set the radiated beam properties (pointing angle, side-lobe level, etc...). This process is not only required at production time (initial-calibration) but also, it needs to be done periodically to account for element drift due to environmental effects. Conventional array testing and calibration are carried out using a far-field range or a near-field scanner. Both methods suffer from requiring set-ups that cannot be used once the array is deployed.

Therefore, it is of interest to develop in-situ calibration and testing methods that can be periodically applied for fielded arrays. In-situ calibration methods on the chip level are possible, but they can only detect the electronic chip performance and not the full channel response up to the antenna air-interface.

An important goal is to realize in-situ calibration that captures the full array-response up to the antenna air-interface. This kind of calibration could be achieved with the use of antenna mutual coupling and was originally introduced by [4, 51]. In these papers, the arrays are single

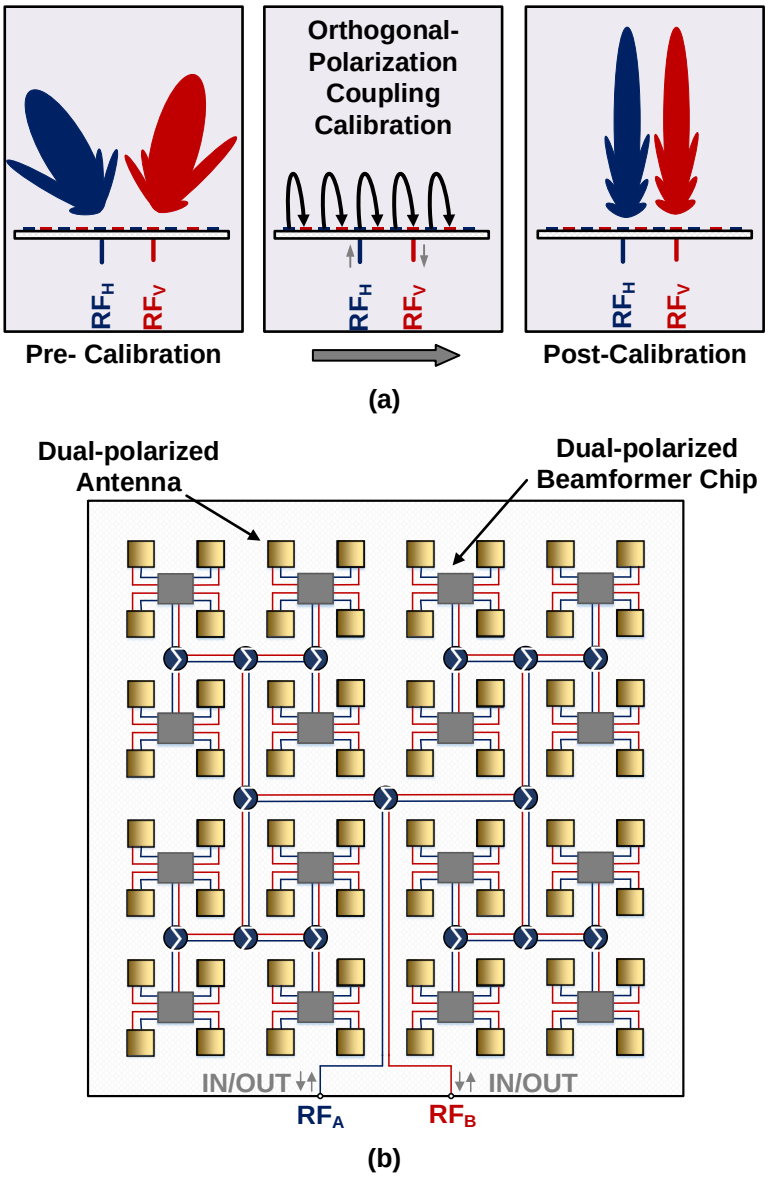

Figure 5.1: (a) Polarization-to-polarization phased-array antenna coupling and calibration concept and (b) 5G-TRX dual-polarized dual-beam phased-array architecture.

polarized and have the capability of transmitting on one element and receiving at all of its direct neighbors, a feature which is not available in mm-Wave 5G phased arrays. Also in [44], mutual coupling between antennas in single-polarized 5G arrays was utilized to perform in-situ self-calibration.

In this work, the problem of in-situ calibration for 5G dual-polarized dual-beam phased

array is investigated. It is shown that a dual-beam dual-polarized 5G TRX phased array can self-calibrate and self-test using polarization-to-polarization antenna mutual coupling on the same aperture (Fig. 5.1a). This is quite advantageous as the array does not require any assistance from neighboring arrays and can be done periodically in the field.

5.2 Dual-Polarized Antenna Coupling and Calibration Methodology

5.2.1 Dual-Polarized Microstrip Antenna Coupling Symmetries:

Fig. 5.2 presents the simulated coupling between two neighboring elements in a 16-element microstrip antenna array spaced at 0.5λ along the x-axis. Two configurations are considered. The first configuration has the antenna polarization aligned to the array-line axis (i.e x-axis) and the second configuration has the antenna polarizations inclined by $\pm 45^{\circ}$ to the x-axis. In the first configuration, Fig. 5.2(a,b), the coupling between the two orthogonal polarization feeds of a given antenna is equal for the neighboring elements ($C_{k,k} = C_{k+1,k+1}$) but the coupling between the cross-polarized feeds on neighboring antennas is not the same ($C_{k,k+1} \neq C_{k+1,k}$). In the second configuration, Fig. 5.2(c,d), both same antenna and neighboring antenna cross-polarized couplings are equal ($C_{k,k} = C_{k+1,k+1}$ and $C_{k,k+1} = C_{k+1,k}$). This property will be used to enable self-calibration based on orthogonal-polarization coupling symmetries.

5.2.2 Calibration Coefficient Extraction:

Consider an N-element linear array of dual-polarized antennas with 45°-inclined polarizations as shown in Fig. 5.3a. Each polarization has a separate beam-forming network and input/output ports. Therefore, the situation is equivalent to having two separate arrays sharing the same aperture. The 45°-polarization elements constitute one array referred to as array (A) with

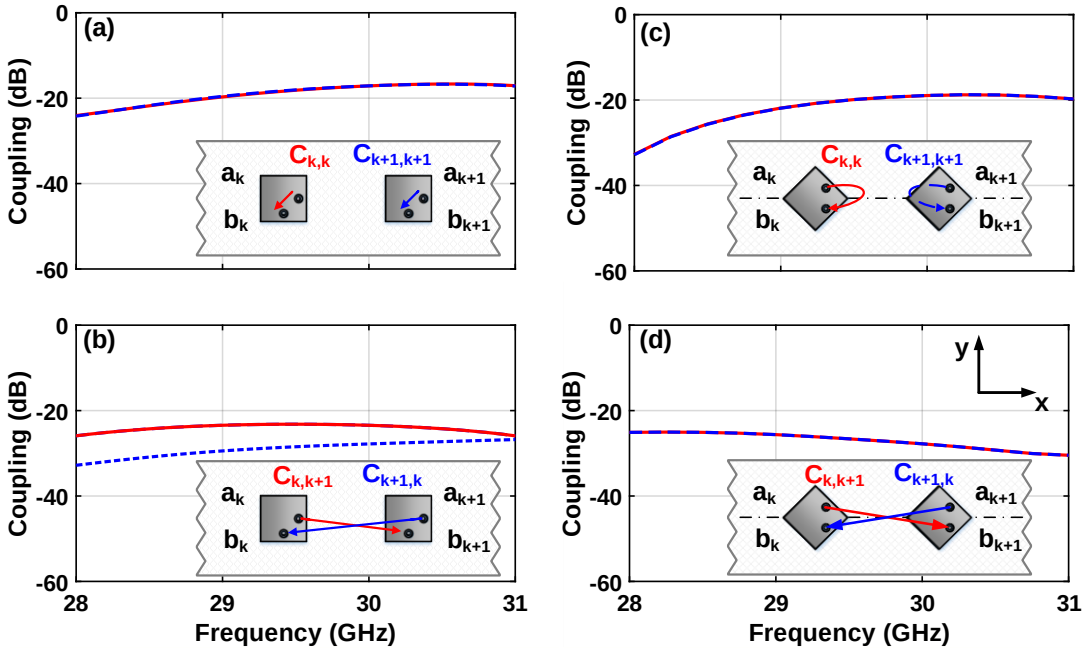

Figure 5.2: Simulated pol.-to-pol. antenna coupling in a dual-polarized dual-beam microstrip patch array: (a,b) standard orientation and (c,d) 45-deg. rotated orientation.

input/output port labeled $\mathrm{RF_A}$, while the $-45°$-polarization elements constitute another array referred to as array (B) with an input/output port labeled $\mathrm{RF_B}$. Each polarization has transmit and receive capabilities so that one can transmit using one polarization and receive using the other polarization through the RF ports A and B, respectively.

Let the channel transfer fucntion of element number k be labeled as a_k for $\mathrm{RF_A}$ channel in the TX mode and as b_k for $\mathrm{RF_B}$ channel in the RX mode. The channel transfer function is the overall response from the array RF co-axial ports to the antenna and includes the Wilkinson feed network, electronic channel, transmission-lines and antenna response. The calibration coefficients are denoted by κ_k which refer to the ratio of channel b_k to the reference channel, chosen as b_1. The intermediate calibration coefficients (channel b_k with respect to channel b_m) are referred to as $\kappa_k^m = b_k/b_m$.

The dual-polarized BIST traversal procedure is shown in Fig. 5.3b. The signal is injected into the $\mathrm{RF_A}$ port and picked up at the $\mathrm{RF_B}$ port. This is done as a typical $S_{2,1}$ measurement using a VNA. The process starts at the first two elements where a set of four $S_{2,1}$ measurements

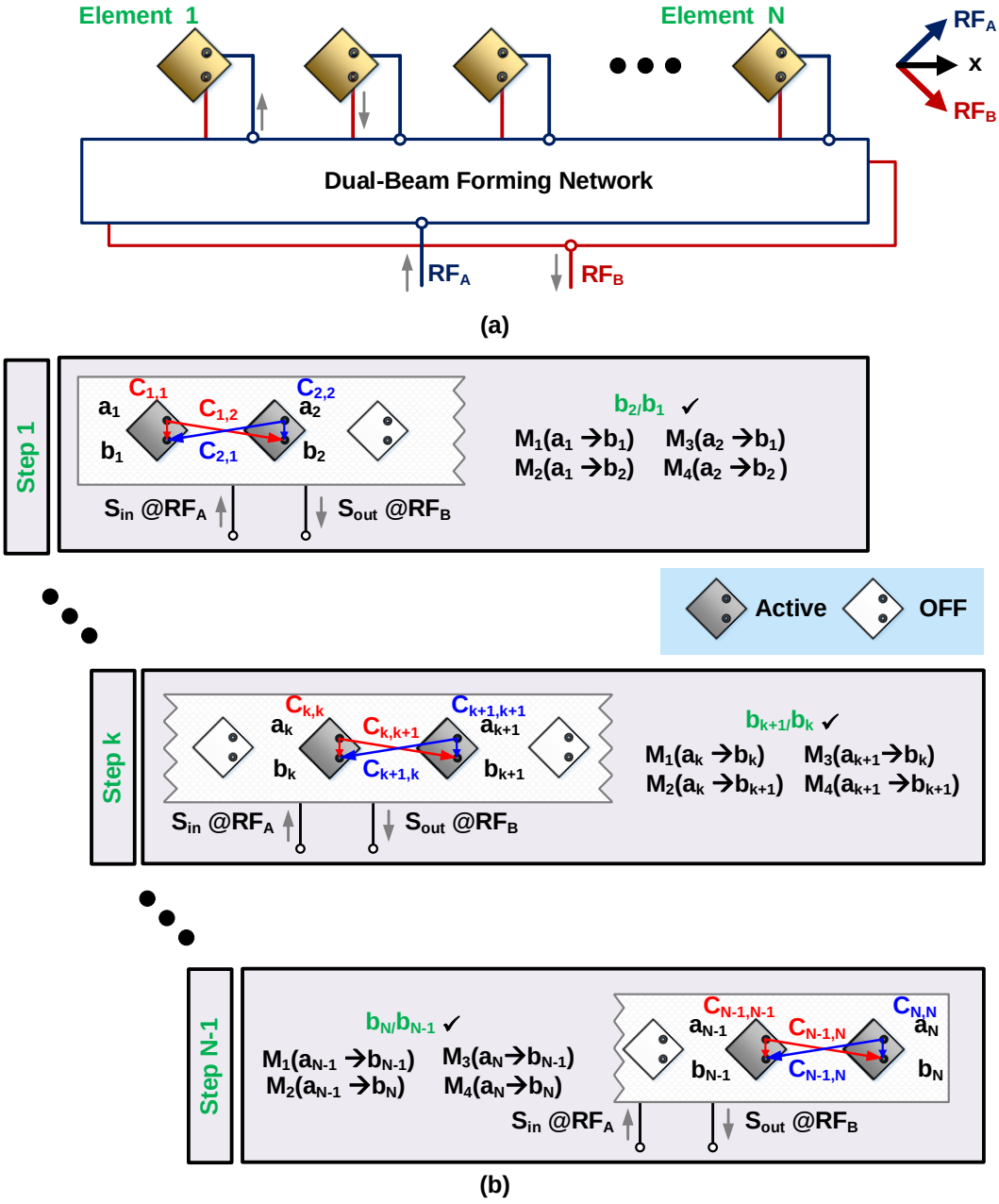

Figure 5.3: (a) N-element dual-polarized dual-beam linear phased array and (b) DP-BIST traversal procedure.

is conducted. For each measurement, only one TX channel and one RX channel are active with all the remaining channels turned OFF. For the first two elements, these four measurements are

expressed as:

$$M_1(a_1 \rightarrow b_1) = \frac{S_{out}}{S_{in}} = a_1 C_{1,1} b_1 \tag{5.1}$$

$$M_2(a_1 \rightarrow b_2) = \frac{S_{out}}{S_{in}} = a_1 C_{1,2} b_2 \tag{5.2}$$

$$M_3(a_2 \rightarrow b_1) = \frac{S_{out}}{S_{in}} = a_2 C_{2,1} b_1 \tag{5.3}$$

$$M_4(a_2 \rightarrow b_2) = \frac{S_{out}}{S_{in}} = a_2 C_{2,2} b_2 \tag{5.4}$$

Since $C_{1,2} = C_{2,1}$ and $C_{2,2} = C_{1,1}$ for the 45° inclined configuration, the unknown coupling coefficients can be cancelled out by taking measurement ratios. The calibration coefficient for channel b_2 is then obtained as:

$$\kappa_2 = \sqrt{\frac{M_2}{M_1} \times \frac{M_4}{M_3}} = \sqrt{\frac{a_1 C_{1,2} b_2}{a_1 C_{1,1} b_1} \times \frac{a_2 C_{2,2} b_2}{a_2 C_{2,1} b_1}} = \frac{b_2}{b_1} \tag{5.5}$$

This step is repeated iteratively to extract the ratio of all pairs of neighboring channels $\kappa_k^{k-1} = b_k / b_{k-1}$. After this is done, the calibration coefficients with respect to the reference channel b_1 can be calculated. For the mth-channel ($m > 1$), this can be expressed as:

$$\kappa_m = \prod_{j=2}^{j=m} \kappa_j^{j-1} = \frac{b_k}{b_1} \tag{5.6}$$

and with this step, the channel ratio of all elements with respect to a reference element are found and the calibration coefficients extraction is completed. Then, any amplitude and phase offset can be corrected by modifying the amplitude and phase setting of the individual channels.

5.3 16-Element Dual-Polarized 5G Phased-Array Implementation

To test the DP-BIST calibration method, a 16-element dual-polarized dual-beam phased array was built (Fig. 5.4). The array is implemented in a low-cost multi-layer printed circuit board and using 2×2 single-beam 28 GHz TRX SiGe beamformer chips [52]. Two 1:4 Wilkinson beamforming networks are used to feed the $+45^\circ$ (RF_A) and the -45° (RF_B) polarized beams. The antenna spacing is 5.1 mm ($\lambda_0/2$ at 29.5 GHz) to scan $\geq \pm 50^\circ$ without grating lobes. A pair of terminated dummy antennas are added on each side of the array to reduce edge effects and minimize coupling-symmetry perturbation. Also, additional passive probe antennas are included (probes 1-4) that are connected to 2.9 mm co-axial connectors separate from the arrays connectors. Probes (1,2) are polarized along the horizontal direction (x-axis) and are placed at either end of the array-line. By symmetry the coupling from probe 1 or 2 to any given array antenna's -45° and $+45^\circ$ feeds is the same, this enables knowing and calibrating any imbalance between the two polarizations if needed (for instance to provide circular-polarization operation using signals from both arrays A and B). Probes (3,4) are polarized vertically (along the y-axis) and are placed so as to couple equally to antennas pair (1,2) and (15,16) respectively. They ensure that the $0^\circ/180^\circ$ phase solutions associated with the square root operation in eq. (5.5) can be easily distinguished.

5.4 Measurements

The arrays are characterized using a standard far-field method at a distance of 1.9 m (see Fig. 5.5). This is done by turning ON the array elements one-by-one and measuring the transmission coefficients to the horn in every gain and phase state. In a second step, coupling measurements between the different channels are performed by turning ON a pair of channels (one in each array) in TX and RX modes and measuring the coupling coefficients as described in

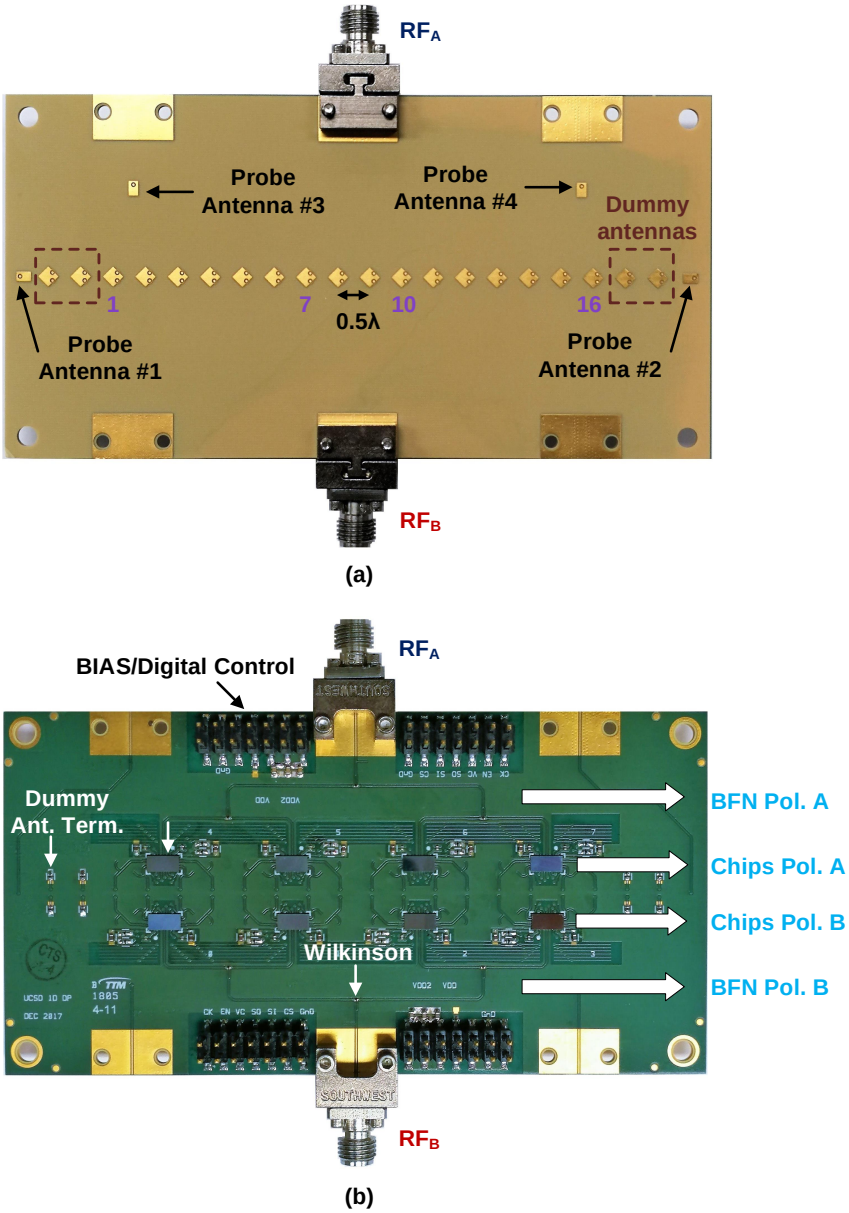

Figure 5.4: 16-element self-calibrating dual-polarized dual-beam 5G TRX phased array: (a) antennas side and (b) chip side.

the DP-BIST stepping procedure.

Fig. 5.6 (a,b,c) presents the measured array port-to-port coupling between different Tx/Rx elements. In each coupling measurement, only a pair of elements is turned ON, shown here for the case of transmitting using array A and receiving using array B. For each transmitting

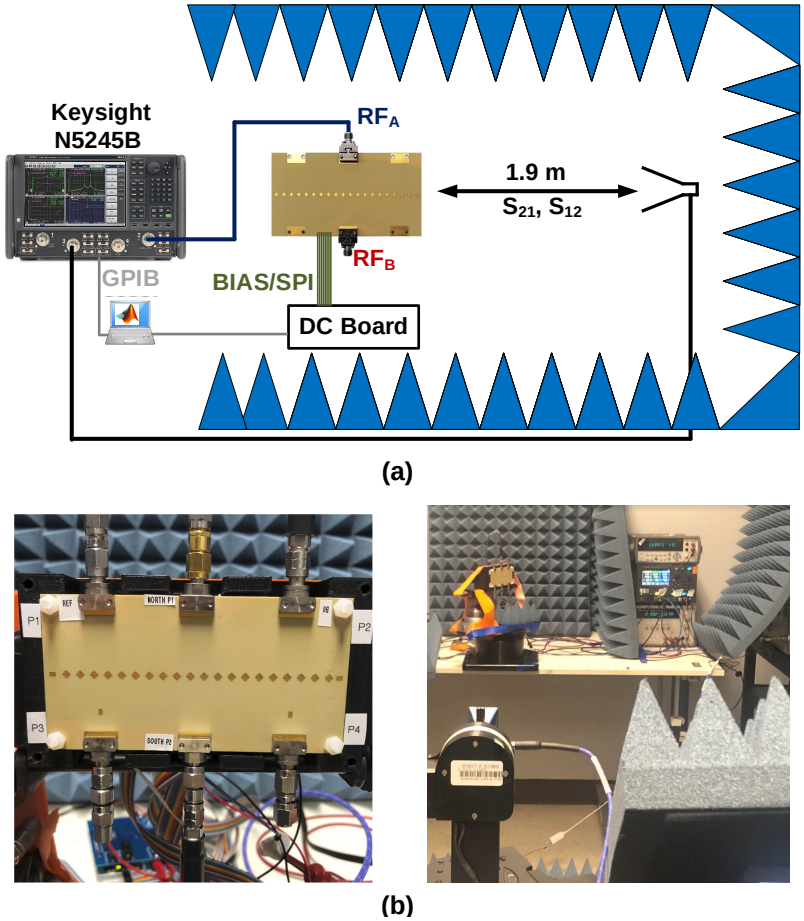

Figure 5.5: Phased array measurement set-up: (a) block-diagram and (b) photo.

antenna, the signal is recorded at three receive elements; The one with same index through $C_{k,k}$, the one directly after through $C_{k,k}$, and the one directly before $C_{k,k-1}$. The process is done for all transmit elements $k = [1-16]$ with the first and last elements involved in only two measurements due to their edge location. It can be observed that the frequency response profile for the same antenna coupling $C_{k,k}$ is very similar for all elements, and the signal level is much higher than the OFF-leakage signal level[1] with a worst case signal to leakage and noise ratio (SLNR) ≥ 30 dB over a wide frequency range from 34-35 GHz as shown in Fig. 5.6 (a). The coupling through $C_{k,k+1}$ and $C_{k,k-1}$ also varies in frequency response for all elements. The coupling peak is about

[1]OFF-leakage is the signal picked up at the receive array output when the TX element is ON and all RX-elements are OFF or vice versa. It represents the coupling happening un-intentionally through antenna to beamformer coupling or antenna to connector coupling or even leakage through the OFF-electronic channels.

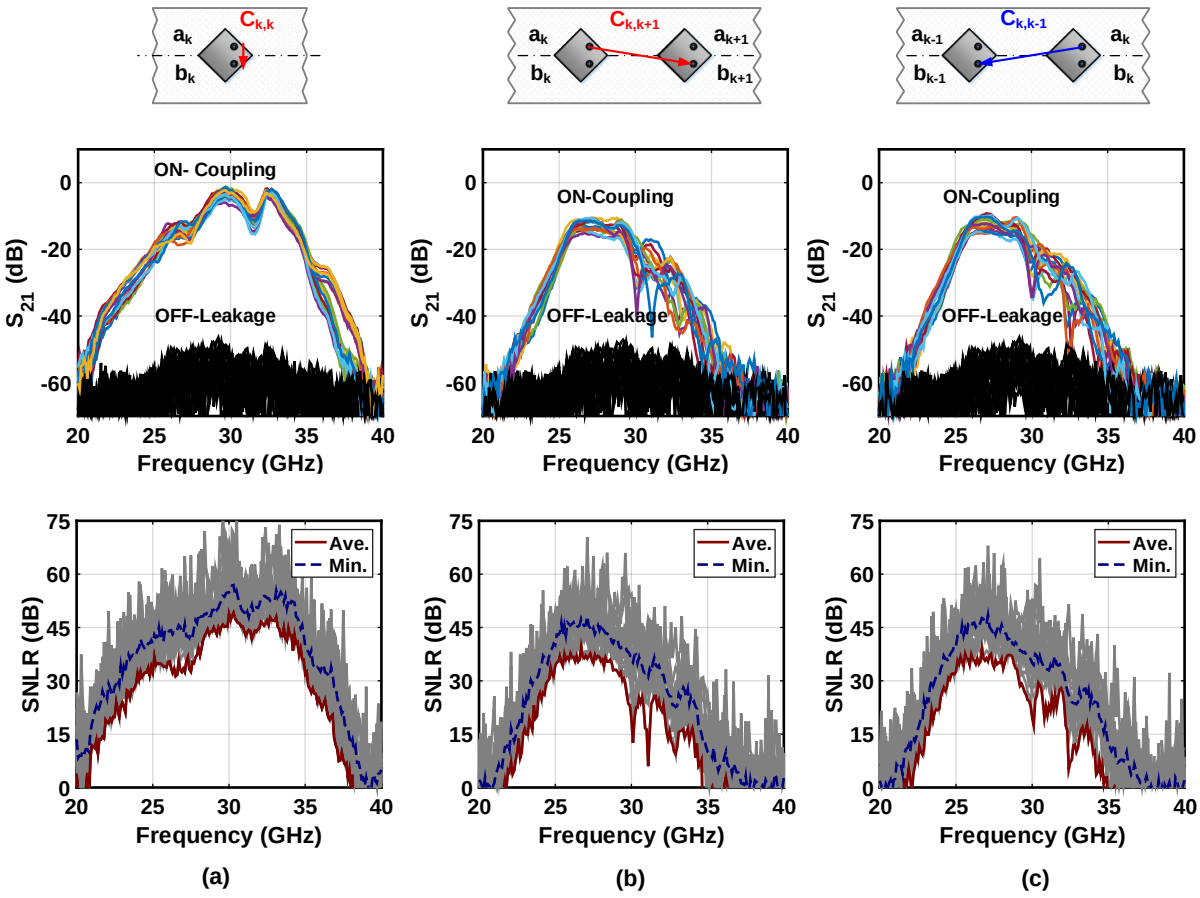

Figure 5.6: Measured couplings and leakage levels (ref.-plane at the array ports) for different TX/RX orthogonality-polarized antenna pairs: (a) TX at k, Rx at k (b) TX at k, RX at k+1 and (c) TX at k, RX at k-1. All channels are in their reference state (maximum gain and zeroth phase state)

-17 dB (port-to-port), which is about 15 dB lower than the $C_{k,k}$ case. The signal to leakage ratio remains sufficiently high (SLNR $\geq$ 30 dB) over the bandwidth from 25-29.5 GHz for all the elements pairs.

Fig. 5.7 presents sample channel testing results using the near-field coupling and using far-field measurements. In the near-field coupling characterization, the TX/RX channel-pair sharing the same antenna are activated. To characterize the TX, the RX state is fixed and TX is cycled through all of its phase shifter and variable gain amplifier (VGA) states. To characterize the RX, the TX state is fixed and the RX is cycled through all of its states. This enables knowing the amplitude and phase of each channel's states relative to each channel's reference state (taken

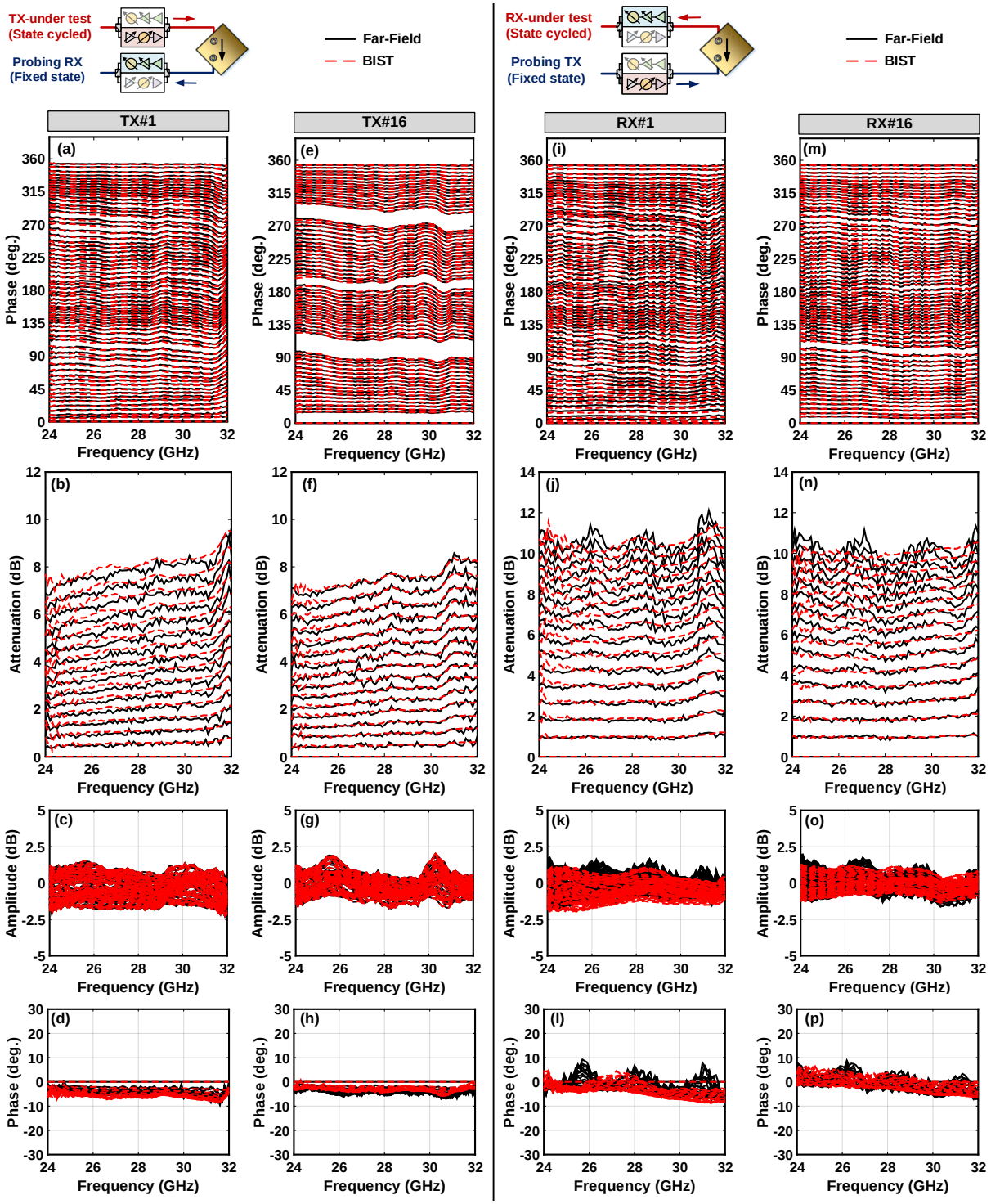

Figure 5.7: Measured channel characterization (phase-shifter and VGA states) using far-field and near-field couplings for Pol. (A) TX (#1,#16) and RX (#1,#16) respectively: (a,e,i,m) phase shifter relative insertion phase, (b,f,j,n) VGA relative insertion gain, (c,j,k,o) phase shifter relative insertion gain, (d,h,l,p) VGA relative insertion phase.

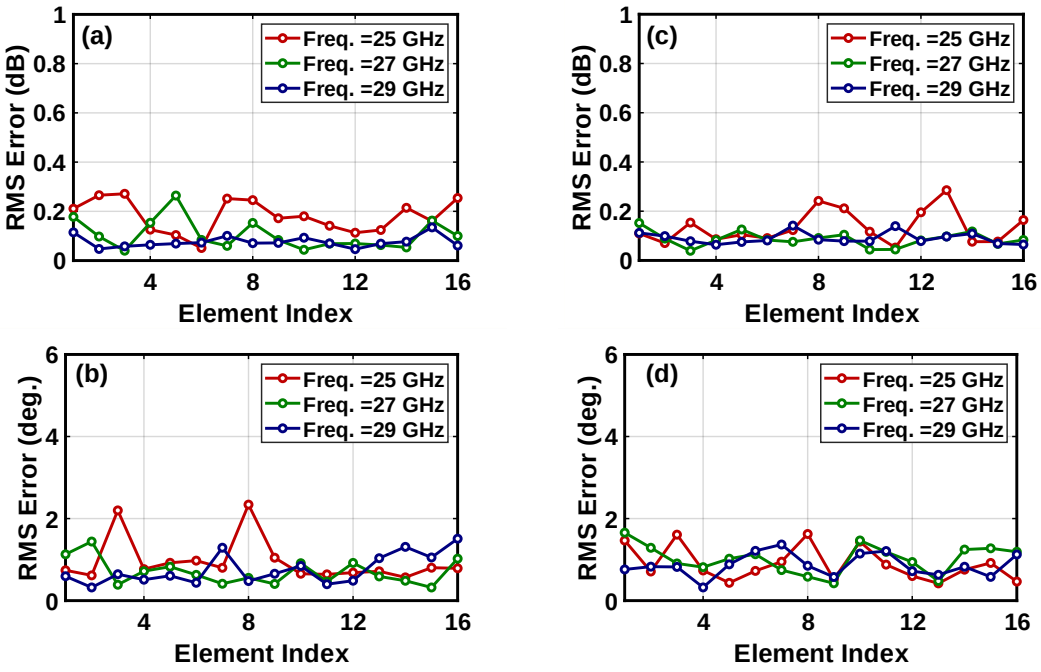

Figure 5.8: Measured rms amplitude and phase errors between far-field and DP-BIST channel characterization results for all channels stat of Pol. A in TX-mode (a,b) and RX-mode (c,d).

as its maximum gain state and zeroth phase state). As can be seen, the near-field characterization agrees very well with the far-field characterization over a wide frequency bandwidth from 24-32 GHz. The variation of the phase shifters and VGAs insertion phase and insertion gain versus phase state and gain state can be determined with high accuracy from the near-field coupling. Interestingly, although all channels are designed to be the same, there is still variation, for instance TX#16 has relatively large gaps in its phase shifter states near the quadrant changes (every 90°) which is detected by both the near-field and far-field characterization. Errors between far-field and near-field results are mostly $\leq$0.6 dB/ 6°, peak errors mainly occur when the VGA is at lowest gain states at which the SNLR is lower by 10-12 dB. The rms errors for all elements in TX mode and in RX mode are shown in Fig. 5.8, the errors are $\leq$0.3 dB/ 3° for all elements at the different frequencies. It is worth mentioning that, in the near field coupling, it is important to ensure that the power levels at the TX input are properly set so as not to saturate or compress the

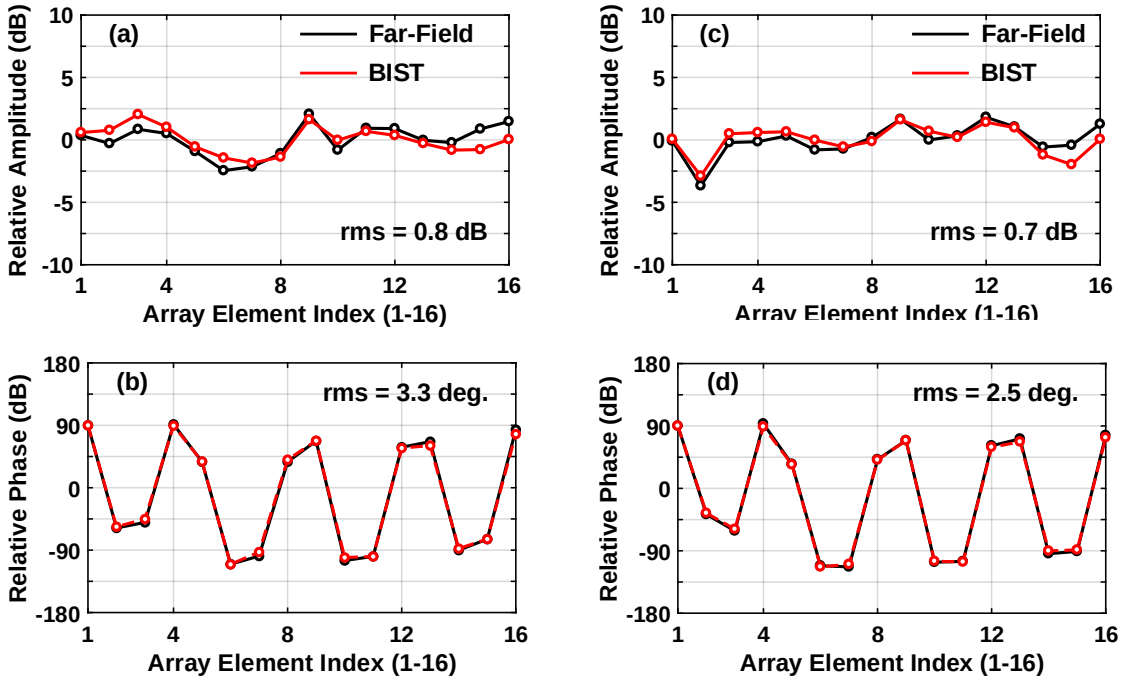

Figure 5.9: Measured DP-BIST and far-field relative array channels amplitudes and phases at 29 GHz in the TX-mode (a,b) and RX-mode (c,d).

RX receiver, especially when transmitting and receiving within the same antenna (port-coupling ≈ -18 dB). In the current case, the RX iP1dB at the maximum gain state is -20 dBm and TX is operated at an output power of ≈ -10 dBm so as to allow enough margin for operation in the linear mode for both the TX and the RX channels. In case the characterization needs to be done at higher power levels especially for TX channels, a further-away weakly coupled receiver can be used or even any of passive probe antennas.

Fig. 5.9 presents the extracted relative channel coefficients for the 45-deg. polarization (RF_A) from the DP-BIST method and the far-field method in TX and RX mode when all elements are in their reference state at 29 GHz. As can be seen, the DP-BIST predicted values are in good agreement with their corresponding far-field ones. The rms error (defined as difference between DP-BIST and far-field values) is 0.7/0.8 dB and 2.5°/3.3° in the RX/TX modes respectively. Fig. 5.10 represents the rms ampltiude and phase errors between far-field and DP-BIST for polarization in TX and RX modes when all the channels are at their zeroth-state. It can be seen

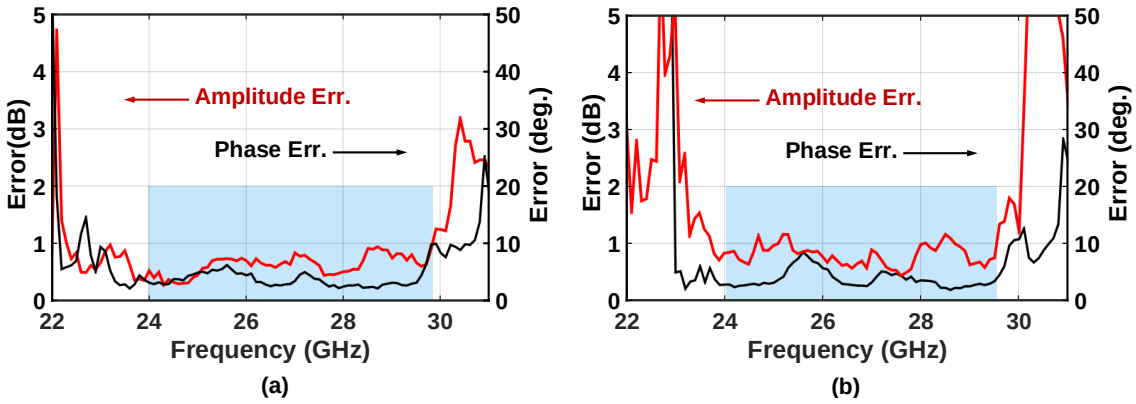

Figure 5.10: Measured DP-BIST and far-field relative array channels amplitudes and phases at 29 GHz in the TX-mode (a) and RX-mode (b).

that over the frequency range from 24 to 29.5 GHz, the errors are less than 0.9 dB/7° in TX mode and less than 1.1 dB/8°. The errors spike outside this range due to the drop in coupling levels, especially $C_{k,k\pm1}$, outside this frequency range as show in Fig. 5.6 (b,c).

The array characterization data based on DP-BIST is then used to correct for the amplitude and phase offsets of the different elements (Fig. 5.9) to establish a uniform illuminated array. Fig. 5.11(a) presents the measured radiation patterns without any calibration, which is clearly un-focused mainly due to the large phase spread on the elements illustrated in Fig. 5.9 which stems from the differnt transmission line length connecting the chip outputs and the antennas. Fig. 5.11(b) presents the measured array radiation patterns after the application of DP-BIST calibration in TX/RX modes to correct for the amplitude and phase spread on the aperture. Both patterns are very close to theoretical expectations with a beam-width of 6.7° and -13 dB side-lobe levels, indicating good calibration quality with small errors. Scanned patterns in the TX and RX modes were also measured and are shown in Fig. 5.12 (a,b), the patterns remain very close to ideal expectations in terms of side-lobes and scan drop.

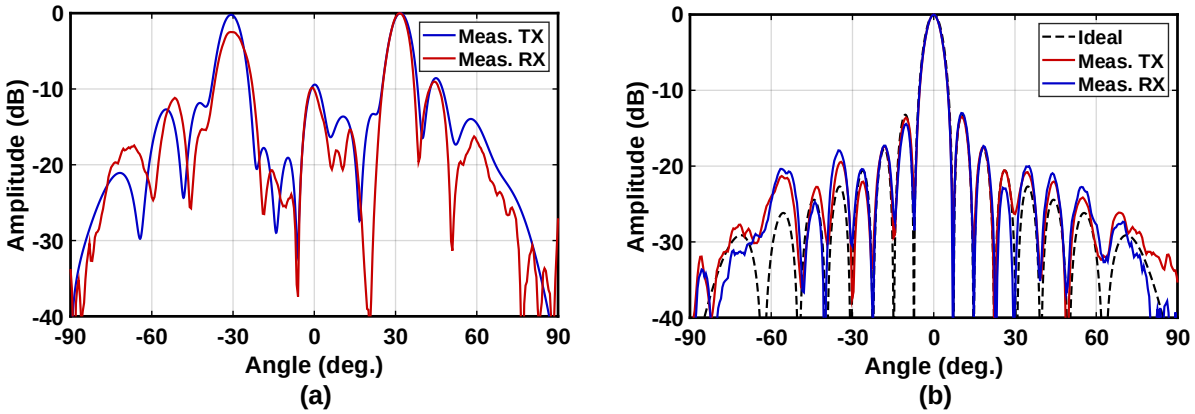

Figure 5.11: Measured scanned polarization (A) broadside patterns at 29 GHz in TX and RX mode: (a) without calibration and (b) after DP-BIST calibration.

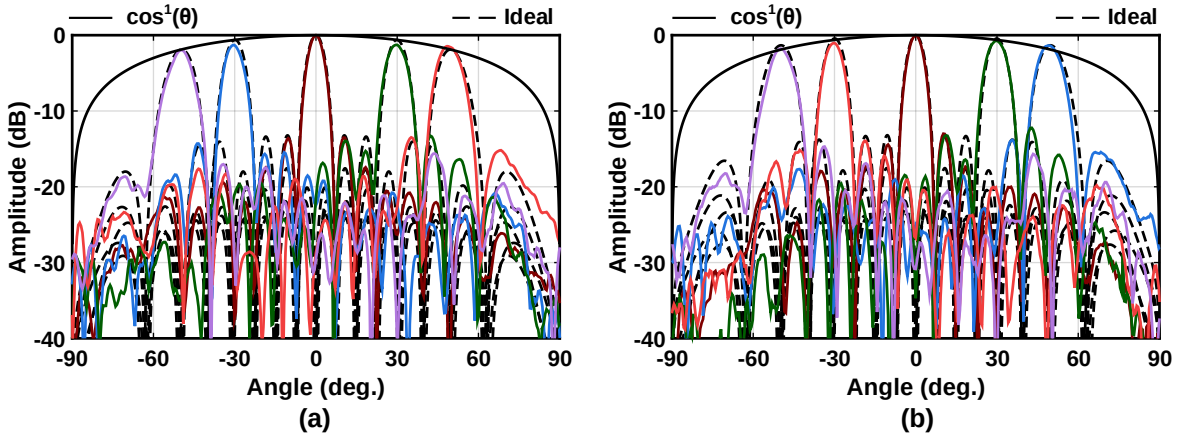

Figure 5.12: Measured scanned polarization (A) patterns at 29 GHz after DP-BIST calibration in: (a) TX-mode and (b) RX mode.

5.5 Conclusion

This work presented an in-situ self-test and self-calibration method for dual-polarized dual-beam 5G TRX phased arrays. The method (DP-BIST) exploits antenna-mutual-coupling symmetries between the two orthogonal polarizations sharing the same aperture. Measurements based on a 16-element linear array demonstrate that DP-BIST agree well with far-field measurements and results in near-ideal phased array patterns.

5.6 Acknowledgement

This work was supported in part by the JUMP program under DARPA/SRC DSSP funding. The authors thank the Qualcomm Proto-lab for assembly of the phased-array with DP-BIST capabilities.

Chapter 5 is mostly a reprint of the material as it appears on IEEE International Microwave Symposium (IMS), 2020. A. Nafe; A. H. Aljuhany; K. Kibaroglu; M. Sayginer; G. M. Rebeiz. The dissertation author was the primary author of this material.

Chapter 6

Conclusion

This dissertation presented two millimeter-wave antenna arrays at 28 GHz for fifth-generation (5G) mobile communication applications and techniques for performing in-situ self-test and self-calibration for single- and dual-polarized 5G phased-arrays. A scalable low-cost 64-element single-polarized transmit/receive phased array is presented in Chapter 2. The array can provide a transmit EIRP up to 52 dBm with a 4 GHz 3-dB EIRP bandwidth (27-31 GHz) and can scan $\pm 50^{\circ}$in azimuth and $\pm 50^{\circ}$ in elevation. The array is designed so that it can be scaled on-grid to any (16xN) size by placing several copies side by side without perturbing the antenna array lattice. This feature allows realization of larger aperture and consequently narrower beams by combining the beams of adjacent 64-element arrays without affecting side-lobe performance. The application area is in multi-beam 5G base-stations providing Gbps communication.

Chapter 3 presented a 2×64-element 28-32 GHz dual-polarized dual-beam phased array for 5G polarization MIMO applications. The array incorporates a shared aperture for both vertically- and horizontally-polarized beams while maintaining high-beam isolation and cross-polarization suppression over scan. An 8-channel SiGe 2×2 quad-beamformer chip is used together with feed-rotation on the 2×2 antenna cell for improved cross-polarization performance. Also, a dual-Wilkinson beamforming network is used in the PCB to obtain two simultaneous

beams. Dual-beam operation and over-the-air (OTA) link measurements were demonstrated achieving record-setting data rates up to 40 Gbps and 60 Gbps using 16- and 64-QAM waveforms at broadside. Link performance with both beams scanned off-broadside to the same direction was also demonstrated achieving a data rate of 9.6 Gbps using 64-QAM waveform with an EVM≤ -25 dB over $\pm 50^{\circ}$ scan range.

In Chapter 4 an in-situ self-calibration for single-polarized 5G phased arrays utilizing mutual antenna coupling from neighboring arrays (labeled Quad BIST) is presented. Mutual-coupling properties of microstrip antennas are studied and near-field coupling dynamic range is analyzed. OFF leakage limitations are identified, and a solution to overcome them is proposed. The Quad-BIST technique was successfully applied to 5G 28 GHz arrays with 4×4 and 8×8 elements in each quadrant. The results show that Quad-BIST predicts the channel states (gain, phase control) with rms errors of 0.2 dB/2° and 0.4 dB/2.5° for the 4×4 and 8×8 quadrants respectively. The relative channel ratios are found to be within rms errors of 0.8 dB/7.5°. Near-ideal patterns are attained using the quadrant-level calibration for both arrays with side-lobe levels below -20 dB over scan.

A second self-calibration technique for in-situ calibration of dual-polarized dual-beam phased arrays is presented in Chapter 5. The procedure, labeled (DP-BIST), exploits the mutual coupling between different antennas of orthogonally polarized beams sharing the same aperture to enable in-situ self-calibration and self-test of the phased array channels of each beam. A proto-type 16-element dual-polarized dual-beam linear phased-array at 29 GHz was implemented for verification of the technique operation. DP-BIST was successfully applied to the linear phased-array prototype and predicted the relative channel states (gain, phase) with rms errors better than 0.3 dB /3° and the relative channel offsets with rms errors 0.8 dB /6° over a wide-bandwidth, showing its feasibility for use in 5G polarization MIMO phased arrays.

6.1 Future Work

In Chapter 4, an in-situ self-calibration technique has been presented for single-polarized 2D MIMO phased arrays. In the implementation, the mutual-coupling data was collected from the prototype quadrant arrays at the RF interface via external VNA measurements and then post-processed offline via MATLAB processing. The promising performance obtained verified the core technique operation and encourages future work on building a more complete online self-calibration system. The system would have transceivers and ADCs/DACs behind every quadrant array and an integrated VNA on the array PCB. The calibration routine can then be implemented on an FPGA controller that interfaces with the arrays and the integrated VNA providing for a complete in-situ solution where the array-calibration and recalibration can be done automatically and periodically in-the-field.

Chapter 5 presented an in-situ self-calibration technique for dual-polarized dual-beam MIMO arrays. DP-BIST operation was verified using linear phased arrays with single beamformer chips instead of dual-beamformer chips due to the non-availability, at the time, of dual-beam former chips capable of simultaneously operating channels of one beam in TX mode while the other beam is in RX mode for performing the required coupling operations. With the availability of such chip-sets, developing 2D dual-polarized dual-beam arrays with self-calibration capabilities is possible to implement and the presented work can be extended, with some modifications, to the more general 2D array case.

Bibliography

[1] W. Roh *et al.*, "Millimeter-wave beamforming as an enabling technology for 5G cellular communications: theoretical feasibility and prototype results," *IEEE Commun. Mag.*, vol. 52, no. 2, pp. 106–113, February 2014.

[2] S. Rangan, T. S. Rappaport, and E. Erkip, "Millimeter-wave cellular wireless networks:potentials and challenges," *Proceedings of the IEEE*, vol. 102, no. 3, pp. 366–385, March 2014.

[3] J. L. Allen, "The theory of array antennas (with emphasis on radar applications)," MASSACHUSETTS INST OF TECH LEXINGTON LINCOLN LAB, Tech. Rep., 1963.

[4] C. Shipley and D. Woods, "Mutual coupling-based calibration of phased array antennas," in *Proceedings 2000 IEEE International Conference on Phased Array Systems and Technology (Cat. No.00TH8510)*, 2000, pp. 529–532.

[5] K. Kibaroglu, M. Sayginer, and G. M. Rebeiz, "A low-cost scalable 32-element 28-GHz phased array transceiver for 5G communication links based on a 2x2 beamformer flip-chip unit cell," *IEEE J. Solid-State Circuits*, vol. 53, no. 5, pp. 1260–1274, May 2018.

[6] K. oglu, M. Sayginer, T. Phelps, and G. M. Rebeiz, "A 64-element 28-GHz phased-array transceiver with 52-dBm EIRP and 8-12-Gb/s 5G Link at 300 meters without any calibration," *IEEE Trans. Microw. Theory Tech.*, vol. 66, no. 12, pp. 5796–5811, Dec 2018.

[7] M. Boers *et al.*, "A 16TX/16RX 60 GHz 802.11ad chipset with single coaxial interface and polarization diversity," *IEEE J. Solid-State Circuits*, vol. 49, no. 12, pp. 3031–3045, Dec 2014.

[8] K. Kibaroglu, M. Sayginer, A. Nafe, and G. M. Rebeiz, "A dual-polarized dual-beam 28 GHz beamformer chip demonstrating a 24 Gbps 64-QAM 2x2 MIMO link," in *Proc. IEEE Radio Freq. Integr. Circuits*, June 2018, pp. 64–67.

[9] S. Shahramian, M. J. Holyoak, and Y. Baeyens, "A 16-element W-band phased-array transceiver chipset with flip-chip PCB integrated antennas for multi-gigabit wireless data links," *IEEE Trans. Microw. Theory Tech.*, vol. 66, no. 7, pp. 3389–3402, July 2018.

[10] A. Nafe, M. Sayginer, K. Kibaroglu, and G. M. Rebeiz, "2x64 dual-polarized dual-beam single-aperture 28 GHz phased array with high cross-polarization rejection for 5G polarization MIMO," in *IEEE MTT-S Int. Microw. Symp. Dig.*, June 2019, pp. 484–487.

[11] J. Pang *et al.*, "A 28GHz CMOS phased-array beamformer utilizing neutralized bi-directional technique supporting dual-polarized MIMO for 5G NR," in *IEEE Int. Solid-State Circuits Conf. (ISSCC) Dig. Tech. Papers*, Feb 2019, pp. 344–346.

[12] B. Sadhu *et al.*, "A 28-GHz 32-element TRX phased-array IC with concurrent dual-polarized operation and orthogonal phase and gain control for 5G communications," *IEEE J. Solid-State Circuits*, vol. 52, no. 12, pp. 3373–3391, Dec 2017.

[13] H. Kim *et al.*, "A 28-GHz CMOS direct conversion transceiver with packaged 2×4 antenna array for 5G cellular system," *IEEE J. Solid-State Circuits*, vol. 53, no. 5, pp. 1245–1259, May 2018.

[14] J. D. Dunworth *et al.*, "A 28GHz bulk-CMOS dual-polarization phased-array transceiver with 24 channels for 5G user and basestation equipment," in *IEEE Int. Solid-State Circuits Conf. (ISSCC) Dig. Tech. Papers*, Feb 2018, pp. 70–72.

[15] J. Dunworth *et al.*, "28 GHz phased array transceiver in 28nm bulk cmos for 5g prototype user equipment and base stations," in *IEEE MTT-S Int. Microw. Symp. Dig.*, June 2018, pp. 1330–1333.

[16] S. Bhardwaj and Y. Rahmat-Samii, "Revisiting the generation of cross-polarization in rectangular patch antennas: A near-field approach," *IEEE Antennas Propag. Mag.*, vol. 56, no. 1, pp. 14–38, Feb 2014.

[17] M. Mirmozafari, G. Zhang, C. Fulton, and R. J. Doviak, "Dual-polarization antennas with high isolation and polarization purity: a review and comparison of cross-coupling mechanisms," *IEEE Antennas Propag. Mag.*, vol. 61, no. 1, pp. 50–63, Feb 2019.

[18] P. K. Mishra, D. R. Jahagirdar, and G. Kumar, "A review of broadband dual linearly polarized microstrip antenna designs with high isolation," *IEEE Antennas Propag. Mag.*, vol. 56, no. 6, pp. 238–251, Dec 2014.

[19] K. Ghorbani and R. B. Waterhouse, "Dual polarized wide-band aperture stacked patch antennas," *IEEE Trans. Antennas Propag.*, vol. 52, no. 8, pp. 2171–2175, Aug 2004.

[20] S. D. Targonski and D. M. Pozar, "Design of wideband circularly polarized aperture-coupled microstrip antennas," *IEEE Trans. Antennas Propag.*, vol. 41, no. 2, pp. 214–220, Feb 1993.

[21] C. Sim, C. Chang, and J. Row, "Dual-feed dual-polarized patch antenna with low cross polarization and high isolation," *IEEE Trans. Antennas Propag.*, vol. 57, no. 10, pp. 3321–3324, Oct 2009.

[22] T. Chi, J. S. Park, S. Li, and H. Wang, "A millimeter-wave polarization-division-duplex transceiver front-end with an on-chip multifeed self-interference-canceling antenna and an all-passive reconfigurable canceller," *IEEE J. Solid-State Circuits*, vol. 53, no. 12, pp. 3628–3639, Dec 2018.

[23] C. Thakkar *et al.*, "A 42.2Gb/s 4.3pJ/b 60 GHz digital transmitter with 12b/Symbol polarization MIMO," in *IEEE Int. Solid-State Circuits Conf. (ISSCC) Dig. Tech. Papers*, Feb 2019, pp. 172–174.

[24] P. S. Hall, J. S. Dahele, and J. R. James, "Design principles of sequentially fed, wide bandwidth, circularly polarised microstrip antennas," *IEE Proceedings H - Microwaves, Antennas and Propagation*, vol. 136, no. 5, pp. 381–389, Oct 1989.

[25] J. Huang, "A Ka-band circularly polarized high-gain microstrip array antenna," *IEEE Trans. Antennas Propag.*, vol. 43, no. 1, pp. 113–116, Jan 1995.

[26] J. Ha, M. A. Elmansouri, P. Valale Prasannakumar, and D. S. Filipovic, "Monostatic co-polarized full-duplex antenna with left- or right-hand circular polarization," *IEEE Trans. Antennas Propag.*, vol. 65, no. 10, pp. 5103–5111, Oct 2017.

[27] J. Granholm and K. Woelders, "Dual polarization stacked microstrip patch antenna array with very low cross-polarization," *IEEE Trans. Antennas Propag.*, vol. 49, no. 10, pp. 1393–1402, Oct 2001.

[28] M. Vigilante, E. McCune, and P. Reynaert, "To EVM or two EVMs?: An answer to the question," *IEEE Solid-State Circuits Mag.*, vol. 9, no. 3, pp. 36–39, Summer 2017.

[29] Y. Yin, S. Zihir, T. Kanar, Q. Ma, H. Chung, L. Gao, and G. M. Rebeiz, "A 37-42 Ghz 8x8 phased-array with 48-51-dbm eirp, 64-qam 30-gb/s data rates, and evm analysis versus channel rms errors," *IEEE Trans. on Microw. Theory Tech.*, vol. xx, no. xx, p. xx, 2020.

[30] K. Kibaroglu, M. Sayginer, A. Nafe, and G. M. Rebeiz, "A dual-polarized dual-beam 28 GHz beamformer chip demonstrating a 24 Gbps 64-QAM 2x2 MIMO link," in *Proc. IEEE Radio Freq. Integr. Circuits Symp. (RFIC)*, June 2018, pp. 64–67.

[31] A. G. Roy *et al.*, "A 37-40 GHz phased array front-end with dual polarization for 5g mimo beamforming applications," in *Proc. IEEE Radio Freq. Integr. Circuits Symp. (RFIC)*, 2019, pp. 251–254.

[32] W. Haselwander, M. Uhlmann, S. Wustefeld, and M. Bock, "Measurement on an active phased array antenna on a near-field range and an anechoic far-field chamber," in *2001 31st European Microwave Conference*, 2001, pp. 1–5.

[33] L. Kuehnke, "Phased array calibration procedures based on measured element patterns," in *2001 Eleventh International Conference on Antennas and Propagation, (IEE Conf. Publ. No. 480)*, vol. 2, 2001, pp. 660–663 vol.2.

[34] J. K. Mulcahey and M. G. Sarcione, "Calibration and diagnostics of the thaad solid state phased array in a planar nearfield facility," in *Proceedings of International Symposium on Phased Array Systems and Technology*, 1996, pp. 322–326.

[35] W. T. Patton and L. H. Yorinks, "Near-field alignment of phased-array antennas," *IEEE Transactions on Antennas and Propagation*, vol. 47, no. 3, pp. 584–591, 1999.

[36] C. A. Balanis, "Antenna theory: a review," *Proceedings of the IEEE*, vol. 80, no. 1, pp. 7–23, 1992.

[37] S. Y. Kim, O. Inac, C. Kim, D. Shin, and G. M. Rebeiz, "A 76-84 GHz 16-element phased-array receiver with a chip-level built-in self-test system," *IEEE Transactions on Microwave Theory and Techniques*, vol. 61, no. 8, pp. 3083–3098, 2013.

[38] O. Inac, F. Golcuk, T. Kanar, and G. M. Rebeiz, "A 90-100 GHz phased-array transmit/receive silicon rfic module with built-in self-test," *IEEE Transactions on Microwave Theory and Techniques*, vol. 61, no. 10, pp. 3774–3782, Oct 2013.

[39] O. Inac, D. Shin, and G. M. Rebeiz, "A phased array rfic with built-in self-test capabilities," *IEEE Transactions on Microwave Theory and Techniques*, vol. 60, no. 1, pp. 139–148, Jan 2012.

[40] T. Kanar, S. Zihir, and G. M. Rebeiz, "A 2-15 GHz accurate built-in-self-test system for wideband phased arrays using self-correcting eight-state I/Q mixers," *IEEE Transactions on Microwave Theory and Techniques*, vol. 64, no. 12, pp. 4250–4261, Dec 2016.

[41] S. Shahramian, M. J. Holyoak, A. Singh, and Y. Baeyens, "A fully integrated 384-element, 16-tile, *w* -band phased array with self-alignment and self-test," *IEEE Journal of Solid-State Circuits*, vol. 54, no. 9, pp. 2419–2434, 2019.

[42] Y. Wang, R. Wu, J. Pang, D. You, A. A. Fadila, R. Saengchan, X. Fu, D. Matsumoto, T. Nakamura, R. Kubozoe, M. Kawabuchi, B. Liu, H. Zhang, J. Qiu, H. Liu, W. Deng, N. Oshima, K. Motoi, S. Hori, K. Kunihiro, T. Kaneko, A. Shirane, and K. Okada, "A 39GHz 64-element phased-array cmos transceiver with built-in calibration for large-array 5g nr," in *2019 IEEE Radio Frequency Integrated Circuits Symposium (RFIC)*, 2019, pp. 279–282.

[43] K. Greene, V. Chauhan, and B. Floyd, "Built-in test of phased arrays using code-modulated interferometry," *IEEE Transactions on Microwave Theory and Techniques*, vol. 66, no. 5, pp. 2463–2479, 2018.

[44] A. Nafe, K. Kibaroglu, M. Sayginer, and G. M. Rebeiz, "An in-situ self-test and self-calibration technique utilizing antenna mutual coupling for 5g multi-beam trx phased arrays," in *2019 IEEE MTT-S International Microwave Symposium (IMS)*, 2019, pp. 1229–1232.

[45] R. J. Mailloux, *Phased Array Antenna Handbook*, 3rd ed. Norwood, MA: Artech House, 2018.

[46] E. R. Hansen, *Phased Array Antennas*, 3rd ed. Hoboken, NJ, USA: Wiley, 1998.

[47] J. Ruze, "The effect of aperture errors on the antenna radiation pattern," *Il Nuovo Cimento (1943-1954)*, vol. 9, no. 3, pp. 364–380, 1952.

[48] D. Pozar, "Input impedance and mutual coupling of rectangular microstrip antennas," *IEEE Transactions on Antennas and Propagation*, vol. 30, no. 6, pp. 1191–1196, 1982.

[49] A. H. Mohammadian, N. M. Martin, and D. W. Griffin, "A theoretical and experimental study of mutual coupling in microstrip antenna arrays," *IEEE Transactions on Antennas and Propagation*, vol. 37, no. 10, pp. 1217–1223, 1989.

[50] R. Jedlicka, M. Poe, and K. Carver, "Measured mutual coupling between microstrip antennas," *IEEE Transactions on Antennas and Propagation*, vol. 29, no. 1, pp. 147–149, 1981.

[51] H. M. Aumann, A. J. Fenn, and F. G. Willwerth, "Phased array antenna calibration and pattern prediction using mutual coupling measurements," *IEEE Transactions on Antennas and Propagation*, vol. 37, no. 7, pp. 844–850, 1989.

[52] K. Kibaroglu, M. Sayginer, and G. M. Rebeiz, "A quad-core 28-32 GHz transmit/receive 5g phased-array ic with flip-chip packaging in sige bicmos," in *2017 IEEE MTT-S International Microwave Symposium (IMS)*, 2017, pp. 1892–1894.

[53] T. Kanar, S. Zihir, and N. Yanduru, "Ultra-compact and modular 5g phased-array 4-channel beamformer front-ends with $\leq 2^{\circ}$ rms phase error," in *2018 IEEE/MTT-S International Microwave Symposium - IMS*, 2018, pp. 1327–1329.

[54] D. M. Pozar, "The active element pattern," *IEEE Transactions on Antennas and Propagation*, vol. 42, no. 8, pp. 1176–1178, 1994.

[55] J. P. Doane, K. Sertel, and J. L. Volakis, "A wideband, wide scanning tightly coupled dipole array with integrated balun (tcda-ib)," *IEEE Transactions on Antennas and Propagation*, vol. 61, no. 9, pp. 4538–4548, 2013.

[56] B. Munk, *Finite Antenna Arrays and FSS*. New York: Wiley, 2003.

[57] S. S. Holland and M. N. Vouvakis, "The planar ultrawideband modular antenna (puma) array," *IEEE Transactions on Antennas and Propagation*, vol. 60, no. 1, pp. 130–140, 2012.